Reconstruction and selection of Z$\rightarrow \tau\tau \rightarrow$e+$\tau$-jet decays at the Compact Muon Solenoid experiment

Konstantinos A. Petridis Torres

High Energy Physics Department.
The Blackett Laboratory.
Imperial College
London

A thesis submitted for the degree of
Doctor of Philosophy
of the University of London
and the Diploma of Imperial College.

June 2009

Declaration

Throughout this thesis, the work of other members of the collaboration is referenced.

During the period of this PhD, the author was responsible for:

- Developing, optimising and maintaining the e+τ-jet trigger for the $10^{32}\,\mathrm{cm}^{-2}\mathrm{s}^{-1}$ instantaneous luminosity regime. A first version of this trigger is documented in [1]. The author then made significant improvements which are documented in Chapter 3 of this thesis, such as adding an ECAL based isolation at the L2 stage of the τ-branch of the e+τ High Level Trigger, replacing the CPU consuming Silicon Strip tracking and isolation with the faster Pixel only tracking for the τ-branch of the e+τ HLT, with no significant increase in the QCD rate.

- Commissioning the L1 τ-jet trigger using Cosmic muon data during the CMS Cosmic Run at Zero Tesla of 2008. These results were the first to show the algorithmic performance of the L1 τ-jet "Isolation" requirement with real data as presented in Chapter 4.

- The complete Z$\rightarrow \tau\tau \rightarrow e$+$\tau$-jet+X study presented in Chapter 5 was the first aimed at measuring the offline τ-jet isolation efficiency. As such the author was solely responsible for this analysis. Particularly, the author was responsible for developing trigger strategies for both the $10^{32}\,\mathrm{cm}^{-2}\mathrm{s}^{-1}$ and $10^{31}\,\mathrm{cm}^{-2}\mathrm{s}^{-1}$ regimes including the 10 GeV electron triggers for the $10^{31}\,\mathrm{cm}^{-2}\mathrm{s}^{-1}$ regime. Moreover further developing already existing tools for γ conversion rejection, optimising the electron and τ-jet kinematic, isolation and identification criteria. Furthermore a various set of parameters to discriminate between τ-jets and electrons were studied and optimised as documented in [2]. Already existing data driven techniques to extract QCD and W+Jet backgrounds were applied and modified to suit the context of this analysis. Methods to extract the Z(ee)+Jets contribution were also studied and documented in [3]. Finally the extraction of the τ-jet efficiency and its systematic error was also performed.

Abstract

Tau leptons are important in Higgs searches, particularly within an MSSM scenario, where decays of electrically neutral (MSSM) Higgs bosons to two τ leptons have a significant branching ratio. The CMS detector is ideally placed to detect such signals both due its good tracking performance and the fine granularity of the electromagnetic calorimeter.
However before such searches take place, it is important to ensure that τ selections are understood. In this context $Z\rightarrow \tau\tau$ decays are important, as they provide a test bench for analogous $H\rightarrow \tau\tau$ and can allow for the measurement of τ-jet selection efficiencies which is vital in extracting the Higgs production cross section and branching ratio and therefore essential in determining potential MSSM parameters.

This thesis contains simulation studies on the development of a combined e+τ-jet trigger tuned for the $10^{32}\,\mathrm{cm}^{-2}\mathrm{s}^{-1}$ instantaneous luminosity regime giving an efficiency for a pre-selected $Z\rightarrow \tau\tau \rightarrow e + \tau$-jet+X sample of $(44.6\pm1.6)\%$ with a QCD rate of $(0.7\pm0.2)\,\mathrm{Hz}$.

Commissioning the L1 τ-jet algorithm on cosmic muon triggered data during the Cosmic Run at Zero Tesla of CMS showed that the current isolation and activity parameters are robust against HCAL noise showing a $<5\%$ drop in efficiency.

Simulated data was used to perform a selection and reconstruction of $Z\rightarrow \tau\tau \rightarrow e+\tau$-jet+X events for the purpose of performing a first measurement of the τ-jet "core" track isolation efficiency using $100\,\mathrm{pb}^{-1}$ of the first LHC data. An efficiency of $85.5\%\pm4.0\%\,(\mathrm{stat.})\pm5.7\%\,(\mathrm{syst.})$ was obtained.

Acknowledgements

The years I have spent working towards my PhD have been a valuable experience. First of all I would like to thank my supervisor, David Colling, for all his help during the last four years and for the numerous times he corrected this thesis.

I would also like to thank Alexandre Nikitenko for his invaluable instruction throughout this period, Simone Gennai, Alexei Safonov, Giuseppe Bagliesi and Sridhara Dasu for their direction in the τ trigger and offline reconstruction as well as in the Z$\rightarrow \tau\tau \rightarrow e + \tau$-jet+X analysis.

Moreover I give thanks to Chris Seez, David Wardrope and Nikos Rompotis for their advice in electron selections, to Anastasis Papageorgiou and Mark Pesaresi for the interesting discussions and to Christina Reimondos for her generosity.

I would like to thank my girlfriend Cora Cheung for her vital encouragement and for her help in correcting this thesis.

Finally I would like to thank my mother Ana Torres-Petridi for her invaluable support and guidance without which this would not have been possible, and my father Angelos Petridis who I am sure is looking down on me and smiling.

Contents

List of Figures

List of Tables

Chapter 1

Theoretical Background

1.1 The Standard Model of Particle Physics

1.1.1 In a nutshell

The Standard Model (SM) of particle physics describes the properties of electroweak and strong interactions of elementary particles. It is one of the most successful theories of the last century and has withstood extensive experimental scrutiny [23][24]. At its heart lies the principle of internal gauge symmetries of the Lagrangian, $\mathcal{L}_{SM}$, expressing themselves as conserved charges [25]. The SM gauge symmetry group is $\mathrm{SU_C}(3) \times \mathrm{SU_L}(2) \times \mathrm{U_Y}(1)$ where the diagonal generators of $\mathrm{SU_C}(3)$ give the QCD colour charges, $\mathrm{SU_L}(2)$ the isospin charges and $\mathrm{U_Y}(1)$ the Weak hypercharge [26][27][28][29]. A cornerstone of the SM is the mechanism of spontaneous electroweak symmetry breaking (EWSB) proposed forty years ago by Higgs, Kibble et al [30][31][32] to generate the weak vector boson masses in a minimal way. It is based on introducing an $\mathrm{SU_L}(2)$ scalar doublet with a corresponding potential with a non-zero vacuum expectation value which reveals the $\mathrm{U_{EM}}(1)$ symmetry from the $\mathrm{SU_L}(2) \times \mathrm{U_Y}(1)$ combination which leaves the vacuum state invariant, and gives three broken generators and therefore three massless Goldstone bosons [33] whose degrees of freedom are replaced by the masses of the three weak gauge bosons. The

vacuum fluctuations on the unbroken direction correspond to a massive scalar particle, the Higgs boson. A more detailed description of electroweak symmetry breaking within a supersymmetry context is described in Section 1.2.4.

1.1.2 Precision Electro-Weak data

Over the last 30 years, the Standard Model of particle physics has been thoroughly tested and probed searching for inconsistencies with experimental data. Some of these more recent tests were carried out by the LEP, SLC and Tevatron collaborations in CERN, SLAC and Fermilab respectively. The results of Table 1.1 are in remarkable agreement with theoretical prediction with all pulls being below 2 standard deviations, apart from $A_{FB}^{0\,b}$ with a pull of -2.9 [4]. $\Delta\alpha_{had}(m_Z^2)$ is the correction to the QED coupling constant arising from hadronic corrections, $\sin^2\theta_{eff}^{lep}$ is the effective weak mixing angle and is equivalent to the radiatively corrected weak mixing angle $\sin^2\theta_W$ measured in leptonic final states, $A_{FB}^{0,f}$ and $\mathcal{A}_f$ measured in $Z \to \bar{f}f$ are the Forward Backward asymmetry as measured by LEP and left-right asymmetry as measured by SLD respectively, R_f denote the partial widths of $Z \to \bar{f}f$, m_W, m_Z, Γ_W, Γ_Z denote the masses and widths of the W and Z bosons and m_t is the top mass. One aspect that has not been yet verified is the existence of the scalar Higgs particle. However using the results of Table 1.1 a constraint can be placed on its mass. In particular radiative corrections to m_W involve contributions from Higgs and top loops and therefore a measurement of m_W and m_t can help constrain the Higgs mass m_H. Figure 1.1 shows on the left the comparison of the indirect constraints on m_W and m_t based on LEP-I and SLD data (dashed contour) and the direct measurements from the LEP-II and Tevatron experiments (solid contour). The shaded region corresponds to the dependence of m_H on these parameters along with the uncertainty arising from $\Delta\alpha(m_Z^2)$ varying by 1σ. The experimental results hint towards a $O(100)\,\mathrm{GeV/c^2}$ Higgs mass. The right plot of Figure 1.1 shows the $\Delta\chi^2 = \chi^2 - \chi^2_{min}$ distribution of the m_H fit using all precision electroweak data as a function of m_H along with the 95% CL lower limit on m_H from direct searches at LEP(shaded area). Including this limit a 95% CL upper limit on m_H is placed at $185\,\mathrm{GeV/c^2}$ [4].

	Measurement with Total Error	Systematic Error	Standard Model fit	Pull
$\Delta\alpha^{(5)}_{\rm had}(m_{\rm Z}^2)$ [41]	0.02758 ± 0.00035	0.00034	0.02768	−0.3
a) LEP-I				
line-shape and				
lepton asymmetries:				
$m_{\rm Z}$ [GeV]	91.1875 ± 0.0021	$^{(a)}0.0017$	91.1875	0.0
$\Gamma_{\rm Z}$ [GeV]	2.4952 ± 0.0023	$^{(a)}0.0012$	2.4958	−0.3
$\sigma^0_{\rm had}$ [nb]	41.540 ± 0.037	$^{(b)}0.028$	41.478	1.7
R^0_ℓ	20.767 ± 0.025	$^{(b)}0.007$	20.743	1.0
$A^{0,\ell}_{\rm FB}$	0.0171 ± 0.0010	$^{(b)}0.0003$	0.0164	0.7
+ correlation matrix [1]				
τ polarisation:				
$\mathcal{A}_\ell$ ($\mathcal{P}_\tau$)	0.1465 ± 0.0033	0.0016	0.1481	−0.5
$q\bar{q}$ charge asymmetry:				
$\sin^2\theta^{\rm lept}_{\rm eff}(Q^{\rm had}_{\rm FB})$	0.2324 ± 0.0012	0.0010	0.23139	0.8
b) SLD				
$\mathcal{A}_\ell$ (SLD)	0.1513 ± 0.0021	0.0010	0.1481	1.6
c) LEP-I/SLD Heavy Flavour				
$R^0_{\rm b}$	0.21629 ± 0.00066	0.00050	0.21582	0.7
$R^0_{\rm c}$	0.1721 ± 0.0030	0.0019	0.1722	0.0
$A^{0,{\rm b}}_{\rm FB}$	0.0992 ± 0.0016	0.0007	0.1038	−2.9
$A^{0,{\rm c}}_{\rm FB}$	0.0707 ± 0.0035	0.0017	0.0742	−1.0
$\mathcal{A}_{\rm b}$	0.923 ± 0.020	0.013	0.935	−0.6
$\mathcal{A}_{\rm c}$	0.670 ± 0.027	0.015	0.668	0.1
+ correlation matrix [1]				
d) LEP-II and Tevatron				
$m_{\rm W}$ [GeV] (LEP-II, Tevatron)	80.399 ± 0.025		80.377	0.9
$\Gamma_{\rm W}$ [GeV] (LEP-II, Tevatron)	2.098 ± 0.048		2.092	0.1
$m_{\rm t}$ [GeV] (Tevatron [56])	172.4 ± 1.2	1.0	172.5	−0.1

Table 1.1: Table summarising the electroweak precision measurements at LEP1 LEP2 SLC and Tevatron as of the Summer of 2008 [4]. These results are compared to the SM fit results by evaluating the pull P= $(O_{\rm meas} - O_{\rm fit})/\sigma_{\rm meas}$.

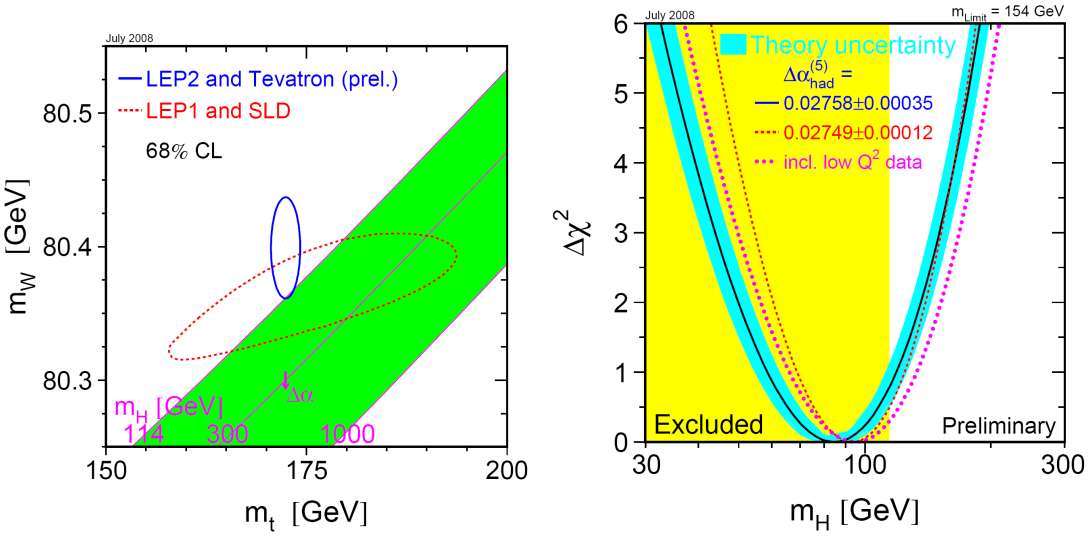

Figure 1.1: Left: Indirect constraints on m_W and m_t based on LEP-I and SLD data (dashed contour) and the direct measurements from the LEP-II and Tevatron experiments (solid contour). The shaded region corresponds to the dependence of m_H on these parameters along with the uncertainty arising from $\Delta\alpha(m_Z^2)$ varying by 1σ. Right:$\Delta\chi^2 = \chi^2 - \chi^2_{min}$ distribution of the m_H using all precision electroweak data as a function of m_H along with the 95%CL lower limit on m_H from direct searches at LEP (shaded area). Including this limit a 95%CL an upper limit on m_H is placed at $185\,\mathrm{GeV/c^2}$ [4].

1.1.3 Outstanding Issues

Although the SM has withstood extensive experimental tests, it still leaves questions unanswered while creating new ones. For example it does not say anything about the gravitational force, does not explain the pattern of fermion masses and in its simplest version does not incorporate masses for the neutrinos [5]. Furthermore the model is based on the direct product of three simple groups ($\mathrm{SU_C}(3) \times \mathrm{SU_L}(2) \times \mathrm{U_Y}(1)$) with different coupling constants and does not provide a true unification of the electroweak and strong interactions. Therefore, one hopes for the existence of a more fundamental Grand Unified Theory (GUT), which describes the three forces within a single gauge group. However, given the high precision measurements at LEP and elsewhere and the particle content of the SM, the evolution of the gauge coupling constants is such that they fail to meet at a common point [5] [34]. Moreover if we accept the SM as an effective theory valid up to a scale Λ, when calculating the radiative corrections to the Higgs boson mass, one encounters divergences quadratic in the cut-off scale Λ. If we choose the cut-off to be the GUT scale, the Higgs

particle mass will prefer to be close to the very high scale unless an unnatural fine adjustment of parameters is performed. This is what is called the naturalness or fine-tuning problem [5].

1.2 Introduction to Supersymmetry

[1] Supersymmetry (SUSY) provides us with an additional set of operators which can transform bosonic fields to fermionic fields and vice versa. The importance of such transformations is that they offer an extension of space-time related transformations without violating the Coleman-Mandula theorem which states that: *In a relativistic theory with non trivial scattering in 4 spacetime dimensions, the only conserved quantities that transform as tensors (including scalars) under the Lorentz group are associated to the generators of the Poincaré group P_m and M_{mn} which generate translations and Lorentz transformations respectively and Z_i which generate the internal symmetry transformations and commute with P_m and M_{mn}* [37][36]. The requirement that conserved quantities transform as tensors under the Lorentz group however can be avoided by extending charges to hold a spinorial index, as spinors transform in a separate way to tensors under a Lorentz transformation. Therefore this offers us a way of bypassing the restrictions of the Coleman-Mandula theorem as it applies only to tensorial charges. SUSY transformations change the spin value of the fields and hence the generators of SUSY do not commute with the spin operators. This means that SUSY generators carry a spinor index which is exactly what is required in order to bypass the Coleman-Mandula theorem. It is thus natural to promote the commutators of the SUSY Lie algebra to anti-commutators (super Lie algebra) [38]. Specifically if we consider Q_α as the generator of SUSY transformations where "α" is a Weyl-type spinor index and $\bar{Q}_{\dot{\alpha}} \equiv Q^\dagger_\alpha$, it can be shown that the algebra of the SUSY generators takes the form of Equation 1.1.

$$\begin{aligned} \{Q_\alpha, \bar{Q}_{\dot{\beta}}\} &= 2\sigma^m_{\alpha\dot{\beta}} P_m \\ \{Q_\alpha, Q_\beta\} &= \{\bar{Q}_{\dot{\alpha}}, \bar{Q}_{\dot{\beta}}\} = 0 \\ [Q_\alpha, P_m] &= [\bar{Q}_{\dot{\alpha}}, P_m] = [P_m, P_n] = 0 \end{aligned} \tag{1.1}$$

[1] This section draws heavily from [34], [35] and [36]

where $\sigma^m = [\mathbb{1}_2, \sigma^i]$ and σ^i are the Pauli matrices, α and $\dot{\alpha}$ denote left and right handed Weyl spinor index respectively and $Q^*_\alpha \equiv \bar{Q}_{\dot{\alpha}}$ where we have used the Van der Waerden index notation [34]. The fact that the SUSY generators commute with P_m means that $[Q_\alpha, P_m P^m] = 0$ and therefore SUSY multiplets contain fields of the same mass. One can consider a finite element of the group $G(a^m, \theta, \bar{\theta}) = e^{(\theta_\alpha Q^\alpha + \bar{\theta}^{\dot{\alpha}} \bar{Q}_{\dot{\alpha}} - a^m P_m)}$. where $(\theta_\alpha, \bar{\theta}^{\dot{\alpha}})$ are Grassman Numbers [39] carrying a Weyl-spinor index and satisfy $\{\theta_\alpha, \bar{\theta}_{\dot{\beta}}\} = \{\bar{\theta}_{\dot{\alpha}}, \bar{\theta}_{\dot{\beta}}\} = \{\theta_\alpha, \theta_\beta\} = 0$. Given a function $S(x^m, \theta, \bar{\theta})$ (also known as a superfield), the action of G on S is

$$G : S(x^m, \theta, \bar{\theta}) \mapsto e^{(\theta_\alpha Q^\alpha + \bar{\theta}^{\dot{\alpha}} \bar{Q}_{\dot{\alpha}} - a^m P_m)} S(x^m, \theta, \bar{\theta}) \tag{1.2}$$

with

$$G(x^m, \theta, \bar{\theta}) G(a^m, \xi, \bar{\xi}) = G(x^m + a^m - i\xi\sigma^m\bar{\theta} + i\theta\sigma^m\bar{\xi}, \theta + \xi, \bar{\theta} + \bar{\xi}) \tag{1.3}$$

By considering the effect of G on the parameter space $(x^m, \theta, \bar{\theta})$ and expanding $S(x^m + a^m - i\xi\sigma^m\bar{\theta} + i\theta\sigma^m\bar{\xi}, \theta + \xi, \bar{\theta} + \bar{\xi})$ around $(x^m, \theta, \bar{\theta})$ one can obtain a linear representation of the SUSY generators as shown in Equation 1.4

$$\begin{aligned} P_m &= i\partial_m \\ iQ_\alpha &= \frac{\partial}{\partial\theta^\alpha} - i\sigma^m_{\alpha\dot{\alpha}}\bar{\theta}^{\dot{\alpha}}\partial_m \\ i\bar{Q}_{\dot{\alpha}} &= -\frac{\partial}{\partial\bar{\theta}^{\dot{\alpha}}} + i\theta^\alpha\sigma^m_{\alpha\dot{\alpha}}\partial_m \end{aligned} \tag{1.4}$$

As S now depends on $(x, \theta, \bar{\theta})$ it is important to be able to define derivatives D along all of these directions in such a way that they preserve SUSY i.e they commute with G and hence they commute or anti-commute with the generators Q and $\bar{Q}$. It can be shown [34] that the appropriate derivatives are

$$\begin{aligned} \partial_m &= \frac{\partial}{\partial x^m} \\ D_\alpha &= \frac{\partial}{\partial\theta^\alpha} + i\sigma^m_{\alpha\dot{\alpha}}\bar{\theta}^{\dot{\alpha}}\partial_m \\ \bar{D}_{\dot{\alpha}} &= -\frac{\partial}{\partial\bar{\theta}^{\dot{\alpha}}} - i\theta^\alpha\sigma^m_{\alpha\dot{\alpha}}\partial_m \end{aligned} \tag{1.5}$$

The physical meaning of superfield S can be seen by expanding in terms of θ and $\bar{\theta}$ around the point $(x^m, 0_\alpha, 0_{\bar{\alpha}})$. As θ and $\bar{\theta}$ are Grassman variables the expansion

will be finite with terms no more than two powers in θ and $\bar{\theta}$ [2] Therefore one can write

$$\begin{aligned} S(x,\theta,\bar{\theta}) &= \phi(x)+\theta\psi(x)+\bar{\theta}\bar{\chi}(x)+\theta\theta m(x)+\bar{\theta}\bar{\theta}n(x)+\theta\sigma^m\bar{\theta}v_m(x)+ \\ &\quad +(\theta\theta)\bar{\theta}\bar{\lambda}(x)+(\bar{\theta}\bar{\theta})\theta\xi(x)+(\theta\theta)(\bar{\theta}\bar{\theta})d(x) \end{aligned} \tag{1.6}$$

where $\theta\theta := \theta^\alpha\theta_\alpha$, $\bar{\theta}\bar{\theta} := \bar{\theta}_{\dot{\alpha}}\bar{\theta}^{\dot{\alpha}}$ With $\phi(x), m(x), n(x), v_m(x), d(x)$ representing bosonic fields and $\psi(x), \chi(x), \lambda(x), \xi(x)$ representing fermionic fields with $\psi(x)$ being a left handed Weyl spinor and $\bar{\chi}(x)$ a right handed Weyl spinor. Although superfields form a linear representation of the SUSY algebra, the large number of unphysical constituent fields indicates that it is a reducible representation. Irreducible representations are obtained by imposing SUSY covariant constraints on S such that it still forms a linear representation of the SUSY algebra. There are two main constraints: $\bar{D}_{\dot{\alpha}}S = 0$ which is used to construct a Chiral superfield and $S = S^\dagger$ which is used to construct a Vector superfield.

1.2.1 Chiral Superfields

As $\{\bar{D}_{\dot{\alpha}}, Q_\beta\} = \{\bar{D}_{\dot{\alpha}}, Q_{\dot{\beta}}\} = 0$, $\bar{D}_{\dot{\alpha}}$ commutes with G, therefore $\bar{D}_{\dot{\alpha}}(G(x,\xi,\bar{\xi})S) = G(x,\xi,\bar{\xi})\bar{D}_{\dot{\alpha}}S$ and hence it is a SUSY covariant transformation. It can be shown that the most general solution to the $\bar{D}_{\dot{\alpha}}S = 0$ constraint is a superfield $\Phi(x,\theta,\bar{\theta}) \equiv S(x,\theta,\bar{\theta})$ whose form is

$$\begin{aligned} \Phi(x,\theta,\bar{\theta}) &= \phi(x)+\sqrt{2}\theta\psi(x)+(\theta\theta)F(x)+i\partial_m\phi(x)\theta\sigma^m\bar{\theta}+ \\ &\quad -\frac{i}{\sqrt{2}}(\theta\theta)\partial_m\psi(x)\sigma^m\bar{\theta}-\frac{1}{4}\partial_m\partial^m\phi(x)(\theta\theta)(\bar{\theta}\bar{\theta}) \end{aligned} \tag{1.7}$$

Where ϕ,F are complex scalar fields and ψ is a left handed Weyl spinor. As Φ only contains a left handed spinor as a constituents it is also known as a left chiral superfield. Consequently $\Phi^\dagger$ contains $\bar{\psi}$ and is known as a right chiral superfield.

The SUSY transformations of the constituent fields can be derived by considering the behaviour of Φ under an infinitesimal SUSY transformation

$$\delta_{\xi,a}\Phi = i(\xi Q + \bar{\xi}\bar{Q} - a^m P_m)\Phi \tag{1.8}$$

[2] As θ, $\bar{\theta}$ are Grassman spinors, $\theta_\alpha\theta_\alpha = 0$ however $\theta^\alpha\theta_\alpha = \theta^\alpha\epsilon_{\alpha\beta}\theta^\beta \neq 0$ where $\epsilon_{\alpha\beta} = i\sigma^2_{\alpha\beta}$ is the lowering undotted index operator.

Therefore by replacing Q, $\bar{Q}$, P_m with their linear representation given by (1.4) , expressing $\delta\Phi$ in terms of the constituent fields remembering that θ, $\bar{\theta}$ are space-time independent, and equating terms of equal powers in θ and $\bar{\theta}$ from the LHS and RHS of Equation (1.8) one obtains

$$\begin{aligned}\delta\phi(x) &= \sqrt{2}\xi\psi(x)\\ \delta\psi(x) &= \sqrt{2}\xi F(x) + i\sqrt{2}\partial_m\phi(x)\sigma^m\bar{\xi}\\ \delta F(x) &= i\sqrt{2}\partial_m\psi(x)\sigma^m\bar{\xi}\end{aligned} \tag{1.9}$$

This is exactly what was expected by a SUSY transformation which transforms fermions into bosons and vice versa. $F(x)$ transforms as a total derivative under a SUSY transformation. Therefore by noticing that products and sums of chiral superfields are also chiral superfields, SUSY invariant actions can be built out of lagragians containing the $\theta\theta$-term (F-term) of a function $W(\Phi)$ also know as the superpotential $[W(\Phi)]_F$, as $F(x)$ and consequently $[W(\Phi)]_F$ leaves the action $I = \int L\, dx^4$ invariant (Gauss's theorem) under a SUSY transformation. By writing a general (renormalisable) W(Φ) as

$$[W(\Phi)]_F = [\frac{1}{2}m_{ij}\Phi_i\Phi_j + \frac{1}{3}\lambda_{ijk}\Phi_i\Phi_j\Phi_k]_{\theta\theta} \tag{1.10}$$

where m_{ij} and λ_{ijk} are coupling constants, a basic Lagrangian for ϕ_i, ψ_i, F_i can be written as

$$\mathcal{L} = \partial_m\phi_i^\dagger\partial^m\phi_i + i\bar{\psi}_i\bar{\sigma}^m\partial_m\psi_i + F_i^\dagger F_i + ([W(\Phi)]_F + [W(\Phi)]_F^\dagger) \tag{1.11}$$

where the first two terms are the familiar kinetic terms for complex scalar and Weyl fermionic fields with $\bar{\sigma}^m = [\mathbb{1}_2, -\sigma^i]$ and $F_i^\dagger F_i$ is the simplest kinetic term for F_i with the correct dimension. Writing out explicitly the $\theta\theta$ term of $W(\Phi)$ in terms of the constituent fields and using the Euler-Lagrange equations for F, one obtains an expression for F as

$$F_i^\dagger = -\frac{\partial W(\phi)}{\partial\phi_i} \tag{1.12}$$

Thus F_i can be completely eliminated using the equations of motion (auxiliary field).

1.2.2 Vector Superfield

Properties of the Vector Superfield

The second covariant constraint on superfield $S(x,\theta,\bar{\theta})$ is $S = S^{\dagger}$. Such a constraint hints towards a superfield that contains real bosonic fields. Indeed without loss of generality superfield $\mathcal{V}(x,\theta,\bar{\theta}) \equiv S(x,\theta,\bar{\theta})$ that satisfies the above condition can be written as

$$\begin{aligned}\mathcal{V}(x,\theta,\bar{\theta}) &= c(x) + i\theta\chi(x) - i\bar{\theta}\bar{\chi}(x) + \frac{1}{2}\theta\theta[m(x)+in(x)] \\ &\quad -\frac{1}{2}i\bar{\theta}\bar{\theta}[m(x)-in(x)] + \theta\sigma^{m}\bar{\theta}V_{m}(x) \\ &\quad +i\theta\theta\bar{\theta}[\bar{\lambda}(x) + \frac{i}{2}\bar{\sigma}^{m}\partial_{m}\chi(x)] - i\bar{\theta}\bar{\theta}\theta[\lambda(x) + \frac{i}{2}\sigma^{m}\partial_{m}\bar{\chi}(x)] \\ &\quad +\frac{1}{2}\theta\theta\bar{\theta}\bar{\theta}[d(x) - \frac{1}{2}\partial^{m}\partial_{m}c(x)] \end{aligned} \tag{1.13}$$

Where c, m, n, d are real scalar fields, χ and λ are left handed Weyl spinor fields and V_m is a real vector field. This is why $\mathcal{V}$ is called a vector superfield as it contains a vector gauge boson as one of its constituents. As for the chiral superfield case, by considering

$$\delta_{\xi,a}\mathcal{V} = i(\xi Q + \bar{\xi}\bar{Q} - a^{m}P_{m})\mathcal{V} \tag{1.14}$$

replacing Q, $\bar{Q}$, P_m with their linear representation given by (1.4) , expressing $\delta\mathcal{V}$ in terms of the constituent fields remembering that θ, $\bar{\theta}$ are space-time independent, and equating terms of equal powers in θ and $\bar{\theta}$ from the LHS and RHS of Equation (1.14) one obtains

$$\begin{aligned}\delta V^{m}(x) &= i(\xi\sigma^{m}\bar{\lambda}(x) - \lambda(x)\sigma^{m}\bar{\xi}) - \partial^{m}(\xi\chi(x) + \bar{\xi}\bar{\chi}(x)) \\ \delta\lambda(x) &= -id(x)\xi - \frac{1}{2}(\sigma^{m}\bar{\sigma}^{n})\xi V_{mn}(x) \\ \delta d(x) &= \partial_{m}(-\xi\sigma^{m}\bar{\lambda}(x) + \lambda(x)\sigma^{m}\bar{\xi}) \\ \delta V_{mn}(x) &= i\partial_{m}(\xi\sigma_{n}\bar{\lambda}(x) - \lambda(x)\sigma_{n}\bar{\xi}) - i\partial_{n}(\xi\sigma_{m}\bar{\lambda(x)} - \lambda(x)\sigma_{m}\bar{\xi})\end{aligned} \tag{1.15}$$

where $V_{mn} = (\partial_m V_n(x) - \partial_n V_m(x))$ and it is equal to the field strength tensor F_{mn} for an abelian gauge theory. Equation 1.15 shows that $V_{mn}(x)$, $d(x)$, $\lambda(x)$ form an irreducible representation of the SUSY algebra just by themselves since given

a SUSY transformation they all transform into each-other without the presence of $c(x)$, $\chi(x)$, $m(x)$, $n(x)$. This indicates that these fields are unphysical and need to be removed. This is possible when considering SUSY gauge transformations. Furthermore as in the chiral superfield case $d(x)$ transforms as a total derivative under a SUSY transformation. This means that one can build SUSY invariant actions considering the "D" term of a vector superfield.

The Wess-Zumino Gauge

As the only requirement on a vector superfield is to be real we could construct a specific one by using chiral superfield Φ in the form $i(\Phi - \Phi^\dagger)$ where for this case

$$\begin{aligned} &\lambda(x) = 0 \\ &d(x) = 0 \\ &\chi(x) = \sqrt{2}\psi(x) \\ &V_m(x) = -\partial_m(\phi + \phi^\dagger) \\ &\frac{1}{2}(m(x) + in(x)) = F(x) \end{aligned} \tag{1.16}$$

where ϕ,ψ,F are the constituents of Φ. Wess and Zumino [40] noted that since under an abelian gauge transformation $V^m(x) \mapsto V^m(x) + \partial^m\Lambda(x)$, the equivalent for a vector superfield is

$$\mathcal{V} \mapsto \mathcal{V} + i(\Phi - \Phi^\dagger) \tag{1.17}$$

since $i(\Phi - \Phi^\dagger)$ is a vector superfield which contains a $\partial_m\Lambda(x)$-type term in the form of $\partial_m(\phi + \phi^\dagger)$ as shown in Equation (1.16). Furthermore $c(x)$, $\chi(x)$, $m(x)$, $n(x)$ fields of $\mathcal{V}$ can be set to zero by a suitable choice of $(\phi - \phi^\dagger)$, ψ and F of Φ while still leaving $(\phi + \phi^\dagger)$ arbitrary. Therefore in the Wess-Zumino gauge

$$\mathcal{V}_{WZ}(x, \theta, \bar{\theta}) = \theta\sigma^m\bar{\theta}V_m(x) + i\theta\theta\bar{\theta}\bar{\lambda}(x) - \bar{\theta}\bar{\theta}\theta\lambda(x) + \frac{1}{2}\theta\theta\bar{\theta}\bar{\theta}d(x) \tag{1.18}$$

and under a gauge transformation of the type in Equation (1.17) transforms $V^m(x) \mapsto V^m(x) + \partial^m\Lambda(x)$ and leaves $\lambda(x)$ and $d(x)$ invariant (same as in standard gauge theory as far as fermionic fields are concerned).

1.2.3 Non-Abelian Supersymmetric Gauge Theory

In order to include in the Lagrangian interactions between fermions and gauge bosons one needs to include all the degrees of freedom of the fermionic fields. Furthermore to create a SUSY invariant action only single chirality superfields can be used. Therefore we need to define left chiral superfields S and T containing both left and right handed degrees of freedom for the fermion and anti fermion with

$$\begin{aligned} S &= \frac{1}{\sqrt{2}}(\Phi_1 + i\Phi_2) \\ T &= \frac{1}{\sqrt{2}}(\Phi_1 - i\Phi_2) \end{aligned} \tag{1.19}$$

where Φ_1 and Φ_2 are left chiral superfields meant to account for the left and right handed fermionic degrees of freedom. However chiral superfields only contain left handed fermions and therefore we must interpret the left handed component of the anti-fermion as the charge conjugate right handed component of the fermion. For example $\psi_L^{e+} \equiv (\psi_R^{e-})^C$ where "C" stands for charge conjugation. One can extend the notion of a non Abelian gauge transformation for a chiral superfield by

$$\begin{aligned} S &\mapsto e^{(-2igT^a\Lambda^a)}S \\ T &\mapsto e^{(2igT^{a*}\Lambda^a)}T \end{aligned} \tag{1.20}$$

where Λ^a are chiral superfields and T^a are the generators of the gauge group. The motivation for the difference in the sign of the exponential will become more evident later. Using Equation (1.20) a gauge invariant combination of superfields is

$$\begin{aligned} &S^\dagger e^{(2gT^a\mathcal{V}^a_{WZ})}S \\ &T^\dagger e^{(-2gT^a\mathcal{V}^a_{WZ})}T \end{aligned} \tag{1.21}$$

as long as

$$\mathcal{V}_{WZ} \mapsto \mathcal{V}_{WZ} + i(\Lambda - \Lambda^\dagger) + \frac{i}{2}[\mathcal{V}_{WZ}, \Lambda + \Lambda^\dagger] \tag{1.22}$$

with $\mathcal{V}_{WZ} = 2g\mathcal{V}^a_{WZ}T^a$ and $\Lambda = 2g\Lambda^a T^a$, which in terms of superfield components V^a_m transforms as

$$V^a_m \mapsto V^a_m + \partial_m(\phi^a + \phi^{a\dagger}) + gf^{abc}(\phi^b + \phi^{b\dagger})V^c_m \tag{1.23}$$

where ϕ^a are the scalar constituents of Λ^a and f^{abc} is the structure constant of the gauge group with $[T^a, T^b] = if^{abc}T^c$. Equation (1.23) has exactly the form of a non Abelian gauge transformation of a vector field in the non SUSY case. Now since SUSY links V^m with λ (Equation (1.15)) and V^m transforms in the adjoint representation of the internal symmetry group, then so should λ and thus $\lambda = \lambda_a T_a$ (spinor index is suppressed). In this case the internal symmetry covariant derivate becomes $\mathcal{D}^m\bar{\lambda}_a^{\dot{\alpha}} = (\partial^m - gf_{abc}V_b^m)\bar{\lambda}_c^{\dot{\alpha}}$. The missing ingredient for a completely SUSY compatible gauge theory is the Lagrangian term for the gauge super-field (containing the familiar $V_{mna}V_a^{mn}$ term where $V_{mn} = (\mathcal{D}_m V_n - \mathcal{D}_n V_m)$). A simple way of obtaining such a term is by remembering that the constituent fields of $\mathcal{V}_{WZ}$ must all have the same mass as they belong to the same supermultiplet. So as the gauge field mass is zero (prior to EWK symmetry breaking) so should be the masses of the fermionic fields $\lambda^a(x)$ and the auxiliary fields $d^a(x)$. Furthermore as $d^a(x)$ are real auxiliary fields, the simplest Lagrangian term can be written as $\frac{1}{2}d^a(x)d^a(x)$. Hence a SUSY and gauge invariant Lagrangian for $\mathcal{V}_{WZ}$ can be written as

$$\mathcal{L}_{\mathcal{V}} = -\frac{1}{4}V_{mn}^a(x)V^{amn}(x) + i\lambda^a(x)\sigma^m\mathcal{D}_m\bar{\lambda}^a(x) + \frac{1}{2}d^a(x)d^a(x) \tag{1.24}$$

where $\mathcal{D}^m\bar{\lambda}_a^{\dot{\alpha}} = (\partial^m - gf_{abc}V_b^m)\bar{\lambda}_c^{\dot{\alpha}}$ and the first term of Equation (1.24) is the familiar field strength gauge invariant Lagrangian. Finally since $(S^\dagger e^{(2gT^a\mathcal{V}_{WZ}^a)}S)$ and $(T^\dagger e^{(-2gT^a\mathcal{V}_{WZ}^a)}T)$ are real and made up of products of superfields, they are also vector superfields. Therefore we can build gauge and SUSY invariant actions by considering the "D" term of such products as discussed in Section 1.2.2

$$\begin{aligned}\mathcal{L}_S = [S^\dagger e^{(2gT^a\mathcal{V}_{WZ}^a)}S]_D &= (\mathcal{D}_m\phi_s(x))^\dagger(\mathcal{D}^m\phi_s(x)) + i\psi_s(x)\sigma^m\mathcal{D}_m\bar{\psi}_s(x) + F_s^\dagger(x)F_s(x) \\ &\quad + i\sqrt{2}g(\phi_s^\dagger(x)T^a\lambda^a\psi_s(x) - \bar{\psi}_s(x)T^a\bar{\lambda}^a(x)\phi_s(x)) + \\ &\quad + g\phi_s^\dagger(x)T^a d^a(x)\phi_s(x)\end{aligned} \tag{1.25}$$

where ϕ_s, ψ_s and F_s are the constituents of the chiral superfield S, λ^a, d^a are the constituents of $\mathcal{V}_{WZ}^a$, $\mathcal{D}_m = \partial_m + igT^aV_m^a$ and the index i of the gauge group multiplet is suppressed. The first two terms of equation (1.25) are the familiar kinetic terms for a scalar and Weyl fermion field respectively. The last two terms represent new interactions between between ϕ_s, ψ_s λ^a and d^a. A similar expression could be written

for the T superfield. Therefore putting Equations (1.25) and (1.24) together, and solving the Euler-Lagrange equations for $F(x)$ and $d(x)$, one obtains

$$\begin{aligned} F^{\dagger}_{s\,i}(x) &= -\frac{\partial W(\phi)}{\partial \phi_{s\,i}(x)} \\ d_a(x) &= -g\sum_{ij}(\phi^{\dagger}_{s\,i}(x)T^a_{ij}\phi_{sj}(x)) \end{aligned} \tag{1.26}$$

Where W is the superpotential described in Section 1.2.1 and needs to be defined in terms of the S and T chiral superfields. Therefore one can write the tree level effective potential which contains the mass terms of ϕ_s, ψ_s and their interactions as

$$V(\phi_{s\,i}(x)) = \sum_i \left|\frac{\partial W(\phi)}{\partial \phi_{s\,i}(x)}\right|^2 + \frac{1}{2}g^2\sum_a\left(\sum_i \phi^{\dagger}_{s\,i}(x)T^a_{ij}\phi_{sj}(x)\right)^2 \tag{1.27}$$

Similar terms can also be written for T which are required in order to include all the fermionic degrees of freedom.

1.2.4 Higgs bosons in the Minimal Supersymmetric Standard Model

In the Standard Model, mass terms for the down type quarks are formed by coupling the scalar Higgs isospin doublet $\phi = \begin{pmatrix}\phi^+\\ \phi^0\end{pmatrix}$to the left handed quark isospin doublet $q_L = \begin{pmatrix}u_L\\ d_L\end{pmatrix}$ and the right handed down quark singlet d_R, such as $q^{\dagger}_L\gamma_0\phi d_R$. Similarly masses to the down type quarks are formed by coupling the conjugate Higgs doublet $\tilde{\phi} = i\sigma_2\phi^*$ to q_L and the right handed up quark singlet u_R, such as $q^{\dagger}_L\gamma_0\tilde{\phi}u_R$. This formulation however is problematic when building a SUSY invariant Lagrangian, as ϕ would be associated to a chiral superfield Φ and $\tilde{\phi}$ would be associated to $\Phi^{\dagger}$, thus making the Higgs superpotential terms in $W(\Phi)$ non-chiral and hence breaking SUSY as discussed in Section 1.2.1. The simplest solution is to include a second Higgs superfield containing a second Higgs doublet to give mass to up type quarks. Therefore one can define two chiral superfield doublets $\Phi(H_u) = \begin{pmatrix}\Phi(H^+_u)\\ \Phi(H^0_u)\end{pmatrix}$ and $\Phi(H_d) = \begin{pmatrix}\Phi(H^0_d)\\ \Phi(H^-_d)\end{pmatrix}$. What remains is to specify the form of the superpotential W_{EWK}. The MSSM is specified by the choice

$$W_{EWK} = y^{ij}_u U^c_i Q_j\cdot\Phi(H_u) - y^{ij}_d D^c_i Q_j\cdot\Phi(H_d) - y^{ij}_l E^c_i L_j\cdot\Phi(H_d) + \mu\Phi(H_u)\cdot\Phi(H_d) \tag{1.28}$$

where L_j are chiral superfield doublets $\begin{pmatrix}\nu_{eL}\\ e_L\end{pmatrix}$, $\begin{pmatrix}\nu_{\mu L}\\ \mu_L\end{pmatrix}$, $\begin{pmatrix}\nu_{\tau L}\\ \tau_L\end{pmatrix}$, Q_j are chiral superfield doublets for $\begin{pmatrix}u_L\\ d_L\end{pmatrix}$, $\begin{pmatrix}c_L\\ s_L\end{pmatrix}$, $\begin{pmatrix}t_L\\ b_L\end{pmatrix}$, E_j^c are chiral superfield singlets for $e\,,\mu\,,\tau$ with c denoting complex conjugation and are interpreted as containing left handed components of anti-fermions as discussed in Section 1.2.3, D_j^c, U_j^c are chiral superfield singlets for down and up type quarks respectively with c denoting complex conjugation and are also interpreted as containing left handed components of anti-fermions. The "$\cdot$" denotes an $SU(2)$ contraction between two doublets with metric $i\sigma_2$ i.e $Q_j \cdot \Phi(H_u) := Q_j i\sigma_2 \Phi(H_u)$. $y_u\,, y_d\,, y_l$ are 3x3 matrices in family or generation space representing the Yukawa coupling strengths of the Standard Model. Finally the final term in Equation (1.28), called the "μ" term, represents the only SUSY invariant coupling between the two Higgs chiral superfield doublets and gives rise to quadratic scalar Higgs couplings.

Electro-Weak symmetry breaking in MSSM

To break EWK symmetry we need first to collect all the terms containing the scalar Higgs fields which contribute to the scalar potential V_H. These arise from three sources

$$\begin{aligned}
&[\mu\Phi(H_u)\cdot\Phi(H_d)]_F \\
&[\Phi(H_u)^\dagger e^{igT^aW^a+i\frac{g'}{2}B}\Phi(H_u) + \Phi(H_d)^\dagger e^{igT^aW^a-i\frac{g'}{2}B}\Phi(H_d)]_D \\
&m_{H_u}^2(|H_u^+|^2+|H_u^0|^2) + m_{H_d}^2(|H_d^0|^2+|H_d^-|^2)\ ,\ b(H_u^+H_d^- - H_u^0H_d^0) + h.c
\end{aligned} \tag{1.29}$$

The first equation of (1.29) comes from the "μ" term of Equation (1.28). The second equation comes from the effective potential of Equation (1.27) for the Higgs chiral superfield gauge interactions described in Section 1.2.3 but applied to an $SU(2)\times U_Y(1)$ gauge group $T^a = \frac{1}{2}\sigma^a$, W^a and g are the generators, the gauge fields and coupling constant of $SU(2)$ respectively. B and g' are the $U_Y(1)$ gauge field and hypercharge coupling constant respectively. $\Phi(H_u)$ and $\Phi(H_d)$ have opposite hypercharges so that the "μ" term is $U_Y(1)$ invariant. The third equation of (1.29)

comes from soft SUSY breaking terms as described in [35] where the constant b can be taken to be real by allowing $(H_u^0 H_d^0)$ to absorb the imaginary phase of b. Putting all these terms together, the Higgs potential V_H can be written in terms of the constituent scalar fields H_u^+, H_u^0, H_d^-, H_d^0 as

$$\begin{aligned} V_H &= (m_{H_u}^2 + |\mu|^2)(|H_u^+|^2 + |H_u^0|^2) + (m_{H_d}^2 + |\mu|^2)(|H_d^-|^2 + |H_d^0|^2) + \\ &+ [b(H_u^+ H_d^- - H_u^0 H_d^0) + h.c] + \frac{g^2 + g'^2}{8}(|H_u^+|^2 + |H_u^0|^2 - |H_d^-|^2 - |H_d^0|^2)^2 + \\ &+ \frac{g^2}{2}|H_u^+ H_d^{\dagger 0} + H_u^0 H_d^{-\dagger}|^2 \end{aligned} \tag{1.30}$$

In the MSSM case we have two Higgs doublets $H_u = \begin{pmatrix} H_u^+ \\ H_u^0 \end{pmatrix}$ and $H_d = \begin{pmatrix} H_d^0 \\ H_d^- \end{pmatrix}$. Therefore as the Lagrangian is $SU(2)$ invariant we can apply an $SU(2)$ rotation such that one of the doublets obtains a more simple form to deal with at the vacuum. The convention is to chose a transformation such that $(H_u^+)_{vev} = 0$. Then considering $\left(\frac{\partial V_H}{\partial H_u^+}\right)_{H_u^+=0}$ implies at the minimum V_H $(H_d^-)_{vev} = 0$ or $b + \frac{g^2}{2} H_d^{0\dagger} H_u^{0\dagger} = 0$. The former condition is accepted as it leads to preserving $U_{EM}(1)$ symmetry. Therefore at the minimum V_H is only made up of electrically neutral Higgs components. Another interesting point is that in contrast to the Standard Model, in the MSSM the quartic Higgs coupling constant is completely determined by the electro-weak couplings. If we also require $\left(\frac{\partial V_H}{\partial H_u^0}\right)_{vev} = \left(\frac{\partial V_H}{\partial H_d^0}\right)_{vev} = 0$ for V_H to be minimised at the vacuum then $(H_u^0 H_d^0)_{vev} \in \Re^+$. We can further simplify things by making the observation that since $(H_u^0 H_d^0)_{vev} \in \Re^+$, $(H_u^0)_{vev}$ and $(H_d^0)_{vev}$ have equal and opposite complex phases. Therefore we could apply a $U_Y(1)$ rotation simultaneously to both $(H_u^0)_{vev}$ and $(H_d^0)_{vev}$ such that $(H_u^0)_{vev} \in \Re^+$,$(H_d^0)_{vev} \in \Re^+$ since they have opposite sign hypercharges. In order to ensure that V_H is bounded from below for the special case that $(H_u^0)_{vev} = (H_d^0)_{vev}$, we must require the quadratic term coefficient to be positive therefore

$$2|\mu|^2 + m_{H_u}^2 + m_{H_d}^2 > 2b \tag{1.31}$$

As $b > 0$ this means that $|\mu|^2 + m_{H_u}^2$ and $|\mu|^2 + m_{H_d}^2$ cannot be simultaneously negative and therefore since $\left(\frac{\partial^2 V_H}{\partial H_{u,d}^{0\ 2}}\right)_{\substack{H_u=0 \\ H_d=0}} = 2(|\mu|^2 + m_{H_{u,d}}^2)$, the point $(H_u^0)_{vev} = (H_d^0)_{vev} = 0$ cannot be a maximum of V_H. We also want to ensure that $(H_u^0)_{vev} = (H_d^0)_{vev} = 0$ is

not a minimum of V_H as then no symmetry breaking will occur. Therefore we must require $\frac{\partial^2 V_H}{\partial H_u^{0\,2}}\frac{\partial^2 V_H}{\partial H_d^{0\,2}} - \frac{\partial^2 V_H}{\partial H_u^0 \partial H_d^0} < 0$ for the point $(H_u^0)_{vev} = (H_d^0)_{vev} = 0$. This gives

$$(|\mu|^2 + m_{H_u}^2)(|\mu|^2 + m_{H_d}^2) < b^2 \tag{1.32}$$

W and Z masses in MSSM

The masses of the W and Z bosons come from the covariant kinetic terms of the Higgs fields

$$\begin{aligned}\mathcal{L}_H^{Kin} &= [(\partial^m + igT^a W^{ma} + ig'B^m)H_u]^\dagger(\partial_m + igT^a W_m^a + ig'B_m)H_u + \\ &+[(\partial^m + igT^a W^{ma} - ig'B^m)H_d]^\dagger(\partial_m + igT^a W_m^a - ig'B_m)H_d \end{aligned} \tag{1.33}$$

where $T^a = \sigma^a/2$. By working in the unitary gauge [23] and considering fluctuations around $\begin{pmatrix}(H_d^0)_{vev}\\ 0\end{pmatrix}$ and $\begin{pmatrix}0\\ (H_u^0)_{vev}\end{pmatrix}$ and remembering that $Z^m = (-g'B^m + gW_3^m)/\sqrt{(g'^2+g^2)}$ we can write

$$\begin{aligned} m_Z^2 &= \frac{1}{2}(g^2+g'^2)((H_d^0)_{vev}{}^2 + (H_u^0)_{vev}{}^2) \\ m_W^2 &= \frac{1}{2}g^2((H_d^0)_{vev}{}^2 + (H_u^0)_{vev}{}^2) \end{aligned} \tag{1.34}$$

From (1.34) we see that

$$((H_d^0)_{vev}{}^2 + (H_u^0)_{vev}{}^2) = (\frac{2m_W^2}{g^2})^{1/2} = 174\,GeV \tag{1.35}$$

and we can define $\tan\beta := (H_u^0)_{vev}/(H_d^0)_{vev}$. Using $\left(\frac{\partial V_H}{\partial H_u^0}\right)_{vev} = \left(\frac{\partial V_H}{\partial H_d^0}\right)_{vev} = 0$ we can write

$$\begin{aligned}(|\mu|^2 + m_{H_u}^2) &= b\cot\beta + \tfrac{m_Z^2}{2}\cos 2\beta \\ (|\mu|^2 + m_{H_d}^2) &= b\tan\beta - \tfrac{m_Z^2}{2}\cos 2\beta \end{aligned} \tag{1.36}$$

which can be used to eliminate parameters $|\mu|$ and b in favour of $\tan\beta$ but without determining the phase of μ.

MSSM tree level Higgs masses

As in the Standard Model case, the Higgs masses and fields are evaluated by considering how fluctuations around the v.e.v of the scalar fields affect V_H. However

in the MSSM due to the multiple scalar Higgs fields, in general the electro-weak Higgs eigenstates are not the physical mass eigenstates. By considering that a general mass term of a generic potential $V(\phi_1, \phi_2)$ when expanded around its minimum $(\phi_1 = v_1, \phi_2 = v_2)$ takes the form

$$-\frac{1}{2}\tilde{\phi}_i \left(\frac{1}{2}\frac{\partial^2 V}{\partial\phi_i \partial\phi_j}\right)\Bigg|_{v_1,v_2} \tilde{\phi}_j \tag{1.37}$$

where $i = 1, 2$ and $\tilde{\phi}_i = \sqrt{2}(\phi_i - v_i)$, by diagonalising $\mathbf{M} = \frac{\partial^2 V}{\partial\phi_i \partial\phi_j}\Big|_{v_1,v_2}$ we can retrieve the physical masses and eigenstates of ϕ_1 and ϕ_2. Applying this procedure to V_H and $\begin{pmatrix} \Im m\sigma_{H_u^0} - 0 \\ \Im m\sigma_{H_d^0} - 0 \end{pmatrix}$, $\begin{pmatrix} \Re e\sigma_{H_u^0} - (H_u^0)_{vev} \\ \Re e\sigma_{H_d^0} - (H_d^0)_{vev} \end{pmatrix}$, $\begin{pmatrix} \sigma_{H_u^{+\dagger}} - 0 \\ \sigma_{H_d^-} - 0 \end{pmatrix}$, where σ_H denotes the Higgs field around its corresponding v.e.v, for the last doublet we have extended Equation (1.37) to account for a complex field basis[3] and the "0"'s mean the the v.e.v was zero, we get the physical mass eigenstates

$$\begin{aligned}
A^0 &= \sqrt{2}[\cos\beta(\Im m\sigma_{H_u^0}) + \sin(\beta\Im m\sigma_{H_d^0})] \\
B^0 &= \sqrt{2}[\cos\beta(\Im m\sigma_{H_u^0}) - \sin(\beta\Im m\sigma_{H_d^0})] \\
h^0 &= \sqrt{2}[\cos\alpha(\Re e\sigma_{H_u^0} - (H_u^0)_{vev}) - \sin\alpha(\Re e\sigma_{H_d^0} - (H_d^0)_{vev})] \\
H^0 &= \sqrt{2}[\sin\alpha(\Re e\sigma_{H_u^0} - (H_u^0)_{vev}) + \cos\alpha(\Re e\sigma_{H_d^0} - (H_d^0)_{vev})] \\
H^+ &= \cos\beta H_u^+ + \sin\beta H_d^{-\dagger} \\
H^- &= \cos\beta H_u^{+\dagger} + \sin\beta H_d^- \\
G^+ &= \sin\beta H_u^+ - \cos\beta H_d^{-\dagger} \\
G^- &= \sin\beta H_u^{+\dagger} - \cos\beta H_d^-
\end{aligned} \tag{1.38}$$

where α is the mixing angle in the mass matrix of $\begin{pmatrix} \Re e\sigma_{H_u^0} - (H_u^0)_{vev} \\ \Re e\sigma_{H_d^0} - (H_d^0)_{vev} \end{pmatrix}$ and is related to other quantities by $\sin 2\alpha = -\frac{m_{A^0}^2 + m_Z^2}{m_{H^0}^2 + m_{h^0}^2}\sin 2\beta$ The eigenstates of Equation (1.38)

[3]Could have also used $\begin{pmatrix} \sigma_{H_u^+} - 0 \\ \sigma_{H_d^{-\dagger}} - 0 \end{pmatrix}$ basis and that is why we get H^- and G^-

have masses

$$
\begin{aligned}
m_{A^0} &= \sqrt{(2b/\sin 2\beta)} \\
m_B^0 &= 0 \\
m_{h^0} &= \sqrt{\frac{1}{2}(m_{A^0}^2 + m_Z^2 - [(m_{A^0}^2 + m_Z^2)^2 - 4m_{A^0}^2 m_Z^2 \cos^2 2\beta]^{1/2})} \\
m_{H^0} &= \sqrt{\frac{1}{2}(m_{A^0}^2 + m_Z^2 + [(m_{A^0}^2 + m_Z^2)^2 - 4m_{A^0}^2 m_Z^2 \cos^2 2\beta]^{1/2})} \\
m_{H^\pm} &= \sqrt{(m_W^2 + m_{A^0}^2)} \\
m_{G^\pm} &= 0
\end{aligned}
\tag{1.39}
$$

As required we ended up with 3 massless Goldstone bosons whose degrees of freedom are replaced by the longitudinal degrees of freedom of the massive $W^\pm$, Z^0 bosons. Moreover we can deduce a maximum value for the tree level mass of h_0 as $m_{h^0} \leq m_Z|\cos 2\beta|$ for $m_{A^0} \gg m_Z$. However higher order radiative increase this limit by a substantial amount depending on the rest of the MSSM parameters and explaining why h_0 has no experimental evidence [35]. Figure 1.2 shows the dependance of the MSSM Higgs masses on m_{A^0} for two $\tan\beta$ values. A near mass degeneracy is observed between m_{A^0}, m_{H^0}, $m_{H^\pm}$ for $m_{A^0} > m_h^{max}$ and between m_{A^0}, m_{h^0} for $m_{A^0} < m_h^{max}$ $\tan\beta > 3$, where m_h^{max} is the maximum allowed value for m_h^0 including the radiative corrections.

MSSM Tree level Higgs couplings to fermions and Vector Bosons

By considering the behaviour of the Yukawa couplings of Equation (1.28) in terms of the constituent fermionic fields around the Higgs field vacua fluctuations, we can deduce the tree level couplings of the MSSM Higgs bosons to fermions. Transforming to the physical mass eigenstates for the Higgs fields we can express the Yukawa coupling constants for for bottom and top like fermions as [41]

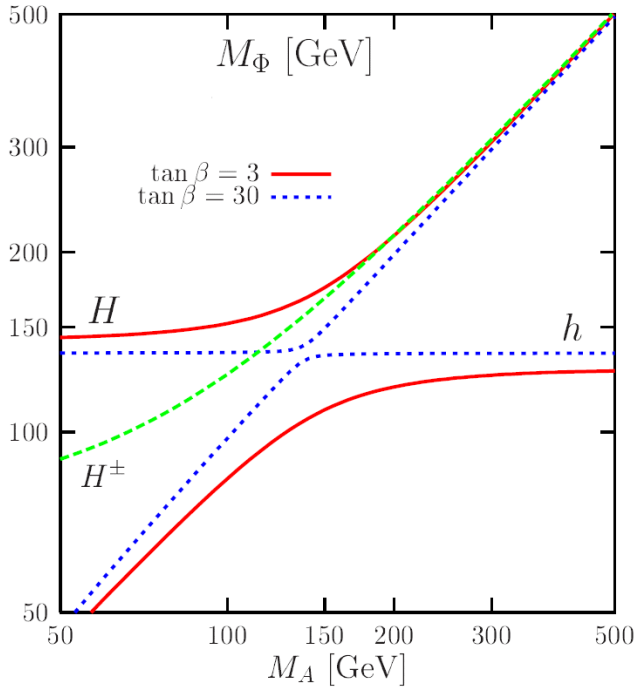

Figure 1.2: The masses of the MSSM Higgs bosons as a function of m_{A^0} for two values of $\tan\beta$= 3 and 30 [5].

$$\begin{aligned} y_b &= \tfrac{g m_b}{\sqrt{2} m_W \cos\beta} \\ y_t &= \tfrac{g m_t}{\sqrt{2} m_W \sin\beta} \end{aligned} \tag{1.40}$$

Furthermore the couplings of the physical Higgs eigenstates to bottom and top like fermions are

$$\begin{aligned} G_{htt} &= i\tfrac{m_t \cos\alpha}{v \sin\beta},\ G_{Htt} = i\tfrac{m_t \sin\alpha}{v \sin\beta},\ G_{Att} = \tfrac{m_t}{v}\cot\beta\gamma_5 \\ G_{hbb} &= -i\tfrac{m_b \sin\alpha}{v \cos\beta},\ G_{Hbb} = i\tfrac{m_b \cos\alpha}{v \cos\beta},\ G_{Abb} = \tfrac{m_b}{v}\tan\beta\gamma_5 \\ G_{H^+\bar{t}b} &= -\tfrac{i}{\sqrt{2}v} V^{bt*}[m_b \tan\beta(1+\gamma_5) + m_t \cot\beta(1-\gamma_5)] \\ G_{H^-t\bar{b}} &= -\tfrac{i}{\sqrt{2}v} V^{bt}[m_b \tan\beta(1-\gamma_5) + m_t \cot\beta(1+\gamma_5)] \end{aligned} \tag{1.41}$$

where $v = 2m_W/g$ [5] and V^{bt} is the CKM matrix factor. Similarly by considering the couplings of the vector bosons with the physical MSSM Higgs bosons appearing

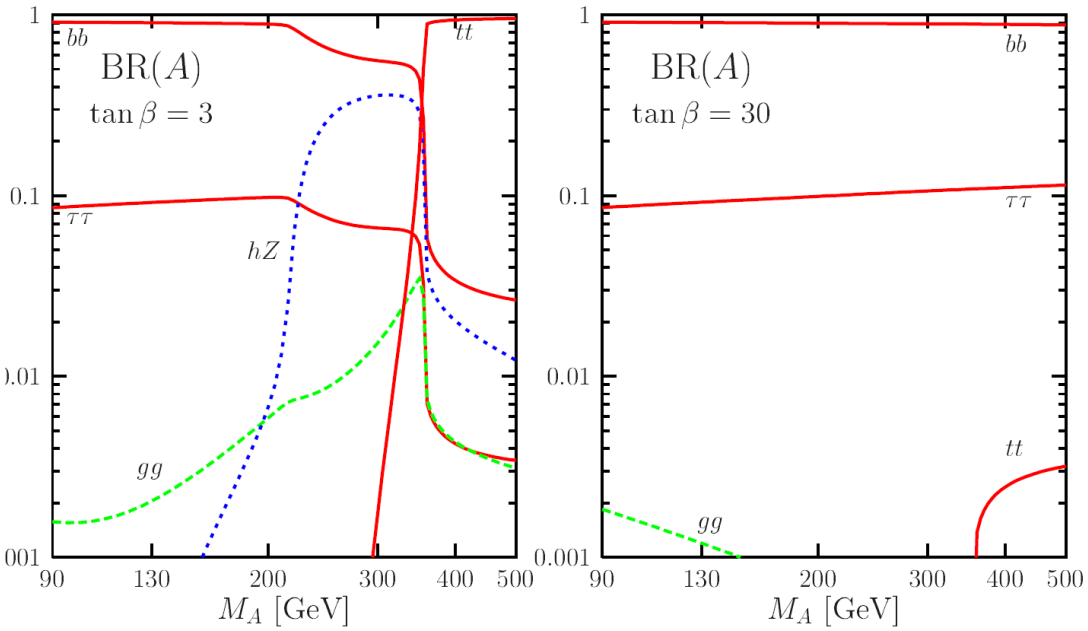

Figure 1.3: Branching ratios of various decay channels of the A Higgs boson as a function of m_A for $\tan\beta = 3$ (Left) and $\tan\beta = 30$ (Right) [5].

in Equation (1.2.4) we get

$$G_{Z_m Z_n h} = ig_Z m_Z \sin(\beta-\alpha) g_{mn},\ G_{Z_m Z_n H} = ig_Z m_Z \cos(\beta-\alpha) g_{mn}$$
$$G_{W_m^+ W_n^- h} = ig_W m_W \sin(\beta-\alpha) g_{mn},\ G_{W_m^+ W_n^- h} = ig_W m_W \cos(\beta-\alpha) g_{mn} \quad (1.42)$$

where $g_W = g$ and $g_Z = g/cos\theta_W$ (θ_W is the weak mixing angle) The ZZA, WWA, $WZH^\pm$ couplings are zero [5].

Therefore an enhancement of the bottom like fermion coupling to h, A^0, H^0 and $H^\pm$ for $\tan\beta > 1$ is obtained compared to a suppression with top like fermions and vector bosons, making Higgs couplings to the heaviest bottom like leptons (τ) and quarks (b) more important within an MSSM context as indicated in Figure 1.3 which shows the branching ratio of A as a function of m_A for $\tan\beta = 3$ and $\tan\beta = 30$.

1.2.5 Results from recent MSSM Higgs searches

Direct searches for the production of a neutral Higgs boson decaying to τ leptons were carried out at the DØ experiment at Tevatron. The results were interpreted

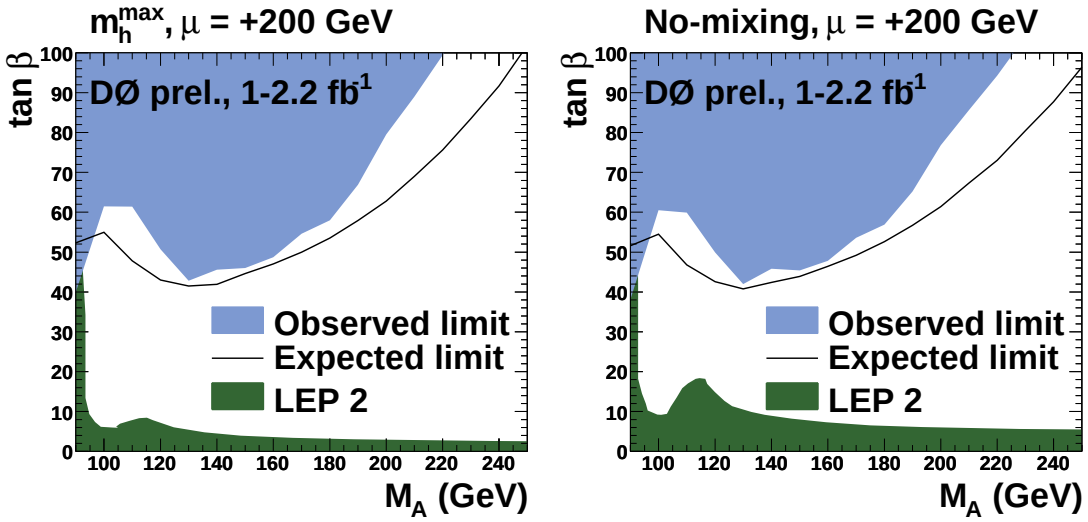

Figure 1.4: Region in the $(m_A, \tan\beta)$ parameter space that has been excluded at 95%CL in two MSSM benchmark scenarios with $|\mu| > 0$: Left m_h^{max}, Right no mixing The green shaded region is the excluded by LEP [6].

in the MSSM and exclusions limits in the $(m_A, \tan\beta)$ plane were placed for two benchmark scenarios. The m_h^{max} and no mixing scenarios differ in the radiative corrections to m_h. In the m_h^{max} scenario SUSY parameters are chosen to maximise the radiative corrections to m_h whereas in the no mixing scenario these corrections are much smaller. Figure 1.4 shows the region in the $(m_A, \tan\beta)$ parameter space that has been excluded at 95%CL in two MSSM benchmark scenarios with $|\mu| > 0$: left, m_h^{max} and right, no mixing. Shown also by the green shaded region is the excluded region by LEP [6].

1.3 Z production at the LHC

At leading order the simplest Z production at LHC occurs by the process $q\bar{q} \rightarrow$Z. However the contribution of Z production from qg or gg scattering to the total Z production cross-section depends on the momentum fraction x carried by the scattering partons[42]. Figure 1.5 shows the kinematic plane for LHC parton kinematics for various scattering scales Q^2 at centre of mass energy $\sqrt{s} = 14\,\text{TeV}$ [7]. Hence to produce a Z within $(|y| < \pm 2.5)$ whose decay products $(e^{\pm})$ lie within the detectable acceptance, one requires the x of the scattering partons to lie within $10^{-4} < x < 0.1$.

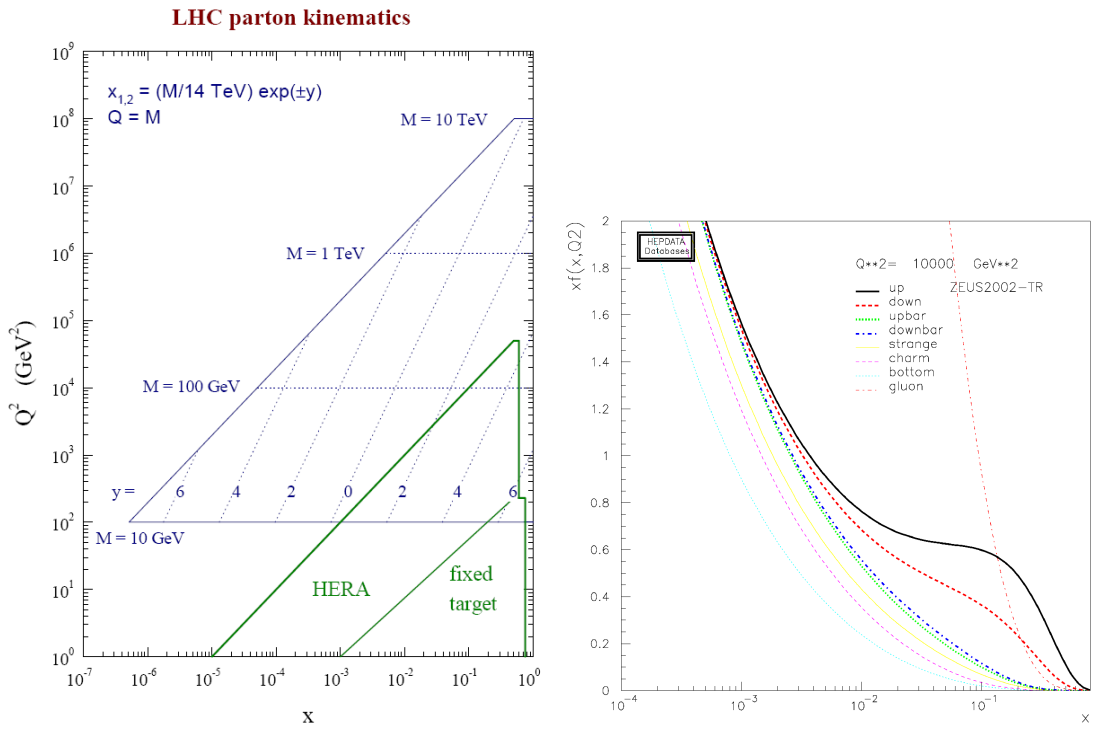

Figure 1.5: Left:LHC parton kinematics at various Mass (Q) scales and rapidities. The blue shaded area is evaluated for the LHC energy of $\sqrt{s} = 14\,\text{TeV}$ [7] Right:PDF distributions as a function of x for $Q^2 = 10000\,\text{GeV}^2$ [7].

This means that the dominant parton in the scattering process will be the gluon as shown in Figure 1.5 [43].

Tree level Feynman diagrams showing the Z production via $q\bar{q}$, gg or gq scattering are shown in Figure 1.6. The outcoming quark or gluons in the gq or gg scattering will hadronise producing jets alongside the Z.

The Z production cross-section times the branching ratio to electrons as a function of $\sqrt{s}$ is shown in Figure 1.7. At $\sqrt{s} = 14\,\text{TeV}$ the expected cross-section is $\sim 2\,\text{nb}$ at NNLO [8].

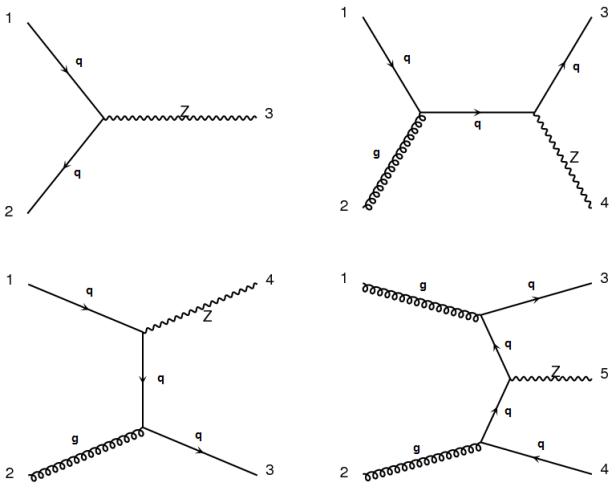

Figure 1.6: Tree level Z production Feynman diagrams at LHC. The dominant $q\bar{q}$ scattering is followed by gq and gg scattering.

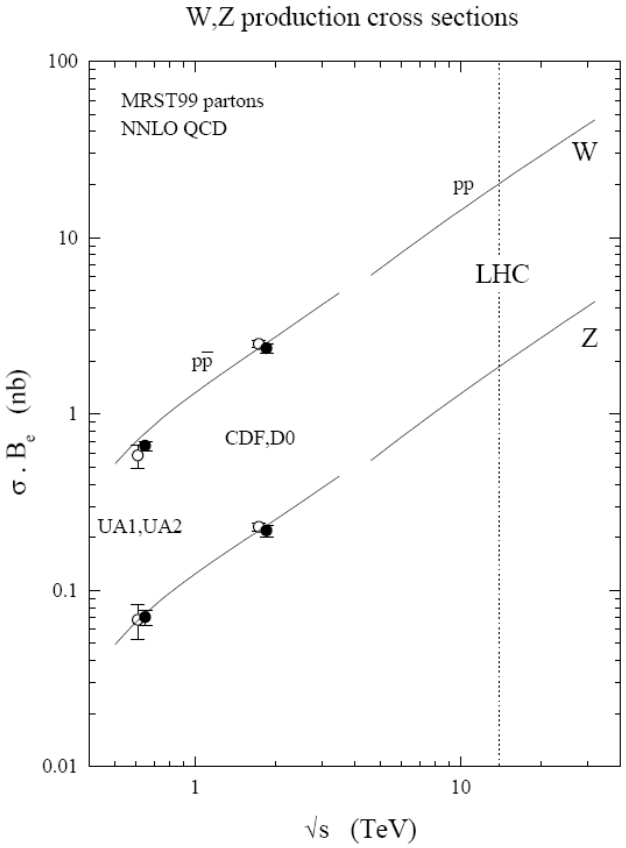

Figure 1.7: W and Z NNLO production cross sections multiplied by Branching ratio to an electron pair as a function of $\sqrt{s}$. The points denote experimental measurements before 1999 [8].

Decay Products	Branching Fraction
$e^-+\bar{\nu}_e+\nu_\tau$	(17.84±0.05)%
$\mu^-+\bar{\nu}_\mu+\nu_\tau$	(17.36±0.05)%
$1\pi+n\pi^0+\nu_\tau$	49.2%
$3\pi+n\pi^0+\nu_\tau$	14.6%

Table 1.2: Table summarising the main τ^- lepton decays [19].

1.4 τ-lepton decays

The τ lepton discovered in 1975 at SLAC [44] has a mass of 1.78 GeV/c^2 and a lifetime of the order of 291×10^{-15} s [19]. A τ with 100 GeV/c of momentum will travel $\sim$ 5 mm distance before decaying. Therefore the identification has to be made from their subsequent decays that remain stable in the scope of the detector. A τ lepton decays weakly, $\sim$ 35% of the time to either an electron or a muon accompanied by a τ and an electron or muon neutrino respectively, and 65% to hadrons, predominantly $\pi^\pm$ and π^0, which form a τ-jet accompanied by a τ neutrino. Out of these hadronic τ lepton decays, 77% contain one charged particle (1 prong) and the rest contain mainly three charged particles (3 prong). Table 1.2 summarises these branching fractions for a τ^- lepton.

Chapter 2

The CMS experiment

2.1 The Large Hadron Collider

Tha Large Hadron Collider (LHC) [45] is a 27 km circumference proton or heavy ion accelerator at CERN due to start operating in 2009. It is designed to accelerate and collide proton beams at a centre of mass energy ($\sqrt{s}$) of 14 TeV. There are four main experiments which will take place at the LHC: two with general purpose detectors, ATLAS (A Toroidal Lhc ApparatuS) [46] and CMS (Compact Muon Solenoid) [11], and two with dedicated detectors, ALICE (A Large Ion Collider Experiment) [47] and LHCb (the Large Hadron Collider Beauty experiment) [48].

Before protons reach the LHC ring, they are initially accelerated by linear accelerators (LINAC). The Proton Synchrotron (PS) provides a $\sim$ 25 GeV beam with the desired bunch structure. These proton beams are then pre-accelerated using the Super PS (SPS) to 450 GeV and injected into the LHC ring for clockwise and anti-clockwise acceleration to the nominal energy of 7 TeV as shown in Figure 2.1.

Inside the LHC accelerator, the particles circulate in opposite directions in two separate beam pipes. The diameter of the beam is reduced by focusing magnets before it enters every experimental interaction point to achieve high luminosity collisions. Within the LHC dipole, these two beam pipes are surrounded by shells of superconducting coils creating the magnetic field which guides the beams to follow a circular path. The entire dipole rests inside a cryogenic vessel.

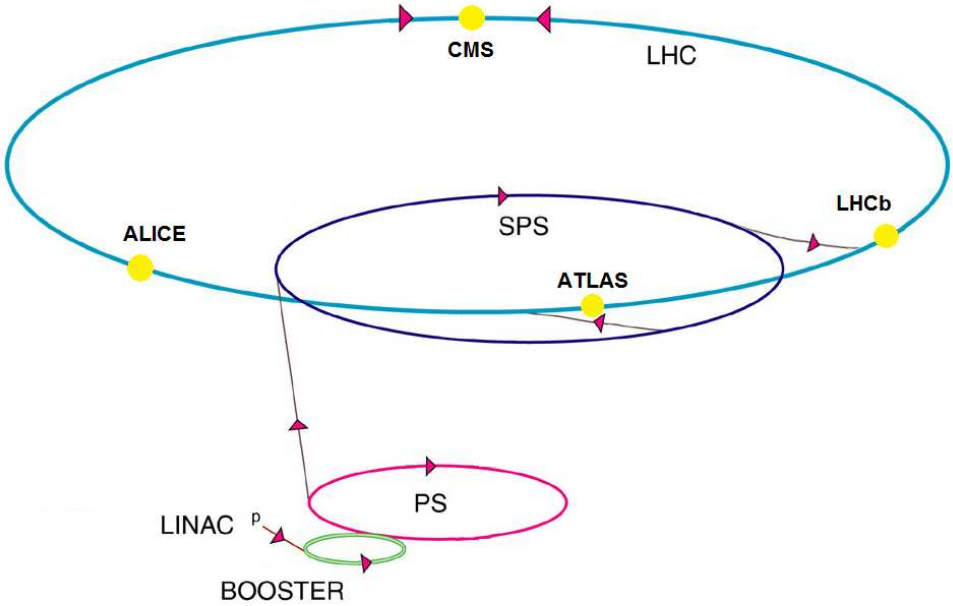

Figure 2.1: The LHC accelerator complex.

The particles within the beam are grouped in cylindrical bunches with a nominal interaction diameter of $\sim 16\,\mu$m, a length of $\sim 8\,$cm and a nominal bunch separation of 25 ns. However out of the available 3564 spaces during a single LHC cycle only 2808 bunches will be filled with protons.

The design instantaneous luminosity is $10^{34}\,\mathrm{cm}^{-2}\mathrm{s}^{-1}$. Using this value, taking the total p-p inelastic (including double-diffractive) cross-section at $\sqrt{s} = 14\,$TeV as 70 mb and a 25 ns bunch spacing, approximately 20 p-p inelastic interactions will occur per crossing, where a factor of 0.8 was used to account for the empty bunches. In addition, the short bunch spacing of 25 ns results in further "pile-up", which comes from the soft remnants overlapping from the two previous bunch crossings and some early effects from the subsequent one.

During the first physics runs the beam parameters are expected to change. The beam energy is to be lowered to 5 TeV, the bunch diameter increased to $\sim 32\,\mu$m with a bunch spacing of 75 ns and a total of 936 bunches per LHC fill. The instantaneous luminosity will decrease to $10^{32}\,\mathrm{cm}^{-2}\mathrm{s}^{-1}$ and $\mathrm{O}(100\,\mathrm{pb}^{-1})$ of data will be collected followed by a shut-down period. The full beam energy of 7 TeV will be used once the LHC comes back on-line, after the first shut-down. Table 2.1 summarises some of these values.

Beam Parameter	p-p Nominal	p-p First Phys. Run	Units
Energy at collision	7	5	TeV
N protons per bunch	1.15×10^{11}	4×10^{10}	-
N Bunches	2808	936	-
Bunch Spacing	25	75	ns
Beam Diameter	16	32	μm
Inst. Lumi.	10^{34}	10^{32}	$\mathrm{cm}^{-2}\mathrm{s}^{-1}$

Table 2.1: Table summarising some of the LHC parameters for nominal and first physics runs [9].

2.2 The CMS detector

2.2.1 General Overview

The Compact Muon Solenoid (CMS) as shown in figure 2.2 is a hermetic general purpose detector with a 4 T super-conducting solenoid in order to achieve a good momentum resolution. This 13 m long 5.9 m inner diameter magnet accommodates the tracker and both the electromagnetic and hadronic calorimeters in its centre. Three different types of muon detectors are placed on the outside of the magnet ensuring full geometric coverage.

The coordinate convention adopted in CMS has the origin at the nominal collision point in the centre of the detector. The y-axis points vertically upwards, the x-axis points radially inwards towards the centre of the LHC ring and the z-axis points along the beam direction towards the Jura Mountains. The polar angle θ is measured with respect to the z-axis and is used to define the pseudo-rapidity $\eta = -ln\tan(\theta/2)$. The azimuthal angle ϕ is measured with respect to the x-axis. The energy fraction and momentum component transverse to the direction of the beam are denoted as $\mathrm{E_T} = \mathrm{E}\sin\theta$ and $\mathrm{p_T} = \sqrt{(\mathrm{p_x^2} + \mathrm{p_y^2})}$ respectively. Finally the imbalance of energy measured in the transverse place is denoted by $\mathrm{E_T^{miss}}$.

CMS has been designed to cover a wide range of physics interests. Some main topics are the search for the Higgs Boson(s) within a Standard Model context or otherwise, the search for SUSY particles, new massive vector bosons and the search for extra dimensions.

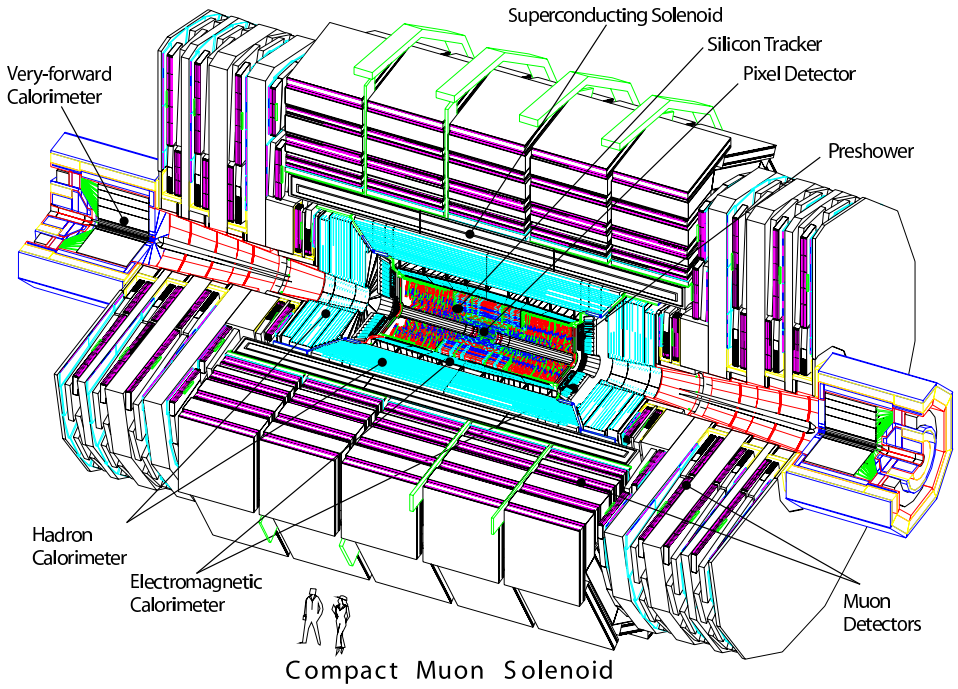

Figure 2.2: A cut away view of the CMS detector.

However before such searches take place, it is important to ensure that Standard Model results are reproduced. Therefore during the initial stages of data taking there will be a major effort to measure standard candles involving W and Z bosons. In this context, Z$\rightarrow \tau\tau$ decays are important, as they provide a test bench for analogous H$\rightarrow \tau\tau$ searches and can can be used to measure the τ-jet selection efficiencies, which is vital in extracting the Higgs production cross section and branching ratio and therefore essential in determining potential MSSM parameters such as $\tan\beta$.

The high crossing rate, which reaches 10^9 inelastic events per second (for nominal LHC operation), provides significant experimental challenges. These challenges are:

- The reduction of the number of events stored to disk, from approximately 10^9 events per second to 10^2 events and is dealt by using an event selecting trigger.

- At the design luminosity an average of 20 inelastic collisions will be overlayed onto the same event. In order to reduce the effect of pile-up and uncover the

collision of interest, detector subsystems with large number of channels and fast timing response have been employed.

- The high radiation environment requires radiation hard detectors and electronics to be used.

The following sections describe each of the sub-detectors of CMS starting from the inner most sub-detector closest to the beam pipe and moving radially outwards.

2.2.2 The CMS Tracking System

The purpose of the tracking system is to perform a precise measurement of the trajectories of charged particles to measure their momenta (with the help of the magnetic field) and to provide a precise reconstruction of their vertices both at trigger level and offline. Its design is also motivated by the requirement to be able to withstand the high radiation environment of the LHC. Furthermore since at the design LHC luminosity there will be 1000 particles originating from more than 20 overlapping interaction points every 25 ns, a high granularity and fast response detection system is required. This requires high power density electronics which in turn requires efficient cooling. This is in conflict with the requirement that the tracker must minimise its material budget, as the effect of multiple scattering, photon conversions, nuclear interactions and bremsstrahlung affects the performance of the detector as a whole [11]. The material budget of every tracker subsystem in terms of radiation lengths is shown in Figure 2.5. The material budget peaks at $1.8\,\mathrm{X}_o$ for $|\eta| = 1.4$.

The Pixel Detector

The pixel detector shown in Figure 2.3 is the first detection layer surrounding the beam pipe. It consists of three concentric cylindrical layers of pixel detectors placed

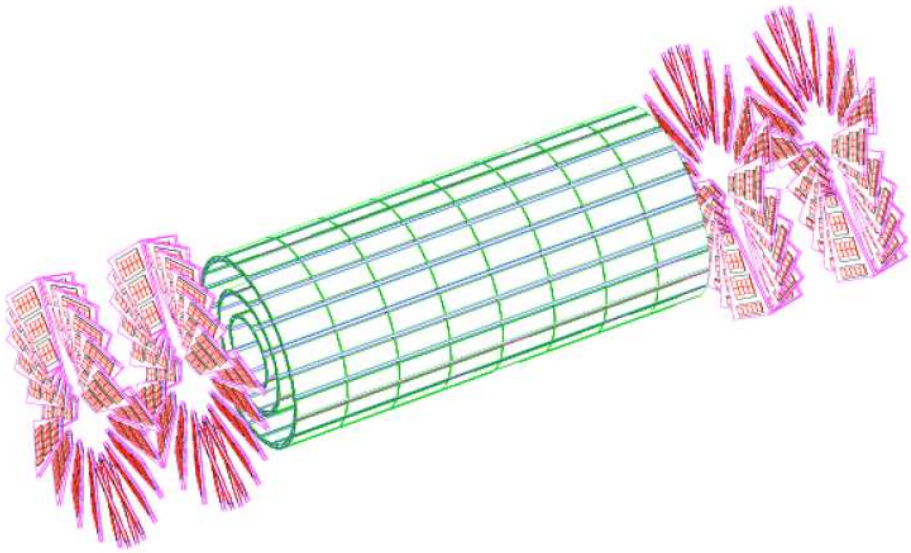

Figure 2.3: A schematic view of the pixel CMS pixel detector. The three barrel layers and end-cap disks are clearly visible [9].

at the radii of 4.4 cm, 7.3 cm and 10.2 cms respectively forming the "pixel barrel" which has a length of 53 cm. The pixel detector also has "pixel end-cap disks" placed on each end of the pixel barrel at 34.5 cm and 46.5 cm from the interaction point in order to extend the rapidity coverage up to $|\eta|$ <2.4. The pixel detector offers a high three-dimensional spatial resolution and it is ideal for the identification of primary vertices and track seeding. This is achieved by using rectangular pixels of dimensions $150\times100\,\mu\text{m}^2$, giving a total 66×10^6 pixels across the whole subsystem. The longitudinal vertex resolution is 30-40 μm in $t\bar{t}$ events where tracks made up of pixel triplet hits were used.

The Silicon Strip Tracker

Surrounding the pixel detector is the silicon strip tracker shown in Figure 2.4. It has a length of 5.2 m and a diameter of 2.5 m. As the name suggests the tracker is made up of silicon micro-strip sensors positioned to form layers of cylindrical barrels and endcap disks. It consists of a total of 10 layers up to a radius of 108 cm in the barrel. Each of the endcaps contains 12 layers. The silicon strip tracker is divided into four subsections the Tracker Inner Barrel (TIB), Tracker Outer Barrel (TOB), the

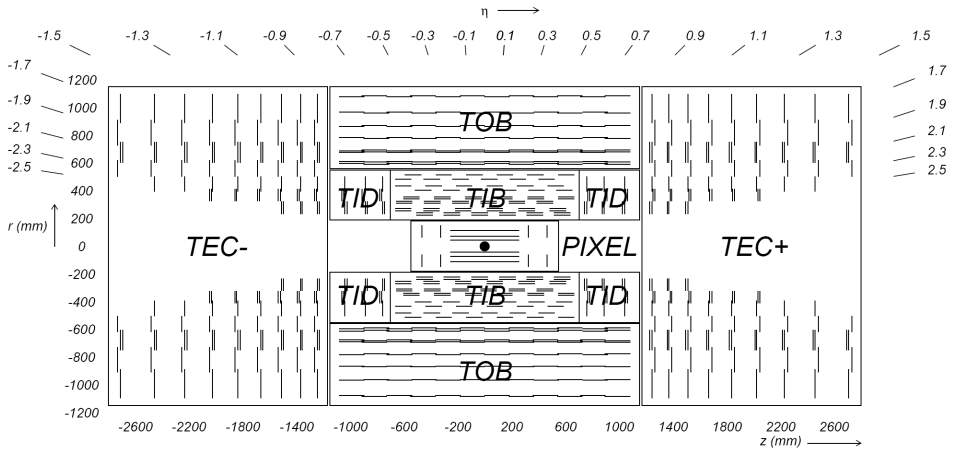

Figure 2.4: A schematic r-z view of the CMS tracker including the pixel detector. All the tracking subsystems are denoted and their coverage both in z and η is shown. Each line represents a detector module [10].

Module type	number of strips	width	length	thickness
TIB (inner two layers)	768	61.5 mm	116.9 mm	320 μm
TIB (outer two layers)	512	61.5 mm	116.9 mm	320 μm
TOB (inner four layers)	512	93.9 mm	91.6 mm	500 μm
TOB (outer two layers)	768	93.9 mm	91.6 mm	500 μm

Table 2.2: Parameters for different types of the Silicon Strip Tracker Barrel. Dimensions are for active sensor regions [20].

Tracker Inner Disks (TID) and the Tracker End Cap (TEC). The barrel part of the Strip Tracker consists of four layers of TIB modules and six layers of TOB modules which are rectangular in shape and containing different number of strips depending on the radii to keep occupancy low (O(1%) per LHC crossing) and ensuring a good hit position resolution. The inner two layers of the TIB and TOB modules are double sided with two back-to-back sensors angled at 100 mrad to provide precise two dimensional hit detection. Table 2.2 summarises these parameters. The performance of the combined Pixel and Silicon Strip Tracker gives $> 95\%$ reconstruction efficiency with p_T resolution of 1-2% and longitudinal and transverse Impact Parameter (IP) resolution of 100 μm and 20 μm respectively for muons with $p_T \in [10, 100]$ GeV/c. A full description of the tracker can be found in [11].

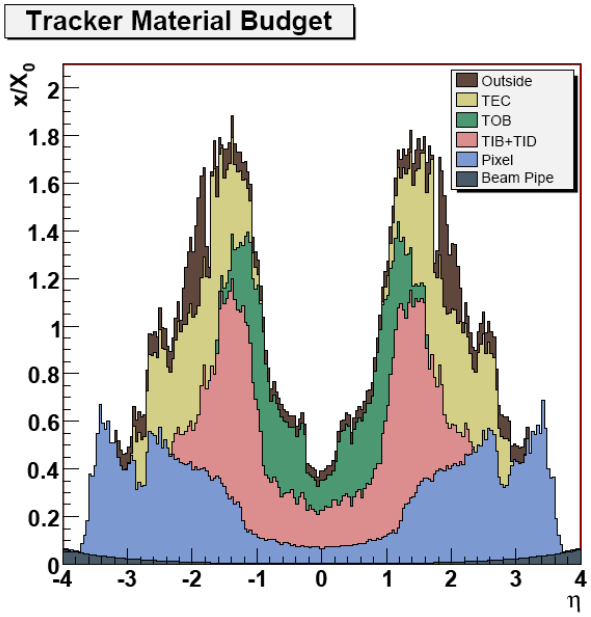

Figure 2.5: The tracking system material budget in terms of radiation lenghts as a function of η [11].

2.2.3 The Electromagnetic calorimeter

The Electromangetic calorimeter (ECAL) of CMS is a hermetic, homogenous calorimeter made out of lead-tungstate crystals ($PbWO_4$). Its aim is to reconstruct the energy of electromagnetic objects such as electrons and photons, including the electromagnetic component of hadronic and τ-jets. The design of the CMS ECAL is mainly motivated by the ability to detect $H \rightarrow \gamma\gamma$ events which requires a high granularity and high resolution detection system to be able to correctly reconstruct the two photons.

The barrel (EB) consists of 61200 crystals and each endcap (EE) consists of 7324 crystals. The short radiation lengths and Moliere radii of the crystals, summarised on Table 2.6, allow for a compact high granularity design that can fit within the solenoid. Furthermore the crystals have a scintillation light decay time of the order of the LHC bunch crossing time (25 ns) and can withstand high radiation doses of up to 10 Mrad making them ideal to operate within the LHC conditions. The limited light yield of the crystals (30 photons/MeV) requires photo-detectors that can operate within a high magnetic field (4 T) and high radiation environment in

Property	Barrel	End-cap
Density [g/cm^3]	8.28	
Radiation Length(X_o)[mm]	89	
Moliere Radius [mm]	22	
No. X_o	25.8	24.7
Front Area [mm^2]	22×22	28.6×28.6
Length [mm]	230	220

Figure 2.6: Table summarising the ECAL crystal properties.

order to amplify the signal. For this purpose Avalanche Photo Diodes and Vaccum Photo Triodes are used at the ECAL barrel and endcap respectively. The crystals are mounted so that their axes form a 3° angle with respect to the vector from the nominal interaction vertex to the crystal front surface. This is done to avoid particle trajectories aligning with ECAL cracks. The coverage of the ECAL barrel and endcaps are $|\eta|$ <1.479 and 1.479< $|\eta|$ <3.0 respectively as shown in Figure 2.7. A preshower detector, made up of two strips of silicon strip detectors lying behind disks of lead absorber, is placed in front of the endcaps in order to further discriminate against π^0's whose energies are higher in this region (compared to the barrel) resulting in pairs of photons whose angular separation is smaller than the ECAL endcap granularity.

The resolution of the ECAL is described by the width of a gaussian distribution parametrised by the reconstructed energy as shown in Equation 2.1

$$\left(\frac{\sigma}{E}\right)^2 = \left(\frac{S}{\sqrt{E}}\right)^2 + \left(\frac{N}{E}\right)^2 + C^2 \tag{2.1}$$

The first term (S) is called the stochastic term and mainly accounts for the photo-statistics and fluctuations in the lateral shower containment. The second term (N) is called the noise term and accounts for the electronic, digitisation and pile-up noise. The third term (C) is called the constant term and accounts for the non-uniformity of the light collection, the inter-calibration errors and the leakage of energy from the back of the crystal. Figure 2.8 shows the ECAL energy resolution for various electron energies. These results where obtained from test-beam, by summing over a region of 3x3 crystals around the impact point of the beam on the calorimeter which was

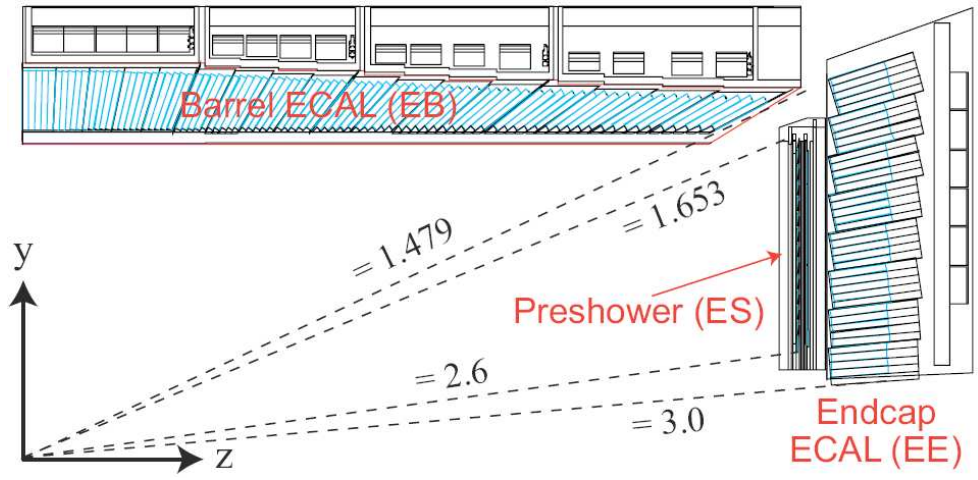

Figure 2.7: View of ECAL geometrical configuration [11].

restricted to a region of 4x4 mm^2. The data were fitted with the resolution function of Equation 2.1 giving S=2.8% GeV$^{\frac{1}{2}}$, N=0.12% GeV, C=0.3%. The resolution for a 100 GeV electron is 0.4%.

2.2.4 The Hadronic Calorimeter

The ECAL is surrounded by a brass/scintilator sampling Hadronic Calorimeter (HCAL) for $|\eta| < 3$, followed by an iron/quartz HCAL in the forward region $3 < |\eta| < 5$. The HCAL combined with the ECAL are responsible for measuring the energies of hadronic jets as well as neutrinos and exotic particles which exhibit their presence as missing energy. It is divided into four regions, the Barrel (HB) the End-cap (HE) which lie inside the solenoid, the Forward (HF) and the Outer (HO) which lie outside. Figure 2.9 shows a quarter r-z view of the various HCAL components and their η coverage.

The HB and HE have a coverage of $|\eta| < 1.3$ and $1.3 < |\eta| < 3$ respectively and have an η,ϕ segmentation of (0.087,0.087) except from near $|\eta|$ =3 where it is doubled. The effective thickness of the HB varies between $5.82\lambda_I$ at η =0 and $10.6\lambda_I$ at $|\eta|$ =1.3 with the ECAL adding a further of $1.1\lambda_I$, where λ_I =16.42 cm. The HE has a thickness of 1.8 m and including the ECAL it is about $10\lambda_I$. The HB has a single longitudinal readout apart from the HB-HE interface where there are

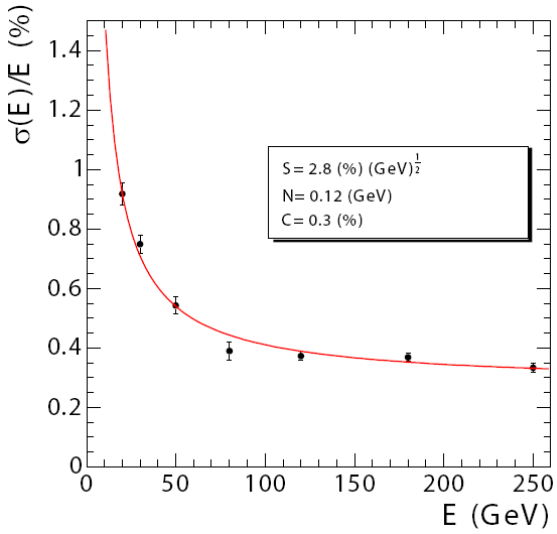

Figure 2.8: The ECAL resolution for various electron energies obtained from testbeam [11]. The data were fitted with the resolution function of Equation 2.1.

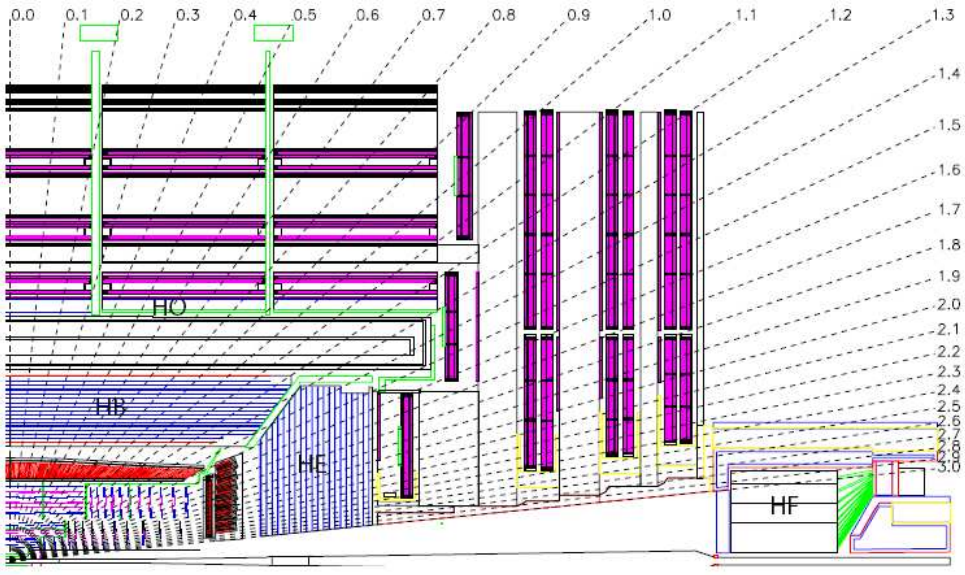

Figure 2.9: Quarter r-z view of the CMS detector with the various HCAL components denoted as HB, HE, HF, HO. The dashed lines denoted fixed η values [11].

two read-out layers. In contrast to the HB, the HE has a longitudinal segmentation which is partially motivated by the radiation environment and the ability to apply correction factors for the calibration coefficients after degradation of the scintillators has occured. The HE towers nearest to the beam line, have three readout layers in depth. The rest of the towers apart from the ones that overlap with the EB, have two readout layers for potential use during a time period where the EE might not be available.

In the central rapidity region the combined stopping power of the EB and HB is not sufficient to contain hadronic showers, hence the HO utilises the solenoid to add $1.4/\sin\theta\lambda_{\mathrm{I}}$ of interaction lengths. It comprises of five rings of sensitive material along the z-axis, placed on the five rings of iron which act as the magnet's return yoke. Furthermore as the HB has the smallest depth at η=0 , two sensitive HO layers are placed on either side of the central iron ring of the return yoke, called the "tail-catcher iron". The total depth of the calorimeter is thus extended to a maximum of $11.8\lambda_{\mathrm{I}}$. The segmentation of the HO is (0.087,0.087) in η,ϕ to match that of the HB.

The design of the HF is motivated by the large particle fluxes which deposit an average of 760 GeV per proton-proton interaction on both HF's compared to 100 GeV on the rest of the calorimeter. Quartz fibres as the active medium and the signal is generated when charged particles generate Cerenkov light making the HF mostly sensitive to the EM component of showers. The fibres are parallel to the beam line and are bundled to (0.175,0.175) η,ϕ towers.

The response of the CMS HCAL to the electromagnetic and hadronic part of the shower, deviates from unity leading to a non-linear energy response. The resolution of the combined CMS HCAL+ECAL on incident charged hadrons is described by

$$\left(\frac{\sigma}{E}\right)^2 = \left(\frac{\alpha}{\sqrt{E}}\right)^2 + \beta^2 \tag{2.2}$$

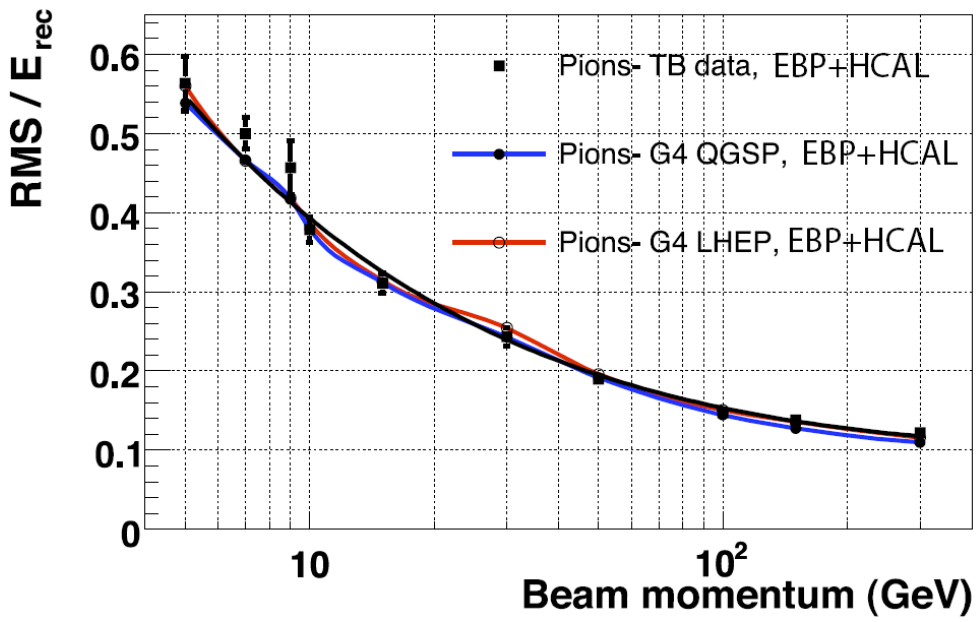

Figure 2.10: The ECAL+HCAL resolution for various pion energies obtained from testbeam [12]. The data were fitted with the resolution function of Equation 2.2 represented by the solid black line. The red and blue lines show the comparison to GEANT4 simulations with different parametrisations of the particle interactions.

Figure 2.10 shows the HCAL+ECAL resolution on charged pions as obtained by the 2004 test beam [12]. Fitting 2.2 to the data resulted in α =1.21 GeV$^{1/2}$ and β =0.095. A comparison of the data to GEANT4 simulations of the combined HCAL+ECAL system are also shown.

2.2.5 The Muon System

As muons are heavier than electrons and do not exhibit strong interactions, they can traverse through the calorimeter and magnet with minimal interaction with the detector. CMS employs three types of gaseous detectors to identify and measure muons as shown in Figure 2.11. The choice of detectors has been driven by the large surface to be covered and by the radiation environment. For $|\eta|$ <1.2 Drift Tubes (DT) interleaved with the iron return yoke are used. The point resolution is $\sim 200\,\mu$m and the directional resolution in ϕ is 1 mrad. In the endcap region, where background rates are larger and the magnetic field is inhomogeneous, Cathode Strip Chambers (CSC) are used with a coverage of $|\eta|$ <2.4. The point resolution of each

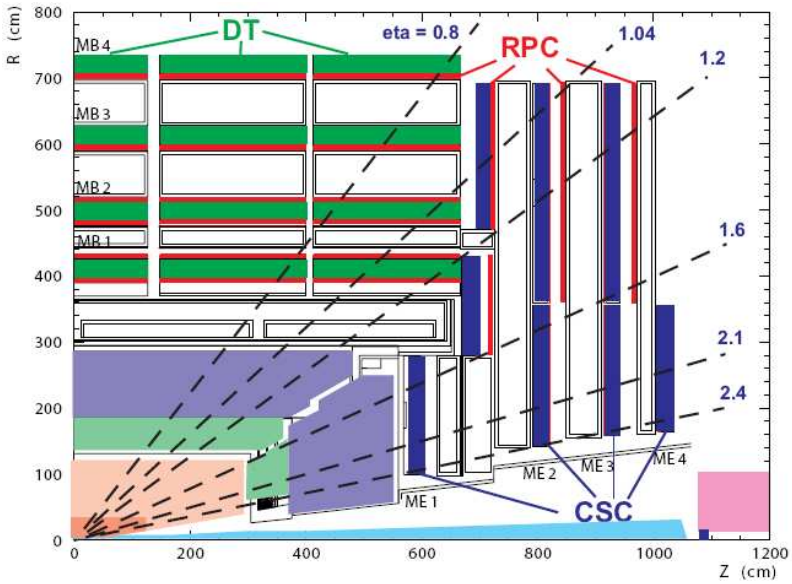

Figure 2.11: One quarter r-z view of the CMS Muon system.

chamber is 100-200 μm. Resistive Plate Chambers (RPC) are used throughout the detector up to $|\eta| < 2.1$ and operate in avalanche mode giving them a fast response (1 ns) ideal for bunch crossing identification, but have a coarser position resolution compared to the DTs and CSCs.

With this detection system, a centrally produced muon can be measured two times. In the tracker, and in the muon system. The measurement of the momentum using only the muon system is determined by the bending angle at the exit of the magnet and the interaction point. This measurement is called "stand-alone muon" and its resolution depends on the amount of multiple scattering of the muon within the detector before the first muon station for p_T^{μ} <200 GeV. After that point the chamber position resolution dominates. For low momentum muons the silicon tracker ("inner tracker")gives the best resolution. Figure 2.12 shows the resolution of the inner, stand-alone and combined (track+muon system) reconstruction as a function of the muon p_T.

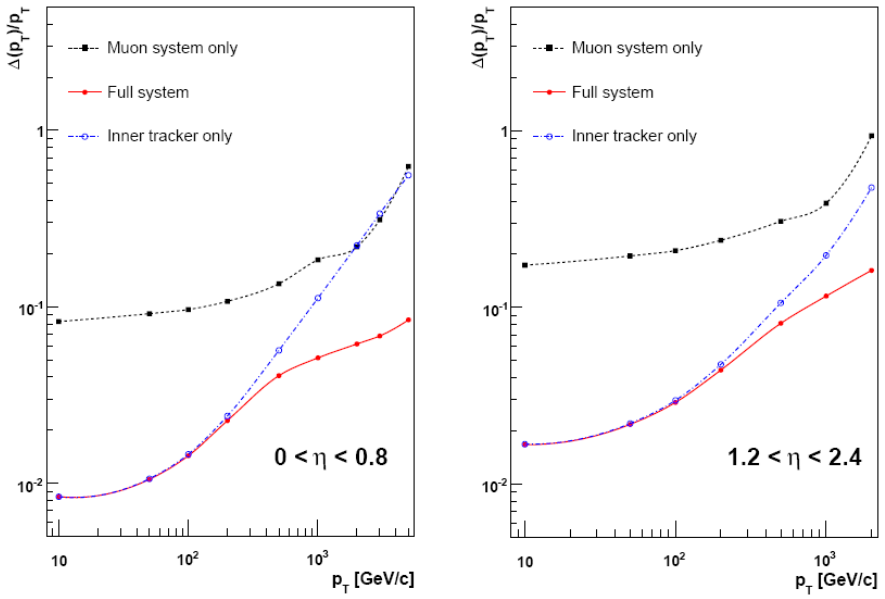

Figure 2.12: Resolution of the various muon recontruction methods as a function of the muon p_T.

2.2.6 The Trigger System

CMS has to be able to operate within the high crossing rate of LHC and detect very rare events with cross-sections much smaller than 1 nb out of all the inelastic proton-proton processes which have a cross-section of the order of 60 mb and are dominated by QCD processes. Figure 2.13 shows a wide range of processes together with their cross section resulting from proton-proton collisions as a function of the particle mass or jet E_T. The total inelastic cross-section coupled to the 25 ns crossing rate gives rise to an event rate close to 1 GHz at the nominal luminosity of $10^{34}\,\mathrm{cm}^{-2}\mathrm{s}^{-1}$. Furthermore considering the event size of the order of 1 MB gives rise to a total data stream rate produced by CMS O(1) PB/s which makes it impossible to store. Therefore an online selection strategy must be devised in order to reduce the large background rate while keeping the signal rate intact. This selection process is called the Trigger. The selection is done in two stages in CMS. At the first level (Level-1 or L1), the rate is reduced to 100 kHz using an on-detector processor. The available information at this stage is very coarse allowing only E_T, η, ϕ information available on jets and loosely identified muons and electrons. This information is then passed onto the next trigger level called the High Level Trigger (HLT) which uses a computer

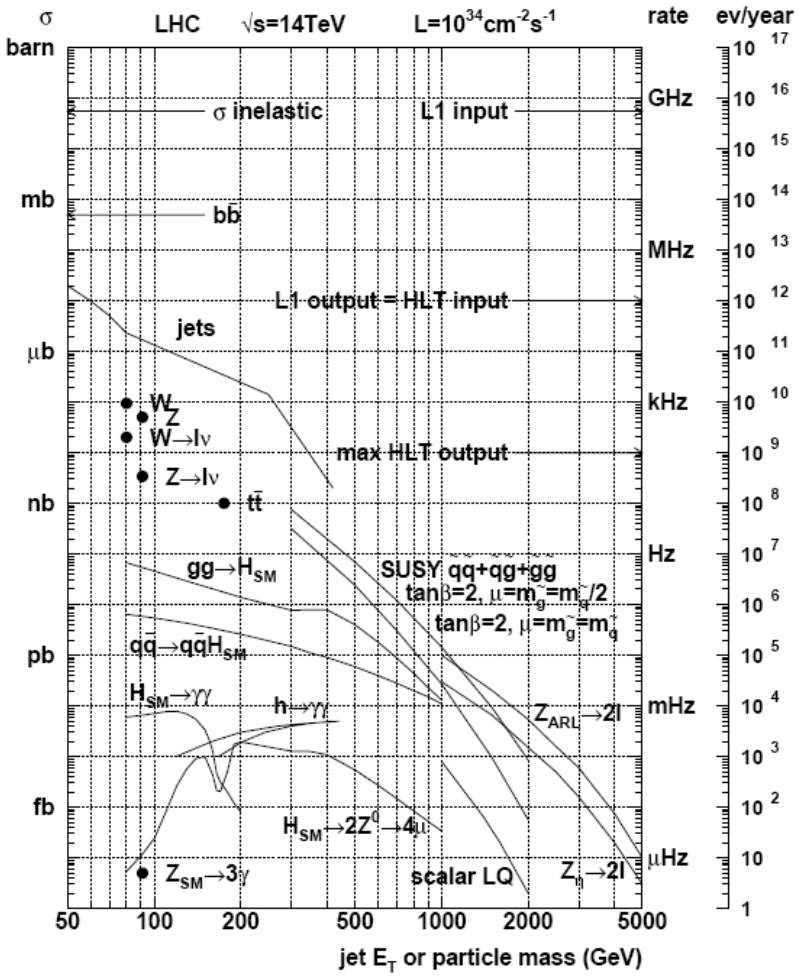

Figure 2.13: Inclusive proton-proton cross-sections for some physics processes at LHC. The interaction rates are given for the nominal luminosity and are shown on the right hand scale. Furthermore the L1 and HLT output/input rates are also denoted.

cluster to reduce the rate by a factor of 1000 by utilising more detector information such as tracks, vertices and calorimeter clusters.

The Level 1 Trigger

The Level 1 Trigger has to be able to operate at 40 MHz, synchronised to the LHC clock. For this purpose Field Programmable Gate Array (FPGA) technology is used which can handle the large data volume coming from the detector and can provide a trigger decision within 3.2 μs which corresponds to 128 bunch crossings. Using data from the ECAL, the HCAL and tracks from the Muon system, a primitive list of

objects is formed and comprises of the four highest in transverse energy isolated or non-isolated electromagnetic (e/γ) objects, central and forward jets, isolated hadrons (τ-jets) and muon tracks. For each object the available information is E_T or p_T, η, ϕ as well as $\Delta\eta$ and $\Delta\phi$ between objects. A logic called condition logic places a decision based on the above variables for each object. Each such decision forms a bit which can be combined with other decisions using an AND-OR logic. The Level-1 Global Trigger synchronises and processes all the information sent by the calorimeter and muon systems and makes a decision to keep or reject an event. There are 128 available bits available in the Global Trigger and hence as many possible Level 1 decision algorithms which also include the total (missing) energy which is a (vector) sum of the E_T of the calorimeter, as well as jet counters which count the number of Level-1 jets above a specific threshold.
The output of the Level-1 is a bit mask of algorithms and their boolean outcome as well as the list of Level-1 objects satisfying their individual criteria and thresholds. The task of the Level-1 Global Trigger is to collect these which are then forwarded to the High Level Trigger for further and more detailed processing.

The High Level Trigger

The role of the High Level Trigger is to reduce the rate to approximately 100 Hz and decide what events will be stored for offline analyses. This is done by making use of more detailed detector information and reconstruction algorithms. In contrast to the L1 which uses custom made hardware dedicated to analysing the detector information in a coarse grained way [1], at HLT the detector information is processed in a single processing farm containing 1000 CPU's also known as the Event Filter Farm. The data from ∼700 frontend electronics from all sub-detectors, is collected, sorted and stored in the RAM and used for the event reconstruction. The maximum per bunch-crossing processing time available for start-up is 40 ms and up to $\sim$ 1 s for high luminosity runs. The reconstruction and selection happens in two stages. At the first stage also known as L2, more refined objects are reconstructed, such as iterative cone jets and super-clusters around the region of the L1 accepted objects, and a first set of selection criteria are placed. At the second stage also known as L3,

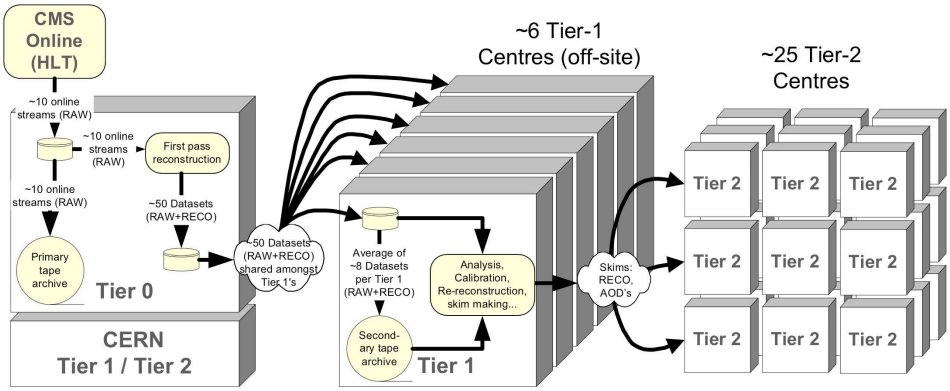

Figure 2.14: Schematic flow of event data in the CMS Computing Model [13].

tracks are unpacked and reconstructed in the region of the L2 objects. The choice of performing the tracking at L3 is due to the event rate reduction by this stage, which allows for the more time consuming tracker data unpacking and reconstruction. For algorithms that require information from the pixel detector, the pixel detector data is unpacked and pixel tracks are reconstructed at a stage between L2 and L3 also known as L2.5.

2.3 The CMS Computing Model in a nutshell

The computing requirements for LHC are unprecedented. By 2010 CMS alone will require over 60 PB of storage [9]. Therefore no single computing centre is capable of providing these level of resources. This motivated the creation of the LHC Computing Grid which groups resources of multiples centres to share the workload both in terms of storage and processing capabilities [49].

The CMS Computing Model makes use of the hierarchy of computing Tiers as proposed by the Models of Networked Analysis at Regional Centres (MONARC) project [50]. This model comprises of:

- A Tier-0 computing centre at CERN, which is directly connected to the experiment for the initial processing and data archiving. It is responsible for the

safe-keeping of the first copy of the RAW experimental data. Furthermore the first reconstruction of the data will be produced and stored there. Finally the Tier-0 will reprocess the data during LHC downtimes.

- Data from the Tier-0 will be distributed to 7 Tier-1 centres. Each Tier-1 is responsible for the safe-keeping of a share of the second copy of the RAW and the reconstructed data. Large amounts of reprocessed data will also be kept at there.

- Data from the Tier-1 will be transferred to $\sim$ 50 Tier-2 centres. These centres store the data for analysis by CMS physicists both local to the associated Tier-2 centre or remote users. Data at Tier-2 centres is not stored indefinitely, but is expected to be analysed and periodically replaced depending on the physics, detector or computing requirements.

Figure 2.14 shows a schematic of the CMS Computing Model [9].

Chapter 3

Electrons, τ-jets and the e+τ-jet High Level Trigger of CMS

3.1 Introduction

This chapter describes the selection and reconstruction of electrons and τ-jets both at offline and at trigger levels. A description of the offline algorithms for electrons and τ-jets respectively, is given before the corresponding trigger algorithm as the HLT reconstruction and selections form a sub-set of the offline reconstruction. A detailed description of the e+τ-jet HLT, its motivation and its performance are also discussed.

3.2 Aspects of electron reconstruction

The detection of electrons in CMS is characterised by a charged track in the Tracker and an electromagnetic energy deposition in the ECAL. The main aspect of the reconstruction is the recovery of the bremsstrahlung radiated energy from the electron as it traverses through the tracker as shown in Figure 3.1. As the CMS tracker material can reach $1.8\,\mathrm{X_0}$ at $|\eta|$ =1.5, about 35% of the electrons radiate more than 70% of their initial energy before reaching the ECAL and in about 10% of the cases, more than 95% of the initial energy is radiated [15]. The recovery of this energy is at the heart of the electron reconstruction algorithms both at HLT and offline.

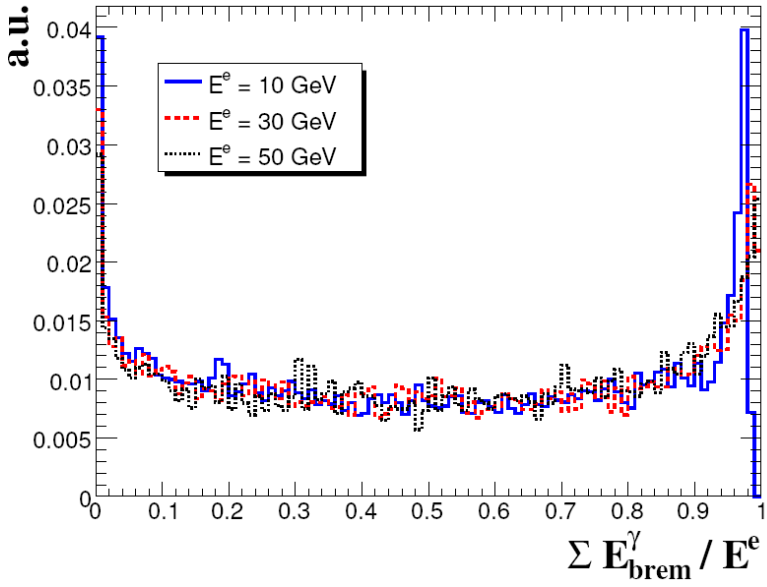

Figure 3.1: Distribution of the fraction of the generated electron energy (E^e) radiated as bremsstrahlung photons (ΣE^{γ}_{brem}) up to a radius corresponding to the ECAL inner surface [14].

3.2.1 Reconstruction of offline electrons

Electron reconstruction begins by clustering the ECAL energy of the electron. The radiated energy is spread in ϕ due to the electron trajectory in the magnetic field and three algorithms have been developed to account for this effect. The Hybrid algorithm which clusters the energy in the ECAL barrel and the Multi5x5 or Island algorithms which cluster the energy in the ECAL end-caps.

The Hybrid algorithm

The Hybrid clustering algorithm, used in the barrel for offline and HLT electron reconstruction, takes advantage of the shower shape knowledge in η and dynamically searches for energetic cells in ϕ. It begins by finding the most energetic crystal with E_T >1 GeV which is then used as a seed to form blocks (dominos) of 1x3 or 1x5 crystals in η (depending on the seed energy) around it, as shown in Figure 3.2. Blocks with energy less that 0.1 GeV are discarded. This clustering algorithm therefore creates clusters of well defined shape in η but separated in ϕ, and thus collecting

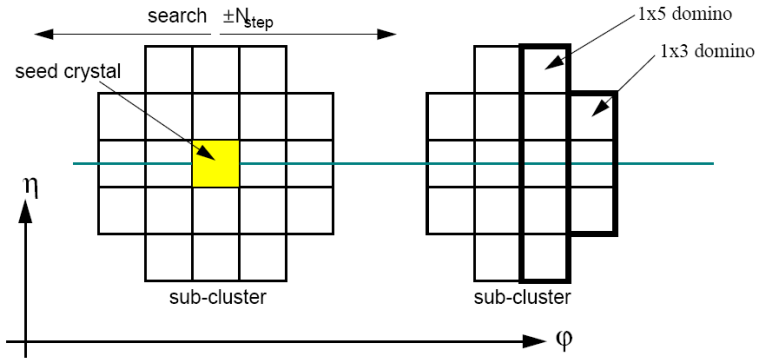

Figure 3.2: The Hybrid clustering algorithm [15] as described in the text.

the bremsstrahlung radiation. Finally super-clusters are formed by collecting the energy of all the clusters within 17 crystals from the seed crystal in ϕ [15].

The Multi5x5 algorithm

The Multi5x5 algorithm is applied in the ECAL end-caps for offline electron reconstruction. As in the Hybrid algorithm, it begins by finding the most energetic crystal E_T >0.18 GeV which is then used to seed the clustering process. An E_T comparison is carried out between this seed crystal and its four adjacent neighbours. If the seed crystal is a local maximum then a 5x5 matrix of crystals is constructed around the seed only including crystals that do not belong to another cluster. However the sixteen crystals surrounding the seed crystal can be used to seed other clusters provided that they form a local maximum with E_T >0.18 GeV when compared to their four adjacent neighbours. Figure 3.3 demonstrates this process. Finally a rectangular $\eta - \phi$ window is centered around each seed and the cluster energy deposits within 0.14 in η and 0.6 rad in ϕ from the seed are summed up to build the super-cluster. This is performed for all seeds in descending order in energy and deposits are only associated to one super-cluster [16].

The Island algorithm

The Island algorithm is applied in the ECAL end-caps for HLT electron reconstruction. It begins by finding the highest E_T crystal with E_T >0.18 GeV which acts as

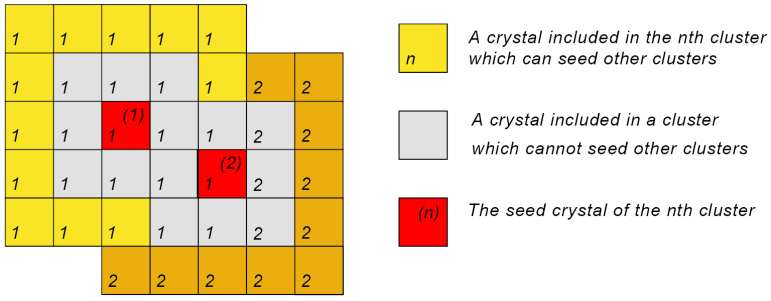

Figure 3.3: The Multi5x5 clustering algorithm [16] as described in the text.

a seed. Starting from this seed the algorithm moves in both directions in ϕ and collects all crystals until a rise or a gap in energy is found. The algorithm then moves one crystal in η and the ϕ search is repeated forming clusters as shown in Figure 3.4. The steps in η continue until a rise or a gap in energy is found. This η search is done for both directions around the seed crystal. Note that all the crystals collected, are marked as belonging to the specific cluster and cannot be reused. Also each seed can only be used to seed one cluster. This ensures that no energy double counting occurs. The main points of this clustering algorithm are that it will not split up the energy of an electron and a radiated soft photon if the showers are close enough. However it will split the showers of two photons coming from a decay of a π^0 (if the opening angle is large enough). Energy deposited in crystals below the seed threshold will not be clustered and neither will small deposits of energy coming from noisy crystals or low energy particles originating from pile-up events. Super-clusters are then formed by summing Island clusters within a rectangular $\eta - \phi$ window separated by 0.06 in η and 0.6 rad in ϕ from the highest E_T Island cluster. The formation of such super-clusters reduces considerably the tails in the reconstructed energy distribution of electrons as shown in Figure 3.4 [15].

Electron Track Reconstruction

The energy weighted average position of these electron super-clusters is then used to propagate back to the pixel layers according to the magnetic field using the beam spot as the reference point, for both positive and negative charge hypotheses. The

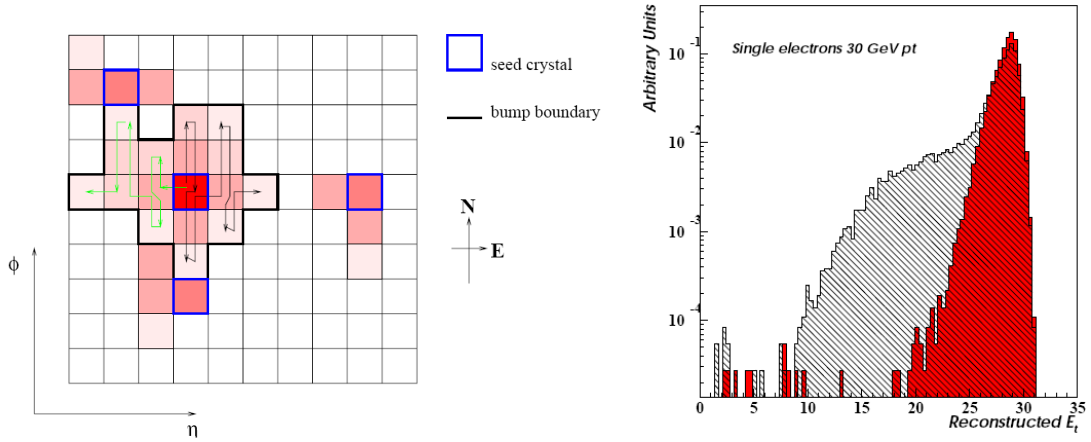

Figure 3.4: Left: The Island clustering algorithm [15] as described in the text. Right: Reconstructed transverse energy for 30 GeV p_T electrons using a single island cluster (hatched) and a super-cluster collected in a 1-crystal-wide window in η around it (solid filled) [15].

advantage of this technique is that the energy weighted average position of the super-cluster coincides with the impact point of an electron of the same momentum in the calorimeter, had it not radiated energy. Compatible pixel hits with the super-cluster position in z and ϕ are then searched for in at least two out of the three pixel layers. If the first compatible hit is found, the transverse momentum of the candidate electron (calculated from the energy of the super-cluster and the beam spot position) and the magnetic field map are used to form an estimated trajectory through the tracker using two scenarios for opposite charges. The second compatible hit is searched for within a tighter z and ϕ window. In the pixel end-caps if a second pixel hit is not found, a second compatible hit is searched for in the first silicon strip layer. The pixel matching criteria are described in Table 3.1.
Using these pixel seeds, Gaussian Sum Filtered (GSF) tracks are formed which account for the non-gaussian fluctuations induced by bremsstrahlung emission [14].

Electron Isolation and Identification

In order to reduce contamination from QCD jets, isolation and identification criteria are applied once the basic electron object is reconstructed. A typical form of isolation in the tracker is to place a cut on the sum the momenta of tracks within an annulus in (η-ϕ) space around the electron direction at the vertex. Isolation in the

ECAL is slightly more involved as the electron "footprint" due to bremsstrahlung radiation must be removed from the energy sum of ECAL crystals. This is done by subtracting the ECAL crystal energy in a strip in ϕ of width $\delta\eta$, as well as the energy of ECAL crystals within a cone ΔR_s in η-ϕ space around the super-cluster position, from the total energy sum of ECAL crystals within the isolation cone in η-ϕ space. This method of ECAL isolation is called the "Jurassic Isolation" [51]. Further identification criteria to reduce contamination from pions can also be applied. These criteria include a cut on H/E which denotes the HCAL E_T behind the electromagnetic seed cluster over the E_T of the electromagnetic seed cluster, $\Delta\phi_{in}$ and $\Delta\eta_{in}$ which denote the difference between the super-cluster position and the track inner most position in ϕ and η propagated to the ECAL, $\sigma_{\eta\eta}$ which describes the energy weighted average of the electron shower spread in η, E/P which denotes the ratio of the energy of the electron super-cluster divided my the track momentum, $E2\times5/E5\times5$ which denotes the maximum in energy 2×5 ECAL crystal strip in η out of the 5×5 ECAL crystals centered around the electron seed crystal divided by the energy in the 5×5 crystal matrix and $E1\times5/E5\times5$ which denotes the energy of the central 1×5 ECAL crystal strip in η divided by the energy in the 5×5 crystal matrix.

3.2.2 Selection and reconstruction of electrons at the Trigger

L1 e/γ object trigger

At L1 no distinction is made between electrons and photons (γ) due to the lack of tracking information. Instead, an electromagnetic trigger requiring lateral shower containment in the ECAL and limited HCAL activity is applied for the central region of the detector ($|\eta|$ <2.5). The e/γ trigger uses a 3x3 trigger tower window which it slides across η and ϕ. The algorithm begins with a 3x3 window centered over an ECAL trigger tower with a significant energy deposition. The surrounding eight towers including the HCAL towers behind them are used for the evaluation of the lateral shower shape and isolation as shown in Figure 3.5. A Fine Grain

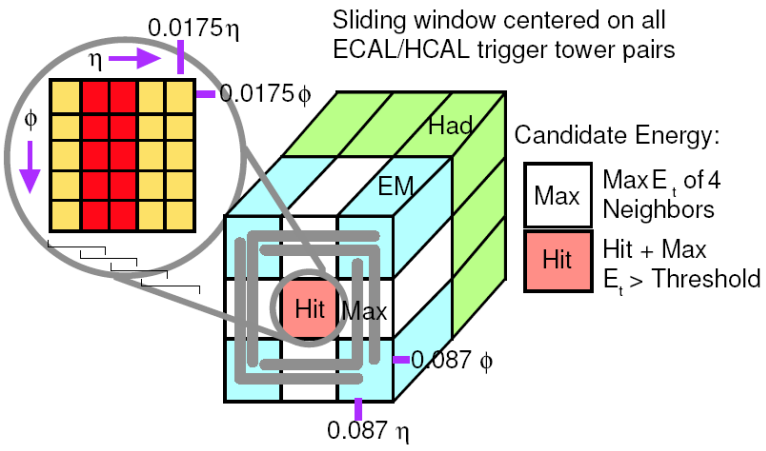

Figure 3.5: The L1 e/γ object made up of 3x3 trigger towers. The E_T of the object is defined as the sum of the E_T of the central - "Hit" region and the highest in E_T adjacent neighbour - "Max". The Isolation and Fine Grain veto logic is also displayed.

(FG) veto is fired if the highest in energy 2x5 (η-ϕ) crystal strip out of the 5x5 crystals contained in the ECAL trigger tower contains <90% of the energy of the tower. Hence the L1 e/γ object is flagged as non electromagnetic. Furthermore a longitudinal shower shape veto (H/E) is fired if the fraction of energy in the HCAL tower behind the ECAL trigger tower (H) over the energy of ECAL trigger tower of the 3x3 region (E) is above a programmable threshold such as 5%. Finally the isolation veto (IV) is fired if none of the "L" strips of Figure 3.5 have an E_T below a programable threshold such as 1.5 GeV. The E_T of the L1 e/γ object is evaluated by summing the E_T of the central ECAL trigger tower and its highest in E_T adjacent neighbor. Both isolated and non-isolated L1 e/γ objects are available to trigger on. For the isolated case none of the nine trigger towers of the 3x3 region should fire the FG, H/E vetoes and the IV should also not fire. For the non-isolated case the central trigger tower out of the 3x3 is required not to fire the FG and H/E vetoes but no IV is applied. For both cases an E_T threshold on the sum of the is applied on the central ECAL trigger tower and its highest in E_T adjacent neighbour.

High Level electron trigger

The electron HLT begins when the required L1 e/γ condition is fulfilled. A sequence of filters is then applied with increasing complexity and hence CPU requirements.

Pixel Windows	$\Delta\phi_1$ (mrad)	$\Delta\phi_2$ (mrad)	Δz_2 (cm)
Ideal	40 ([-25,+15])	±1	±0.05
Start-up	60 ([-35,+25])	±5	±0.05
Large	75 ([-45,30])	±10	±0.2
Offline	200 ([-125,75])	±2	±0.07

Table 3.1: Table summarising the pixel matching parameters for a negative charge hypothesis for the three regimes discussed in the text as well as the much looser pixel matching requirements on offline "GSF" electrons. $\Delta\phi_1$ represents the window range in the inner most layer. If no compatible hit is found in the 1st layer, the 2nd layer is considered. $\Delta\phi_2$ and Δz_2 represent the window sizes in ϕ and z for the second to innermost layers.

Firstly ECAL super-clusters are built using the Hybrid or Island clustering algorithms (as discussed in Section 3.2.1) which collect the energy spread in ϕ as the electron traverses through the tracker material within the magnetic field of CMS. These super-clusters are then required to match the desired L1 e/γ seeds in (η-ϕ). After this matching step an E_T requirement is placed on the super-clusters followed by HCAL isolation.

Pixel hit matching to the super-cluster then follows as described in Section 3.2.1 As the performance of these pixel matching cuts are sensitive to the misalignment of the detector and the beam spot uncertainty, as well as the standard window cuts tuned for ideal detector and beam spot conditions, two separate sets of selections have been devised. Large matching Windows (LW) for the very beginning of data taking and Startup matching Windows (SW) for the early stages of data taking when the detector is not perfectly aligned. Table 3.1 summarises these values.

These pixel hits are used to seed the track reconstruction. Due to timing constraints at HLT, dedicated GSF tracking cannot be performed and standard Kalman tracks are used instead. A cut is placed on the relation between the measured E_T in the super-cluster and the measured p_T of the track in order to reduce QCD rate.

Regional track reconstruction then follows by seeding tracks with pairs of hits in the pixel layers located within a rectangular η-ϕ region around the reconstructed electron. Using these tracks and the reconstructed electron track, a Track isolation is placed on the electron. A nominal set of all the selection variables above are summarised in Table 3.5 [1].

3.3 Aspects of τ-jet reconstruction

Hadronic tau decay jets (τ-jets) resemble QCD jets from a calorimetric perspective, with electromagnetic and hadronic energy deposits originating from the neutral and charged pions, respectively. However τ-jets are more collimated and isolated than QCD jets. The main challenge of the τ-jet reconstruction algorithms is therefore to reduce this enormous QCD background. Another complication arises from the fact that a significant fraction of the τ-lepton momentum escapes undetected with the ν_τ, which renders τ-jets even softer and further reduces the experimental discrimination of signals involving τs specially when compared to those with electrons and muons [2].

3.3.1 Reconstruction of offline τ-jets

There are two approaches for τ-jet object reconstruction in CMS. One based on Particle Flow (PFlow or PF) and the other on Calorimetric Towers (Calo-Towers). Both approaches build "iterative-cone" jets [9] of size ΔR =0.5 out of Particle Flow objects or calorimetric towers respectively. This analysis focuses on the use of PF τ-jets (PFTaus) due to their improved energy and position resolution as described later in this Section.

The Particle Flow Algorithm

Particle Flow reconstruction aims to provide a complete event description at the level of reconstructed particles by combining information from all the sub-detectors of CMS. The PFlow algorithm begins by firstly identifying PF muons and electrons using dedicated algorithms [17] and removing their tracks and associated calorimetric depositions. PF charged hadrons are then reconstructed by linking the remaining tracks to calorimetric clusters by extrapolating tracks from the last measured hit to the HCAL surface at a depth corresponding to one interaction length. The track is linked to any given cluster if the extrapolated position in the HCAL is within the boundaries of one of the cells of the cluster, appropriately enlarged to account

for the presence of gaps between calorimeter cells, cracks between calorimeter modules, for the uncertainty on the position of the shower maximum, and for the effect of multiple scattering for low-momentum charged particles. The link distance is defined as the distance in the (η,ϕ) plane between the extrapolated track position and the cluster position. If the calibrated ECAL and HCAL energy is compatible with the track momentum within measurement uncertainties, the charged hadron momentum is then redefined by fitting to the measurements of the tracker and the calorimeter. The benefit of this approach is mainly at high energies or high η regions where the track parameters are determined with degraded resolutions. In the case that the energy of the cluster linked to the track exceeds the track momentum by more than the calorimeter resolution defined as $102\%/\sqrt{(}\mathrm{p}) \oplus 6.5\%$ in the barrel or $135\%/\sqrt{(}\mathrm{p}) \oplus 1.8\%$ a Particle Flow photon (PFGamma) or Particle Flow neutral (PFNeutral) is built. If the excess is greater than the total ECAL energy associated to the track then a PFGamma is created with the total ECAL energy calibrated with a photon hypothesis and the rest of the energy is associated to a PFNeutral. If the excess is smaller then only a PFGamma is created.
The remaining ECAL and HCAL clusters which were not linked to to any track give rise to PFGamma's and PFNeutrals whose energy is obtained by calibrating the cluster energies under the photon or hadron hypothesis respectively.
As the hadronic content of a τ-jet mostly involves charged pions kaons and neutral pions decaying to photons, the PFLow algorithm is ideally suited to delivering an accurate reconstruction of the τ-jet as the HCAL energy deposition is correctly replaced by the accurate track momenta. Figure 3.6 shows the $\mathrm{E_T}$ and ϕ resolutions for τ-jets originating from τ^- leptons with $\mathrm{E_T}$ >50 GeV/c, for both Calorimetric and Particle Flow approaches [17]. The improvement provided by PFlow is clearly evident.

The τ-jet identification algorithm

The τ-jet identification proceeds in two stages for both calorimetric and PFlow τ-jets. Firstly a common set of selections appropriate for various analyses involving τ-jets which employ relatively simple and robust methods such as Tracker and ECAL

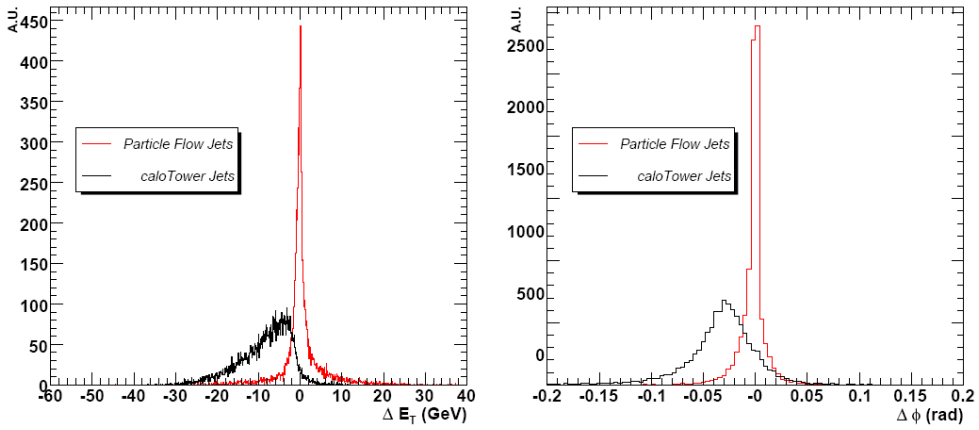

Figure 3.6: E_T (left) and ϕ (right) resolutions for τ-jets originating from τ^- leptons with E_T >50 GeV/c, for both Calorimetric and Particle Flow approaches. The bias in ϕ is due to the 4 T magnetic field of CMS [17].

isolation, similar to those used for trigger conditions, and are aimed at strongly suppressing backgrounds while still preserving a large fraction of the genuine τ-jets. The selections begin by applying an E_T threshold is applied to each PFlow (Calo) jet. Next at least one PFlow charged hadron (track) with p_T^{ldg} >5 GeV/c is required to be found at a distance ΔR_m <0.1 from the jet direction in (η, ϕ) space. The highest-momentum PFlow charged hadron (track) satisfying this cut is called the "leading track" or "leading PF charged hadron". An inner narrow "signal cone" (ΔR_s), expected to contain all tau decay products, is then defined around the direction of the leading track. An isolation annulus, expected to contain little activity if the tau is isolated is defined in (η-ϕ) within $\Delta R_s < \Delta R < \Delta R_{iso}$ as shown in Figure 3.7. A typical size of $\Delta R_{iso} = 0.5$ is used by default.

The cone particle contents are determined with a direction w.r.t. the primary vertex position and are thus unaffected by sweeping effects from the strong magnetic field. The isolation criteria require no reconstructed PFlow charged hadrons (tracks) with p_T >1 GeV/c and no PFGammas with p_T >1.5 GeV/c allowed in the isolation annulus. It is worth noting that the size of the signal cone ΔR_s can either be fixed or varying with E_T. The reason for this is that the products of a three or five prong τ-jet decay become more collimated as the τ-lepton E_T increases due to the larger Lorenz boost. Therefore a varying signal cone size ensures the signal cone contains all the τ-jet decay products for low E_T jets, while still suppressing QCD

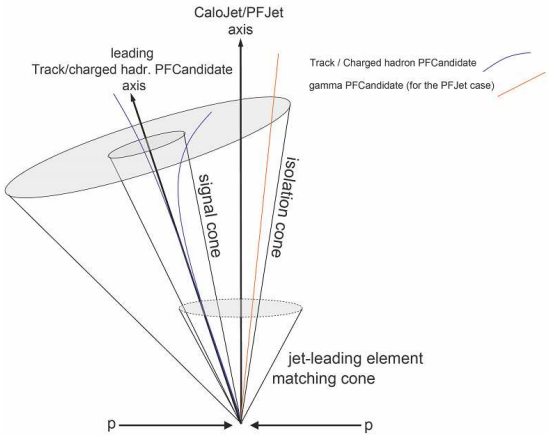

Figure 3.7: The τ-jet cone isolation algorithm [2].

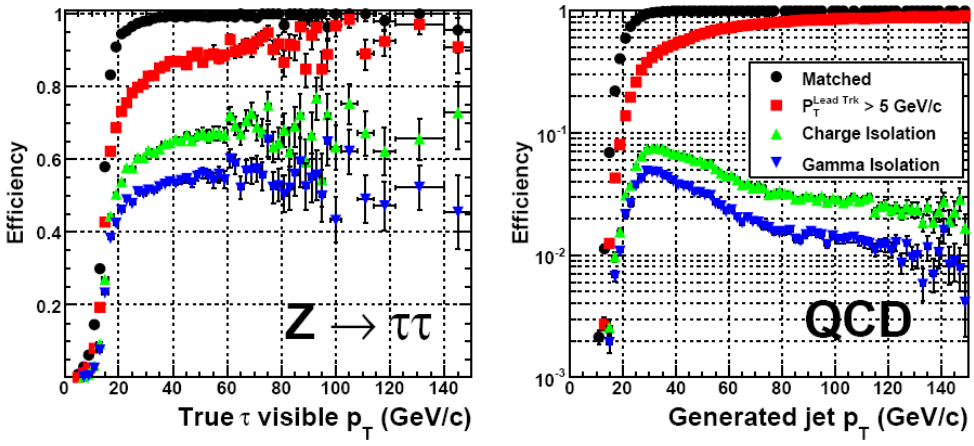

Figure 3.8: The τ-jet reconstruction and selection efficiency as a function of the PFlow τ-jet E_T for τ-jets from $Z \rightarrow \tau\tau$ decays (Left) or generator jets from QCD di-jet events (Right). The signal cone size varies as $\Delta R_s < 5/E_T$ between 0.07 and 0.15 [2]. Efficiencies are cumulative.

background. The efficiency of the τ-jet selection criteria, as a function of PFTau E_T and η, including the object reconstruction efficiency (matching efficiency) for true τ-jets from Z$\rightarrow \tau\tau$ decays or generator jets from QCD di-jet events are shown in Figures 3.8 and 3.9 respectively. The signal cone size varies as $\Delta R_s < 5/E_T$ between 0.07 and 0.15 [2].

The second stage of τ-jet selection, involves applying more specific selections to remove electrons or muons faking τ-jets. This is important as electroweak processes such as Z$\rightarrow ee/\mu\mu$ produce copious amounts of isolated electrons and muons which can satisfy the isolation criteria of the PFTau. In order to reject electrons two

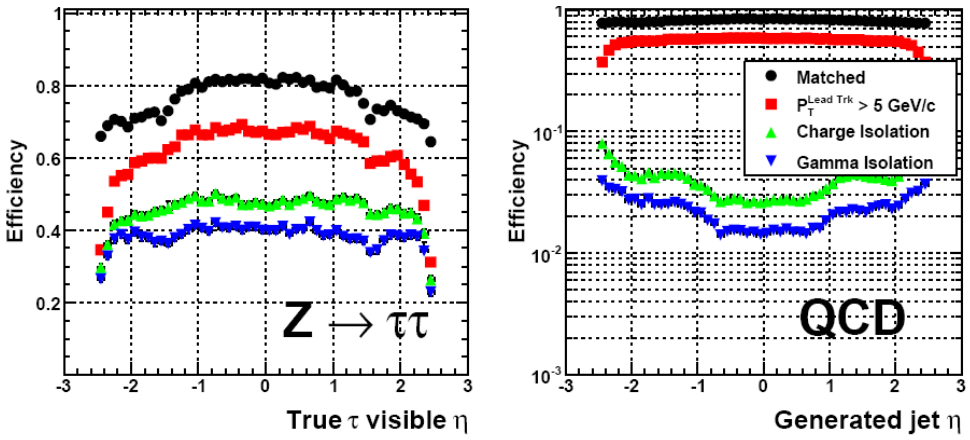

Figure 3.9: The τ-jet reconstruction and selection efficiency as a function of the PFlow τ-jet η for τ-jets from $Z \rightarrow \tau\tau$ decays (Left) or generator jets from QCD di-jet events (Right). A cut on $E_T > 15\,GeV$ is applied.The signal cone size varies as $\Delta R_s < 5/E_T$ [2]. Efficiencies are cumulative.

approaches have been used. Firstly as electrons deposit a larger amount of their energy in the ECAL and less in the HCAL compared to the τ-jet, calorimetric variables such as the electro-magnetic fraction or the maximum in E_T HCAL tower of the PFTau divided by the PFTau leading PF charged hadron p_T are used. The second approach aims at zooming inside the tau candidate and trying to reconstruct an electron, switching the focus to finding all electrons specially those which fail the reconstruction procedures of Section 3.2 (e.g due to radiating large fraction of their energy in the tracker). This is achieved by using an electron pre-identification (electron pre-id) which uses multivariate techniques taking as input the track quality, the difference between the momentum measured at the beginning and at the end of the track and the compatibility between the latter and the linked ECAL cluster, achieving a 90-95% efficiency for electrons across the entire tracker acceptance, with about 5% pion contamination. A detailed view of the performance of these two approaches is described in Section 5.4.3. To reject muons faking PFTaus, the very high efficiency of standard muon reconstruction and identification in CMS provides nearly optimal rejection of muons otherwise identified as tau candidates. A PFTau candidate can then be rejected if it matches any identified muon. This gives a PFTau efficiency of $> 99\%$ with a muon efficiency of $< 1\%$ [2].

A final requirement can be applied to further discriminate between QCD jets and PFTaus, by placing a cut on the number of PF charged hadrons within ΔR_s as

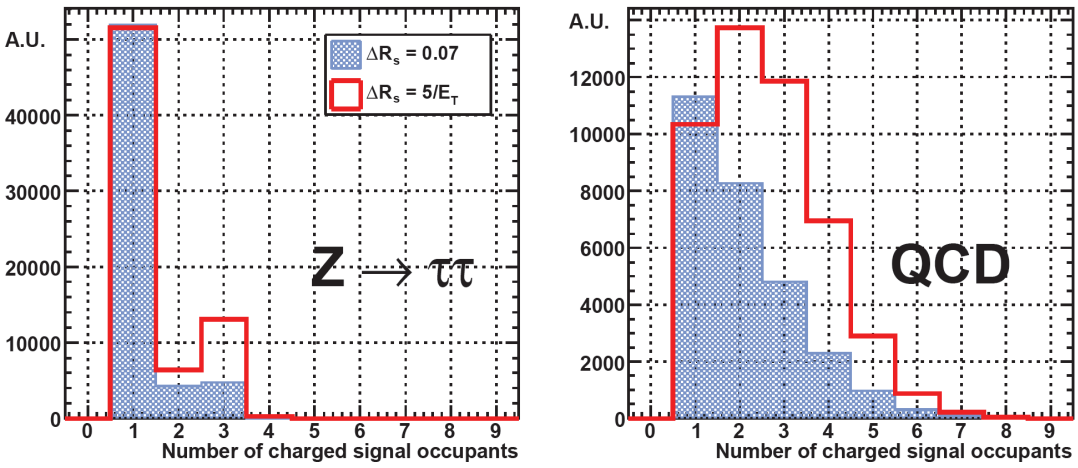

Figure 3.10: Comparison of the distributions of the charged-hadron multiplicity in the signal cone, for τ-jets (left) and QCD jets (right), with the shrinking ($\Delta R_s < 5/E_T$) and fixed ($\Delta R_s = 0.07$) signal-cone definitions. PFTaus having $E_T > 10\,GeV$ are isolated within $\Delta R_{iso} = 0.5$ with $p_T^{chg\,had} > 1\,GeV/c$, $p_T^{\gamma} > 1.5\,GeV/c$.

shown in Figure 3.10, for two different signal cone types fixed at 0.07 (filled) and varying as $5.0/E_T$ (solid line), for hadronically decaying τ's in $Z \rightarrow \tau\tau$ events (left) and QCD jets (right). Due to the τ-jet structure a cut on 1 or 3 signal charged hadrons can be placed.

3.3.2 Selection and reconstruction of τ-jets at the Trigger

L1 τ-jet object trigger

At L1 hadronic jets are reconstructed using a sliding window of 3x3 "calorimetric regions" each of which contains either 4x4 ECAL+HCAL towers as shown in 3.11 or a single tower in the forward regions where the tower size is larger. The central calorimetric region E_T is required to be higher than the eight surrounding neighbours. There are two criteria for determining whether a L1 Jet is a τ-jet and they are based on the fact that τ-jets are narrower and more isolated than QCD jets. The "Activity" criterion requires the ECAL and HCAL towers of the nine regions making up the L1 Jet that are above programable thresholds, (E_T^{ECAL}, E_T^{HCAL}) should satisfy one of the patterns of Figure 3.11 (τ-veto off) [52]. The "Isolation" criterion, which has not been yet implemented in the L1 hardware or the L1 hardware emulator,

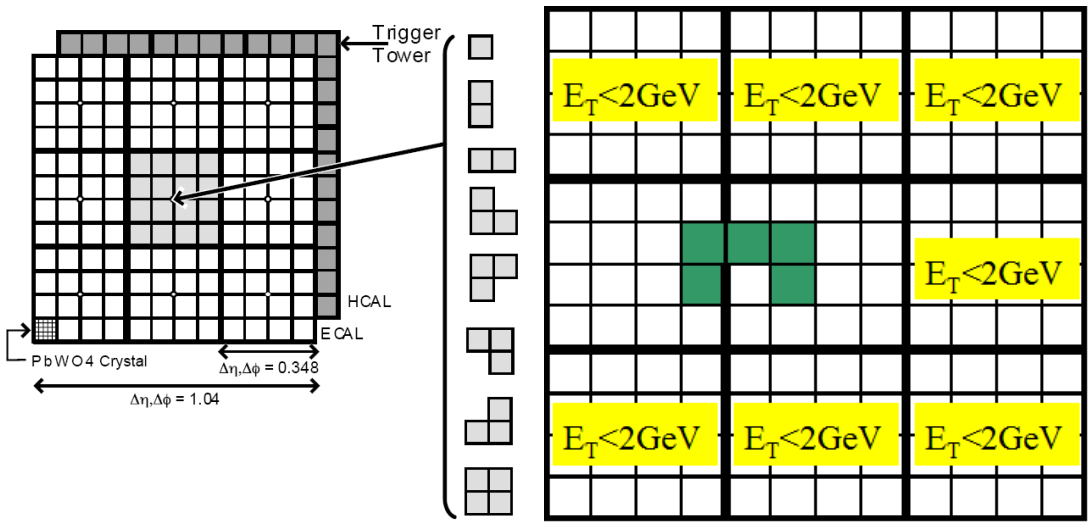

Figure 3.11: The L1 τ-jet object Activity (Left) and Isolation (Right) criteria as described in the text. In the current version of the hardware and hardware emulator only the Activity criterion is placed, which requires all nine regions to have an activity pattern matching one of the veto patterns shown.

requires only one region, excluding the central one, to have an energy above a programable threshold (E_T^{Iso}) as shown in Figure 3.11. The values of (E_T^{ECAL}, E_T^{HCAL}) and E_T^{Iso} will vary depending on the instantaneous luminosity. A nominal set of values for the $10^{32}\,cm^{-2}s^{-1}$ regime are (E_T^{ECAL}=4, E_T^{HCAL} = 4) GeV, E_T^{Iso} = 2 GeV. Once the Isolation criterion is implemented in the hardware a logical AND between the "Activity" and "Isolation" criteria will define a L1 τ-jet. An E_T cut is also applied on the L1 τ-jet which is evaluated by summing the E_T of all nine calorimetric regions and applying a set of L1 Jet corrections which are tuned for QCD jets thus over-correcting the L1 τ-jet response as shown in Figure 3.12.

HLT τ-jet object trigger

The τ-jet HLT begins once the appropriate L1 τ-jet bit has fired. At L2 iterative cone calorimetric jets of cone size 0.5 are built around the four L1 τ-jet candidates and an E_T threshold is placed on these. An ECAL isolation is applied in order to further reduce the QCD rate before the more CPU consuming tracking is performed. As there is no tracking information, the isolation is not performed around the leading track as described in Section 3.3.1 but around the L2 calorimetric jet axis and the

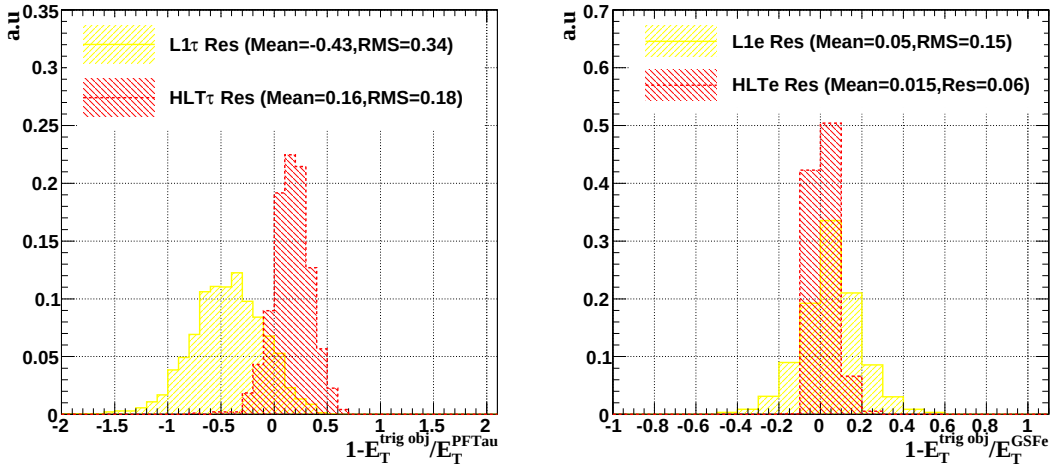

Figure 3.12: Resolution of τ trigger objects (Left) and electron trigger objects (right). These have been measured against offline PFTaus and GSF electrons satisfying the pre-selection criteria of Table 3.2 for $E_T^{PFTau} > 15\,GeV$ and $E_T^{GSFe} > 10\,GeV$ respectively. A clear overcorrection of the L1 τ-jet E_T scale is seen by an average factor of 1.43.

sum of crystal E_T within an annulus around the calorimetric jet axis is required to be smaller than a programmable value ($< 3\,GeV$). At L2.5, all pixel tracks containing pixel hits on all three pixel layers or silicon strip tracks within ($\Delta\eta$,$\Delta\phi$)=(0.1,0.1) around the L2 τ-jet axis are reconstructed [1]. Using these pixel (silicon-strip) tracks, a pixel (silicon-strip) track isolation is applied as described in Section 3.3.1. The motivation for performing pixel track based isolation is that it saves processing time compared to the CPU demanding silicon strip tracking. Unpacking seeding and building silicon strips tracks within a region in ($\Delta\eta$,$\Delta\phi$)=(0.5,0.5) around the L2 τ-jet axis requires ~ 3 more CPU time compared to unpacking the whole pixel detector and building pixel tracks [53] and provides no improvement in reducing the QCD rate compared to the pixel track isolation. Finally an optional L3 can be applied where full silicon strip tracks are reconstructed in order to place a tighter p_T cut on the leading track associated to the L2.5 τ-jet. This additional level will become more important during the $2\times10^{33}\,cm^{-2}s^{-1}$ instantaneous luminosity regime when trigger rates will need to be further reduced.

3.4 The e+τ-jet trigger

The motivation behind a combined e+τ-jet trigger (e+τ) using a logical AND, is mainly in order to lower the E_T threshold of the electron trigger while keeping the rate due to QCD low by requiring the existence of a τ-jet object as well. As τ decays to leptons (electrons, muons) are three body decays, the E_T spectrum of the outcoming lepton tends to be soft (majority have E_T <30 GeV). Therefore by having a lower electron E_T threshold compared to the single electron trigger, one can gain in the number of signal events (H(Z)$\rightarrow \tau\tau \rightarrow e + \tau$-jet) stored on tape.

3.4.1 Trigger Performance

Sample definitions

Trigger rates for the e+τ-jet trigger were measured using a PYTHIA sample of QCD events with $\hat{p}_T$ >15 GeV/c where $\hat{p}_T$ is the transverse momentum scale of the process. Trigger efficiencies were measured on a PYTHIA sample of Z$\rightarrow \tau\tau \rightarrow e+\tau$-jet events where the generated electron and τ-jet were required to lie within the tracker acceptance with $|\eta|$ <2.5. In light of the LHC schedule $\sqrt{s} = 10$ TeV was used for both signal and QCD samples, where $\sqrt{s}$ denotes the center of mass energy. CMS SoftWare version (CMSSW) CMSSW_2_1_7 was used for running the trigger and offline reconstruction. Further pre-selections were then applied only to the Z$\rightarrow \tau\tau \rightarrow e + \tau$-jet sample on offline objects summarised in Table 3.2. The total efficiency of these pre-selections are summarised in Table 3.4

All the trigger thresholds and selections were optimised for the $10^{32}\,\mathrm{cm}^{-2}\mathrm{s}^{-1}$ instantaneous luminosity regime. These selections are summarised in Tables 3.5 and 3.6 for the electron and τ-jet branches of the e+τ trigger respectively.

Trigger Rate

The performance of the e+τ-jet trigger (HLT_IsoEle12_IsoTau_Trk3), where the E_T threshold of the electron branch has been lowered to 12 GeV compared to the 15 GeV

- Offline electron and PFTau with $E_T > 14\,GeV$ and $E_T > 15\,GeV$ respectively.
- Offline electron isolated in the tracker with no tracks of p_T^{trk} >1.5 GeV/c within an annulus of 0.02< ΔR <0.5.
- Offline electron satisfies "Robust" identification criteria of Table 3.3 which are tailored to select electrons with high (>90%) efficiency during the initial stages of data taking.
- Offline PFTau with leading track p_T >5 GeV/c.
- Offline PFTau isolated in the tracker with no tracks of p_T^{trk} >1.0 GeV/c with DR_{iso} <0.5, and DR_s <5.0/E_T and bounded between 0.07<DR_s <0.15.
- Offline electron and PFTau satisfying the above criteria satisfy $DR_{e\tau}$ >0.7 (ensure separate objects).

Table 3.2: Offline object event pre-selections applied on Z$\rightarrow \tau\tau \rightarrow e + \tau$-jet events.

"Robust" cut Based Criteria	H/E	$\Delta\phi_{in}$ [rad]	$\Delta\eta_{in}$	$\sigma_{\eta\eta}$
EB (η_e <1.479)	0.115	0.090	0.0090	0.0140
EE (η_e >1.479)	0.150	0.092	0.0105	0.0275

Table 3.3: Table summarising the Robust electron identification criteria. H/E denotes the HCAL E_T behind the electromagnetic seed cluster over the E_T of the electromagnetic seed cluster. $\Delta\phi_{in}$ and $\Delta\eta_{in}$ denote the difference between the super-cluster position and the track inner most position in ϕ and η respectively, $\sigma_{\eta\eta}$ describes the energy weighted average of the electron shower spread in η.

Pre-selection	Efficiency
Generator Level	0.484±0.003
Offline Level	0.164±0.004
Total	0.079

Table 3.4: Table summarising the generator and offline level Z$\rightarrow \tau\tau$ event pre-selections. Efficiencies are relative to the previous.

HLT e of e+τ-jet Cut	Value
L1 seed	L1 Iso e/γ E_T >10 AND L1 τ-jet E_T >20 GeV
HLT E_T	E_T >12 GeV
HCAL Iso	ΣE_T^{HCAL} <3 GeV within ΔR <0.3 OR H/E<0.05
Pixel Match	Ideal matching windows
Loose 1/E-1/P	(1/E-1/P)>999. GeV^{-1}
Track Iso	$\Sigma p_T^{trk}/p_T^e$ <0.06 within 0.02< ΔR <0.2, p_T^{trk} >1 GeV

Table 3.5: Table summarising the selection criteria and for the electron branch of the e+τ-jet trigger. The values have been chosen for the $10^{32}\,cm^{-2}s^{-1}$ regime.

HLT τ-jet of e+τ-jet Cut	Value
L1 seed	L1 Iso e/γ E_T >10 AND L1 τ-jet E_T >20 GeV
L2 E_T	E_T >15 GeV
e-L2 τ-jet Non-Coll (N-C)	At least one HLT e-L2 τ-jet pair separated by $\Delta\eta$ >0.3 OR $\Delta\phi$ >0.3
L2 ECAL Iso	ΣE_T^{ECAL} <5 GeV within 0.15< ΔR <0.5
L2.5 Lead Pixel Track finding	3 pixel hits, ΔR_m=0.1, p_T^{LdgTrk} >3 GeV/c
L2.5 Pixel Iso	ΔR_{iso}=0.5, ΔR_s=0.15 3 pixel hit track, p_T^{trk} >1 GeV/c, $\Delta z_{trk-vtx}$ <2 mm

Table 3.6: Table summarising the selection criteria and for the τ-jet branch of the e+τ-jet trigger. The values have been chosen for the $10^{32}\,cm^{-2}s^{-1}$ regime. Note that the τ-jet branch HLT algorithms will only start if the electron criteria of the e+τ-jet trigger are satisfied.

threshold of the Single Isolated Electron trigger, in QCD events with $\hat{p}_T$ >15 GeV/c for the $10^{32}\,cm^{-2}s^{-1}$ regime is summarised in Table 3.7. A final QCD rate of (0.7±0.2) Hz is obtained for the $10^{32}\,cm^{-2}s^{-1}$ regime and is acceptable considering the total HLT bandwidth of 100 Hz available during this period.

HLT_IsoEle12_IsoTau_Trk3	Rate (Hz)	Efficiency Rel
L1 (Iso e/γ + τ-jet) (10,20) GeV	2910±10	0.020
L1 e Match	2670±10	0.917
HLT e E_T >12 GeV	1690±8	0.632
HLT e Hcal Isolation	1490±7	0.881
HLT e Pixel Match	152±2	0.102
HLT e Loose 1/E-1/P	135±2	0.894
HLT e Track Isolation	46.9±1.3	0.346
N-C HLT e-L2 τ-jet E_T >15 GeV	11.9±0.6	0.255
L2 τ-jet ECAL Iso	8.7±0.5	0.725
L2.5 τ-jet p_T^{Ldg} >3.GeV/c	4.7±0.4	0.550
L2.5 τ-jet Pixel Iso	0.7±0.2	0.159

Table 3.7: Table summarising the performance step-by-step of the HLT_IsoEle12_IsoTau_Trk3 trigger on QCD events with $\hat{p}_T$ >15 GeV/c for the $10^{32}\,cm^{-2}s^{-1}$ regime. The error on the rate represents the binomial statistical uncertainty scaled by the appropriate factor to form a rate. A total rate of (0.7±0.2) Hz is obtained.

Trigger Efficiency

Table 3.8 shows the performance of the HLT_IsoEle12_IsoTau_Trk3 trigger on Z→ $\tau\tau \rightarrow e + \tau$-jet events pre-selected using the criteria of Table 3.2. The L1 efficiency is artificially increased due to the lack of a collinearity check between the electron and the τ-jet. This means that due to the bad L1 τ-jet resolution and the over-correction of the L1 τ-jet energy scale coming from the generic L1 jet corrections (Figure 3.12), the electron could fire both the L1 e/γ and L1 τ-jet legs. In order to have a physical e+τ-jet trigger, a filter is applied at HLT which requires at least one pair of HLT electrons and L2 τ-jets to be separated by $\Delta\phi$ >0.3 or $\Delta\eta$ >0.3. The loss of signal efficiency in the HLT electron pixel matching step, is due to the tighter pixel matching criteria applied at HLT compared to offline as shown in Table 3.1. The loose (1/E-1/P) cut ensures that all HLT electrons have a reconstructed track associated to them. Even though events have been pre-selected to contain one

well identified offline GSF electron the efficiency of this cut is not 100% as the track reconstruction at HLT uses Kalman fitted tracks which might fail reconstruction for electrons radiating large fraction of their energy.

The L2 E_T and non-collinearity requirement between the HLT electrons and L2 τ-jets cuts out 20% of signal events even though they have been pre-selected containing an offline non-collinear GSF electron and a PFTau with $E_T > 15\,GeV$. This is mainly due to events where the L1 τ-jet list did not contain the true τ-jet candidate. Instead the L1 τ-jet was triggered by the same object which fired the L1 e/γ trigger. Therefore when the L1 e/γ and τ-jet objects are passed on to HLT, the non-collinearity requirement filters out these events. Another reason is due to a badly reconstructed τ jet energy at L2.

The requirement to have a pixel track made up of three pixel hits associated with the L2 τ-jet is mainly responsible for the loss of efficiency of the L2.5 τ-jet leading track finding step. Future versions of the L2.5 τ-jet trigger will use mixed triplet seeds using both pixel and tracker hits in order to increase this efficiency. Finally an efficiency of (44.6±1.6)% is obtained on events pre-selected using the criteria described in 3.2.

HLT_IsoEle12_IsoTau_Trk3	Efficiency Cumulative	Efficiency Rel
L1 (Iso e/γ + τ-jet) (10,20) GeV	0.910± 0.020	0.910
L1 e Match	0.910± 0.020	1.000
HLT e E_T >12 GeV	0.903± 0.023	0.993
HLT e Hcal Isolation	0.899± 0.023	0.996
HLT e Pixel Match	0.774± 0.021	0.860
HLT e Loose 1/E-1/P	0.729± 0.020	0.942
HLT e Track Isolation	0.720± 0.020	0.988
N-C HLT e-L2 τ-jet E_T >15 GeV	0.580± 0.018	0.805
L2 τ-jet ECAL Iso	0.567± 0.018	0.978
L2.5 τ-jet p_T^{Ldg} >3.GeV/c	0.484± 0.017	0.853
L2.5 τ-jet Pixel Iso	0.446± 0.016	0.922

Table 3.8: Table summarising the performance step-by-step of the HLT_IsoEle12_IsoTau_Trk3 trigger on Z$\rightarrow \tau\tau \rightarrow e + \tau$-jet events. These events have been pre-selected using the criteria described in 3.2. The errors represent the binomial statistical uncertainty. An efficiency of (44.6±1.6)% is obtained.

Figure 3.13 shows the L1 e+τ-jet efficiency as a function of the offline PFTau (left) and electron (right) E_T. The L1 objects are required to match the offline objects

which in turn match the true Monte Carlo (MC) objects within $\Delta R < 0.5$. The difference in the plateau efficiency value for electrons and PFTaus is due to the worse L1 τ-jet resolution as shown in Figure 3.12 which smears the turn on curve. Furthermore the L1 τ-jet E_T scale over-estimates the true τ-jet E_T due to the inappropriate L1 jet MC based corrections which are applied to L1 τ-jets.

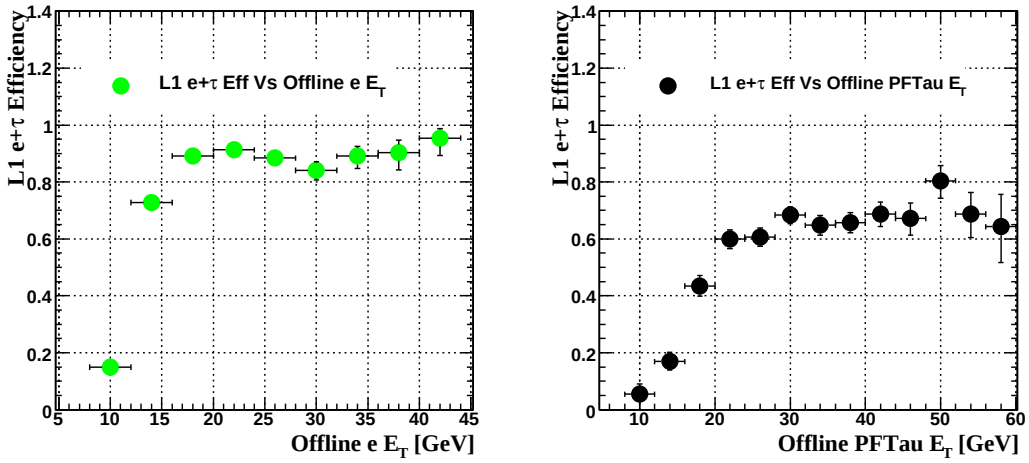

Figure 3.13: The L1 e+τ-jet efficiency as a function of the offline PFTau (right) and electron (left) E_T. The L1 objects are required to match the offline objects which in turn match the true MC objects within $\Delta R < 0.5$.

The HLT turn on curves for the HLT τ-jet and electron of the e+τ trigger are shown in Figure 3.14. The HLT electron efficiency (of the e+τ-jet trigger) is measured with respect to events firing the L1 e+τ-jet trigger. The HLT electrons are required to match the offline electrons which in turn match the true MC objects within $\Delta R < 0.3$. The HLT τ-jet efficiency is measured with respect to events passing the HLT electron leg of the e+τ-jet trigger. The HLT τ-jets are required to match the offline electrons which in turn match the true MC objects within $\Delta R < 0.3$. The sharper turn on for the HLT electron is due to the better electron resolution at HLT compared to the HLT τ-jet resolution as shown in Figure 3.12.

Table 3.9 summarises the additional efficiency obtained by combining the HLT_IsoEle12_IsoTau_Trk3 trigger with the single isolated electron trigger with $E_T > 15$ GeV (HLT_IsoEle15_L1I) in a logical OR, compared to using the HLT_IsoEle15_L1I

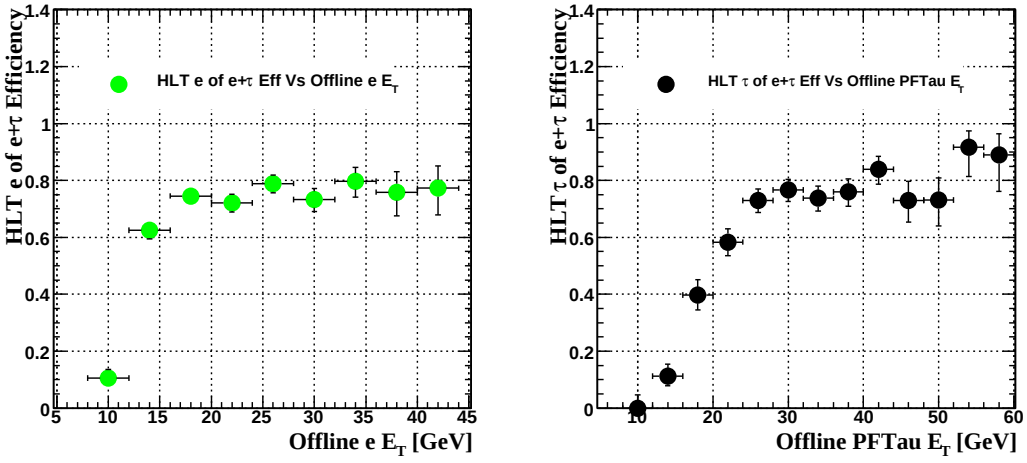

Figure 3.14: Right: The HLT τ efficiency of the e+τ-jet trigger as a function of the offline PFTau E_T. Left: The HLT e efficiency of the e+τ-jet trigger as a function of the offline electron E_T. The HLT objects are required to match the offline objects which in turn match the true MC objects within $\Delta R < 0.2$.

trigger by itself. A gain of $\sim 6.5\%$ is obtained on $Z \rightarrow \tau\tau \rightarrow e + \tau$-jet events satisfying the pre-selection criteria of Table 3.2. This marginal gain is due to the small difference between the HLT electron E_T thresholds of the two triggers. Therefore the e+τ trigger will play a more important role during higher instantaneous luminosity regimes such as $2 \times 10^{33}\,\mathrm{cm}^{-2}\mathrm{s}^{-1}$ where due to the higher rates, the E_T threshold of the single isolated electron trigger will have to be increased to $> 20\,\mathrm{GeV}$ thus making the gain of the e+τ-jet more prominent [54].

Trigger Type	HLT_IsoEle15_L1I	IsoEle15_L1I OR IsoEle12_IsoTau_Trk3
Efficiency	$(61.4 \pm 2.5)\%$	$(65.4 \pm 2.5)\%$
$((\lvert\epsilon^{hlt}_{e\|\|e\tau} - \epsilon^{hlt}_{e}\rvert)/\epsilon^{hlt}_{e}$	$\sim 6.5\%$	

Table 3.9: Additional efficiency obtained by combining the HLT_IsoEle12_IsoTau_Trk3 trigger with the single isolated electron trigger with $E_T > 15\,\mathrm{GeV}$ (HLT_IsoEle15_L1I) in a logical OR, compared to using the HLT_IsoEle15_L1I trigger by itself.

3.5 Conclusions

A detailed description of the electron and τ-jet reconstruction algorithms both offline and at trigger level was presented. Furthermore the motivation and performance

of the e+τ trigger (HLT_IsoEle12_IsoTau_Trk3) for the $10^{32}\,\mathrm{cm}^{-2}\mathrm{s}^{-1}$ regime on Z$\rightarrow$ $\tau\tau \rightarrow e + \tau$-jet and QCD di-jet events was also presented. Given the parameters of Table 3.5 and the offline pre-selections of Table 3.2 a Signal efficiency of (44.6$\pm$1.6)% with a QCD rate of (0.7$\pm$0.2) Hz for an instantaneous luminosity of $10^{32}\,\mathrm{cm}^{-2}\mathrm{s}^{-1}$ was obtained. Finally the efficiency of the logical OR between HLT_IsoEle15_L1I, HLT_IsoEle12_IsoTau_Trk3 was compared to the HLT_IsoEle15_L1I yielding efficiencies of $(65.4 \pm 2.5)\%$ and $(61.4 \pm 2.5)\%$ respectively. The marginal gain in efficiency was due to the small difference between the HLT electron $\mathrm{E_T}$ thresholds of the two triggers. Therefore e+τ trigger will play a more important role during the higher instantaneous luminosity regimes such as $2 \times 10^{33}\,\mathrm{cm}^{-2}\mathrm{s}^{-1}$ since due to the higher rates the electron $\mathrm{E_T}$ threshold of the single isolated electron trigger will have to be increased to $> 20\,\mathrm{GeV}$.

During the LHC start-up, the HLT_IsoEle12_IsoTau_Trk3 selections will be re-tuned in order to increase the efficiency on τ-jets by loosening the pixel triplet requirement. This could be achieved for example by building tracks using pixel doublet hits together with a hit in the silicon strip layers for the cases when a third pixel hit is not found. Moreover by integrating PF objects in the trigger, a better QCD rejection could be achieved. In particular the use of more sophisticated PF based calorimetric shower shape variables at L2 has been a major improvement of the τ-jet triggers at CMS over the last few months. These improvements need to be further studied and propagated to the later stages of the τ trigger and integrated with the e+τ trigger. Finally commissioning the τ-jet triggers using the first LHC collision data would ensure that CMS is ready for a wide range of τ related physics.

Chapter 4

L1 τ jet trigger commissioning

4.1 Commissioning the L1 τ-jet trigger using Cosmic Run Data

4.1.1 Introduction

The Cosmic RUn at ZEro Tesla (CRUZET) took place during the summer of 2008. The purpose of this run was to commission the full detector, trigger and reconstruction using cosmic muon, noise or randomly triggered events in preparation for the LHC start-up. This exercise took place in four stages, with a continuous running period of approximately one week per stage followed by a period of analysis and fixes. The tracker and pixel subsystems became available during the end of the third stage. This meant that the full detector apart from the magnetic field were active in the underground detector cavern.

This chapter describes the validation of the L1 τ-jet trigger algorithms as described in Section 3.3.2 using random and cosmic muon triggered events. The 1σ noise fluctuation of a reconstructed HCAL tower is expected to be $\sim 0.3\,\text{GeV}$. This makes HCAL noise an important factor when considering jets which can contain O(100) of such towers [9]. Therefore the goal of this study was to understand the effect that HCAL noise has on the L1 τ-jet algorithms both in terms of rate and isolation. The

L1 jet rate due only to noise was determined using randomly triggered events whereas the effect of HCAL noise on the L1 τ-jet algorithmic efficiency was determined by looking at localised calorimetric energy depositions originating from cosmic muons.

4.1.2 Software information

CMSSW version CMSSW_2_0_12 was used to analyze the datasets from CRUZET1 and CRUZET3 which were collected during the first and third period of the CRUZET excercise.

CRUZET1 used CMSSW_2_0_7 for the reconstruction with dataset /Cosmics/CRUZET1_CRUZET_V3_v1/RECO[1].

CRUZET3 used CMSSW_2_0_11 for the reconstruction with dataset /Cosmics/CRUZET3_CRUZET3_V2P_v3/RECO.

4.1.3 The L1 calorimetric emulation

During the CRUZET exercise the L1 jet hardware was undergoing commissioning and hence was not reliable for this study. Moreover due to problems with the timing of the trigger primitive generation, the L1 hardware emulator could not be used for the majority of the CRUZET running period. So the L1 calorimetric emulation was used, which instead of running over trigger primitives [52] (ECAL and HCAL reconstruction by the L1 hardware), runs the L1 τ-jet algorithms over offline ECAL and HCAL reconstructed hits (rec hits) and is part of the official CMS SoftWare package. The advantages of this method are that firstly it produces regions and jets directly from rec hits without undergoing the numerous energy scale transformations that take place in the emulator and the hardware. Secondly the L1 calorimetric emulation shows a good agreement (within 10%) with the L1 hardware emulator as shown in Figure 4.1 where a [18]. Lastly the new isolation veto bit which has not yet been implemented in the hardware and emulator, was implemented in the

[1]The dataset is given in the standard CMS data base convention

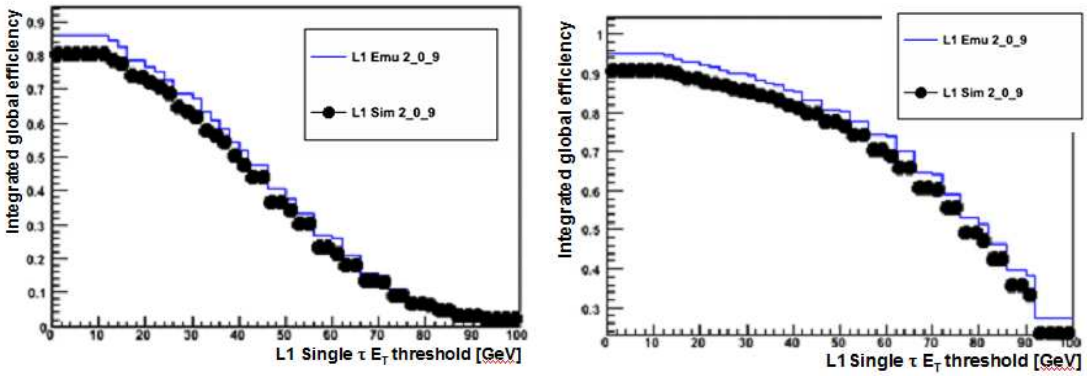

Figure 4.1: Comparison of the L1 Single τ-jet trigger efficiency in simulated Z$\rightarrow \tau\tau \rightarrow \tau$-jet$\tau$-jet (left) and QCD events with $\hat{p}_T \in [80, 120]$ GeV/c (right) between the L1 hardware emulator (solid line) and the L1 Calorimetric emulation (closed circles). No L1 jet corrections were applied. The L1 hardware emulator read in trigger primitives and the L1 calorimetric emulation reads in ECAL and HCAL rec hits. Both methods agree within 10% [18].

calorimetric emulation and hence could be studied for the first time with real data. It is worth noting that the L1 jet corrections were switched off as they will need to be recalculated for startup and they also add a layer of ambiguity in the absolute E_T scale as they are not tuned for noise and muon energy depositions in the calorimeter.

4.1.4 Run selection and event pre-selections

The triggers used to select events were only based on L1 decisions, as the HLT only became available during the very last period of this exercise. In order to quantify the L1 jet rate due to HCAL noise, randomly triggered runs where used. This trigger was based on a random number generator which would send a L1 accept decision at random intervals but with the constraint on the L1 rate of ~ 90 Hz. The cosmic muon triggered runs used L1 muon CSC and DT triggers in a logical OR combination with a dedicated calorimetric "presence of energy" and "top-bottom" ECAL barrel coincidence triggers which required a deposition of energy on positive and negative ϕ regions. Some of the Muon and ECAL regions used to trigger on cosmic muons events are shown in Figure 4.2. DT sectors 3 or 4 or 5 or 9 or 10 or 11 in all wheels were used. For the ECAl barrel "top-bottom" trigger regions (5 or 6) and (14 or 15) were used [55].

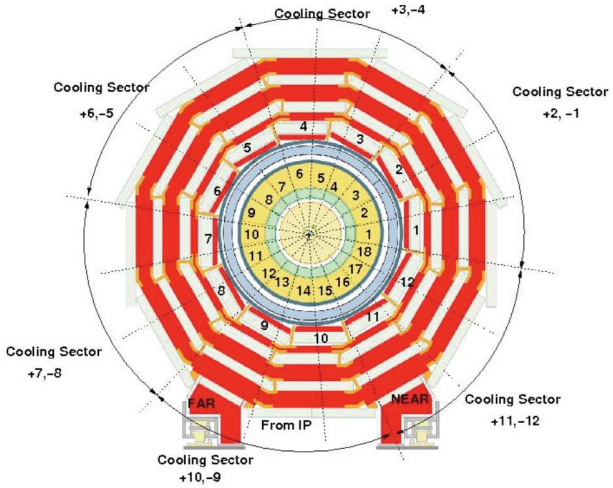

Figure 4.2: View of the DT and calorimeter regions used in triggering on cosmic muon events during the CRUZET exercise.

A set of pre-selection criteria were applied to the cosmic muon triggered events in order to ensure good quality muons deposit localised amounts of energy in the calorimeter just as a τ-jet would. These selections are summarized below:

1. A tight cut on the number of muon chamber hits per track $N_h > 20$. The distribution of the number of muon system hits per standalone track is shown in Figure 4.3. The peaks are due to various number of chambers which are hit depending on the angle the muon crosses the detector.

2. Transverse impact parameter (d0) of muon track $|d0|<70\,cm$, the d0 distribution distribution is shown in Figure 4.4

3. Longitudinal impact parameter (dz) of muon track $|dz|<70\,cm$, the dz distribution is shown in Figure 4.4. The asymmetry is due to the position of the CMS detector relative to the cavern shaft.

4. Extrapolated muon track trajectory to the ECAL crosses the EB.

5. Extrapolated muon track trajectory to the HCAL crosses through maximum two HCAL towers. If two HCAL towers are crossed, these towers must share a common face ($i\Delta\eta$=1 XOR $i\Delta\phi$=1), where $i\eta$ and $i\phi$ represent the numbering scheme of HCAL towers in η and ϕ respectively.

6. Only two muon tracks satisfying the above criteria $N^{\mu}=2$ and no other standalone muon tracks in the event.

7. The extrapolated trajectories to the ECAL surface of the two muon tracks satisfying the above criteria must cross the EB at opposite ϕ and have a relative opening angle α <0.15 rad. The distribution of α is shown in Figure 4.3.

Selections 1-4 ensure a well reconstructed muon traverses through the barrel region of the calorimeter and relatively close to the nominal interaction point.
Selection 5 ensures that muons will cross through a small section of the barrel and restrict muons from depositing energy over a large calorimeter region. Furthermore the requirement on two crossed towers sharing a common face, attempts to make the deposition "τ-jet like" by satisfying the L1 τ-jet Activity patters of Section 3.3.2 Selection 6 selects well understood clean events, and rejects multiple cosmic muon events or events with fake muons as they add ambiguity to this study. Finally Selection 7 ensures that the muon did not scatter through a large angle which could result in a non localised energy deposition in the calorimeter and the loss of the scattered reconstructed muon track. The total efficiency of all the above selections is 0.05%.

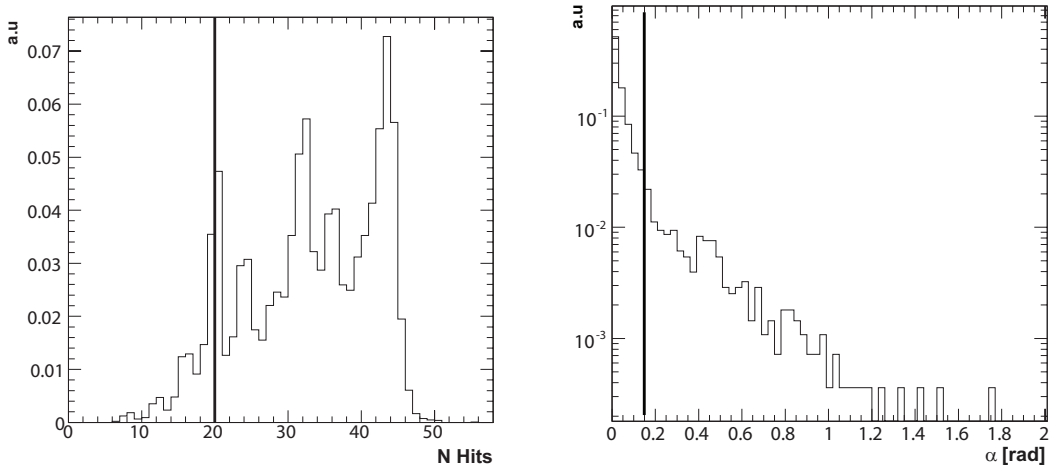

Figure 4.3: Left: Distribution of the number of hits of reconstructed standalone muon tracks in CRUZET 3 data. A cut was placed at $N_h > 20$. Right: Distribution of the opening angle alpha between two standalone muon tracks in events with two standalone muons. A cut was placed at α <0.15 rad. Events were triggered using the triggers described in Section 4.1.4. No other selections were applied.

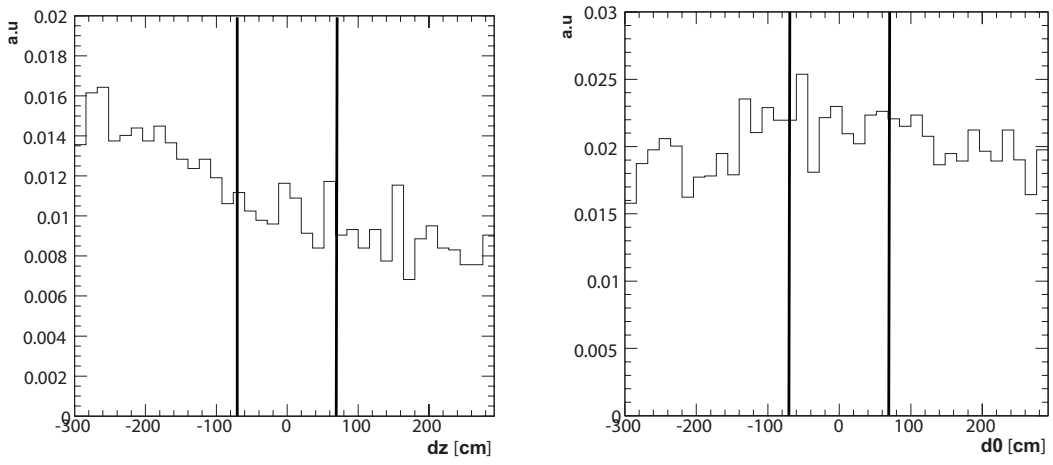

Figure 4.4: Distribution of the longitudinal (left) and transverse (right) impact parameters of reconstructed standalone muons in CRUZET 3 data. Cuts where placed at |dz|<70 cm and |d0|<70 cm respectively. Events where triggered using the triggers described in Section 4.1.4. No other selections were applied. The asymmetry in dz is due to the position of the cavern shaft relative to the CMS detector.

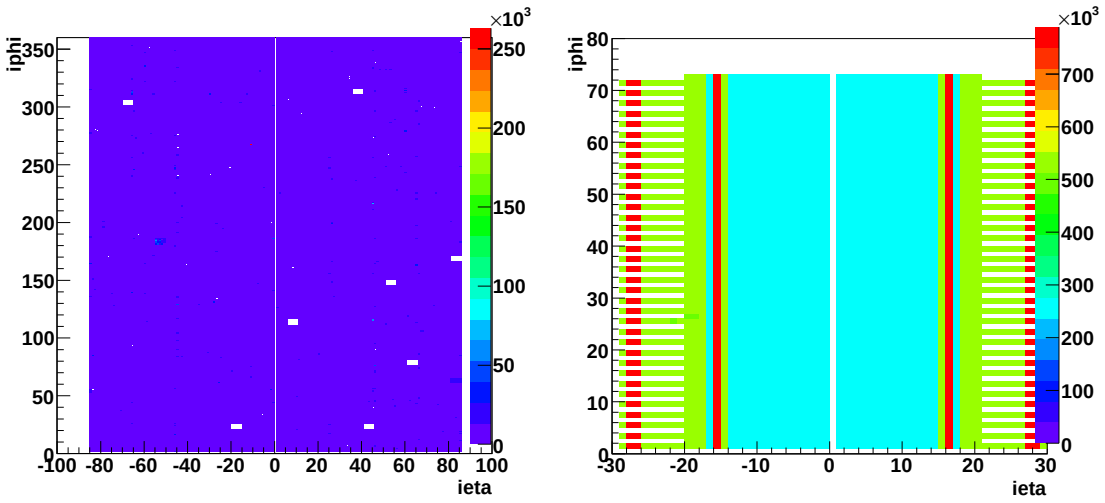

Figure 4.5: ECAL (left) and HCAL (right) detector element η-ϕ map (denoted as iη, iϕ) for non zero energy rec-hits is shown. The ECAL extends up to the end of the barrel as no ECAL end-caps had been installed.

4.1.5 Evaluation of L1 jet rate due to calorimetric noise

In total there was only one random triggered run available, taken during the first period of CRUZET (CRUZET 1). In order to ensure that there was no coincidence between a random trigger and a cosmic muon, a veto was placed on events containing at least one standalone track with loose track quality criteria placed. The efficiency of this veto was >99%. Figure 4.5 shows the η-ϕ map of the ECAL and HCAL rec-hits containing non-zero energy over this entire run. The blank areas on the ECAL correspond to problematic crystals or supermodules which were masked to read out zero energy. The ECAL barrel is only shown as the end-caps had not been yet installed. The HCAL shows all channels were read out correctly. The non uniformities in the number of hits is due to the double and triple read out layers of the HCAL. For the region of iη >28, the iϕ numbering scheme changes to account for the larger HCAL towers ($\Delta\phi$=0.348 rad) in the HF. However as this analysis is only interested in L1 central and τ-jets the HF is not required, where the L1 central jets are L1 jets that have failed the L1 τ-jet Activity and Isolation criteria.

The E_T distribution of the L1 calorimetric regions and of the L1 jets both τ and central are shown in Figure 4.6. It is evident that even though these are randomly

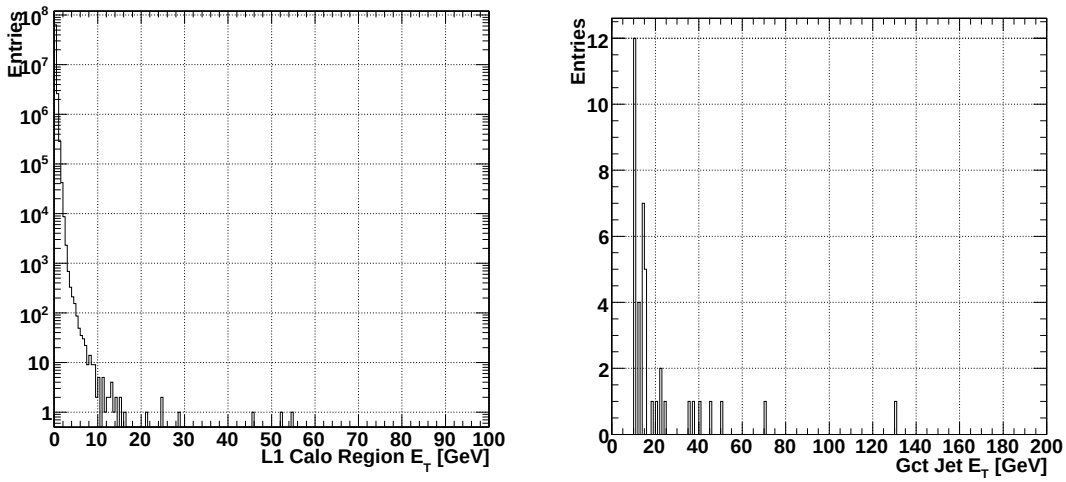

Figure 4.6: E_T distributions of the L1 calorimetric regions (left) and L1 jets (right) in random triggered run of CRUZET 1.

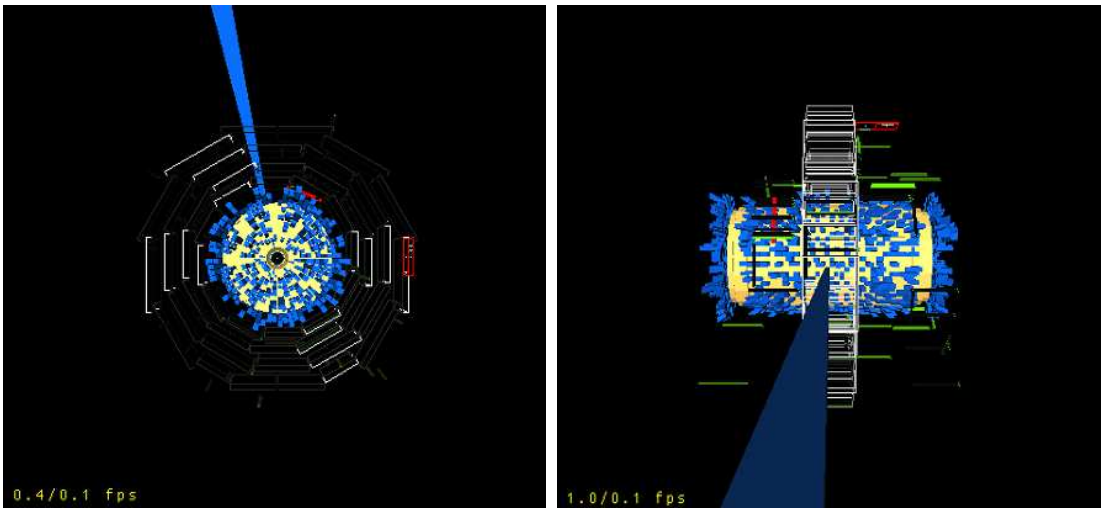

Figure 4.7: Event display of random triggered run 43636 in X-Y view (left) and R-Z view (right). DT wheel 0 is shown. The HCAL barrel and endcaps are in orange and the hits with a minimum energy of 0.5 GeV are denoted as blue towers. A single HCAL tower with 136 GeV of energy due to HPD noise is shown. A closer inspection showed that there is no ECAL energy either in the vicinity or at π from this particular tower.

triggered events with no coincident cosmic muon, a jet with E_T in excess of 100 GeV was reconstructed. An event display of the event with a L1 jet with E_T =132 GeV is shown in Figure 4.7. The size of the blue blocks indicate the energy deposited in the HCAL towers with a minimum threshold of 0.5 GeV. As it can be seen there is a single tower with E=136 GeV which is due to noise originating from the HCAL Hybrid Photo Diode (HPD). A check on the ECAL energy in either the vicinity or at π from this particular tower shows no deposition, confirming that it is due to HCAL noise. Figure 4.8 shows the average number L1 jets both central and τ with E_T greater than the value denoted on the x-axis ($P_{L1\,jet}$). A working point of E_T >40 GeV with $P^{40}_{L1\,jet}$=$(1.5 \pm 0.8 \times 10^{-5})$ was chosen. Even though it is too low for an unprescaled L1 single jet trigger at LHC, it gives an upper limit estimate of the fake rate of L1 jets due to noise with sufficient statistical significance. Random triggered events satisfying the L1 Jet E_T >40 GeV requirement only had one jet with E_T >40 GeV, therefore a trigger rate can be evaluated by calculating $R = \frac{P^{40}_{L1\,jet}}{Bx}$ where Bx is the bunch crossing time. Considering that for the first physics run of LHC the bunch crossing time will be 75 ns, this will give rise to a rate of approximately 200 ± 106 Hz which accounts for ~2% of the 12 kHz bandwidth which will be used for startup. The error corresponds to the binomial statistical uncertainty on the average number of jets per event with L1 Jet E_T >40 GeV. For the nominal 25 ns bunch crossing this L1 jet rate triples to $(600 \pm 318)\dot{\text{H}}$z, however by this time the full L1 bandwidth of 100 kHz will have been deployed giving ~0.6% of the total L1 bandwidth being occupied by L1 central and τ-jets with E_T >40 GeV. The effect of calorimetric noise on the rate of L1 jets is present however it does not occupy a large fraction of the total L1 available bandwidth. One thing to note is that this study only offers an estimate of this rate as the detector running conditions and L1 jet corrections are likely to change once LHC turns on. Moreover these noise rates are only a lower estimate as the presence of the magnetic field as well as calorimeter response degradation could potentially increase the effective calorimetric noise.

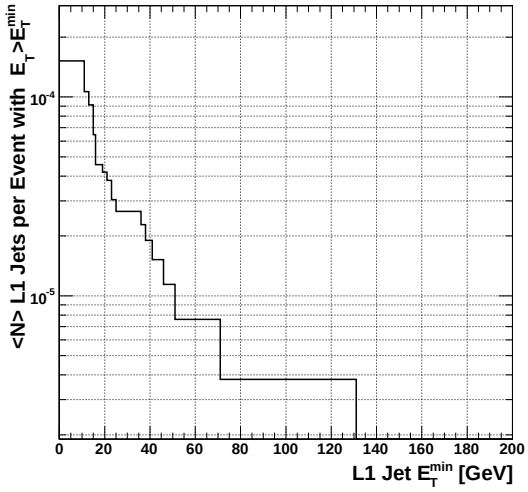

Figure 4.8: Integrated number of L1 jets both central and τ with E_T greater than the value denoted on the x-axis in randomly triggered run.

4.1.6 Evaluation of the algorithmic L1 τ-jet efficiency using cosmic muons

As cosmic muons depositing a localised amount of energy in the calorimeter make good τ-jet candidates, approximately 30M triggered events from the third stage of CRUZET (CRUZET 3) were analyzed. Out of these approximately 15K events passed the pre-selections of Section 4.1.4.

Muon properties

The two top plots of Figure 4.9 show the η and ϕ distributions of the cosmic muon track after the pre-selections. The plots indicate that the muons are coming in downwards in a central direction. An important aspect of the cosmic muon reconstruction compared to the muon reconstruction from pp collisions is that the outermost and innermost track states are reversed, with the innermost state now being the outermost muon detector layer. These standalone tracks are then propagated to the calorimeter surface assuming a straight line trajectory since there is no magnetic field. The two bottom plots of Figure 4.9 show the η and ϕ distributions of the track position in the outermost detector layer, against the η and ϕ positions of the

track propagated to the calorimeter surface (HCAL η,ϕ). All the track positions are measured with respect to (0,0,0). It can be seen a good agreement is achieved between the track "Inner" and the propagated positions. The width of the bottom left plot is because tracks that are coming in with non-zero η, are propagated to a different detector layer. The two peaks of the bottom right plot denote the positions of the incoming and outgoing muon.

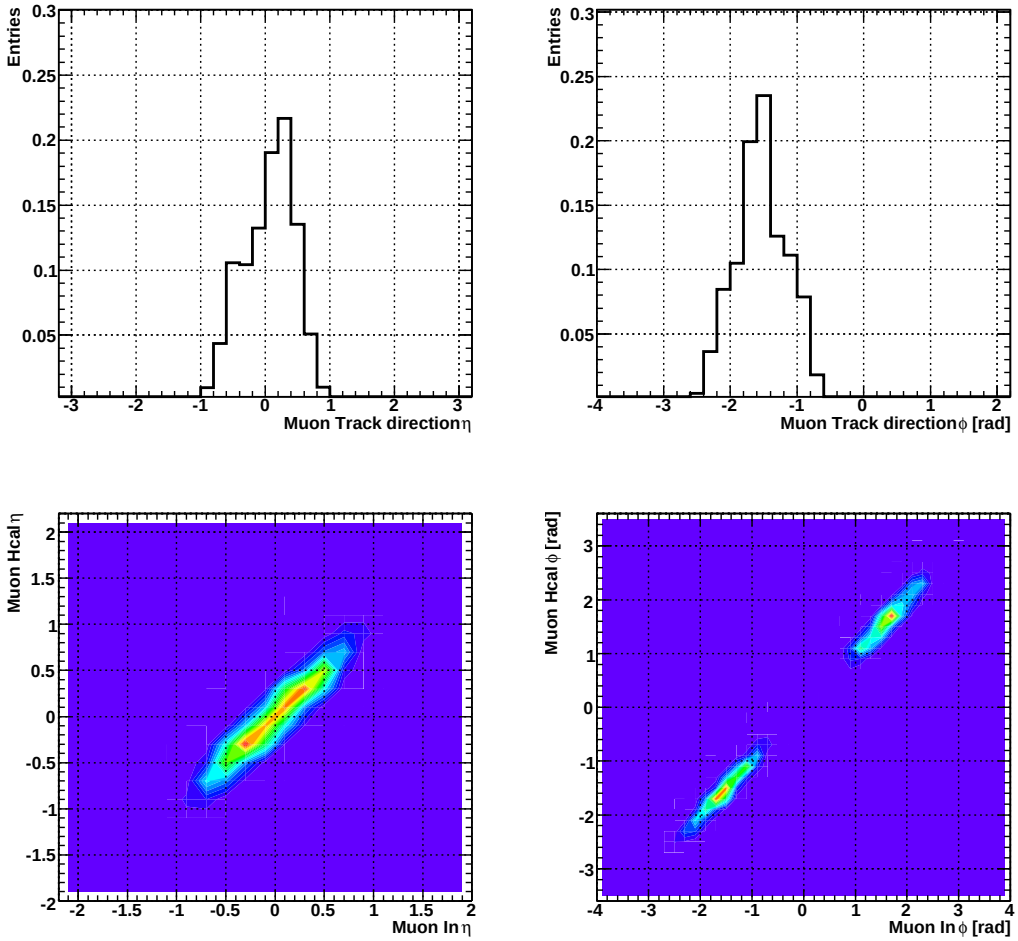

Figure 4.9: Top plots: η and ϕ distributions of the muon track direction. Bottom plots: η and ϕ distributions of the "Inner" muon track position plotted against the propagated track η and ϕ positions on the calorimeter surface.

The average energy deposited in the ECAL and HCAL is shown in Figure 4.10. The left plot shows the sum of NxN ECAL crystal energy around the most energetic crystal in the vicinity of the propagated track position to the ECAL surface. Most of the ECAL energy is contained within 9x9 crystals. The excess at zero is because of unclustered energy due to errors in the propagated position which could occur due to scattering of the muon in the HCAL. The peak is at 250 MeV. The right plot shows the equivalent plot but for 3x3 and 5x5 sum of HCAL tower energy around the most energetic tower in the vicinity of the propagated track position to the HCAL surface. The means of gaussians fitted over the range of -0.1 GeV to 5 GeV are 1.89 GeV and 1.91 GeV respectively indicating that most of the energy is contained within a 3x3 HCAL tower regions and going to 5x5 further smears the distribution with noise. The negative energy values are due to the lack of zero suppresion on the rec-hits over the entire CRUZET exercise. Figure 4.11 shows a typical event display of a cosmic muon crossing through the entire detector and depositing energy at the calorimeter.

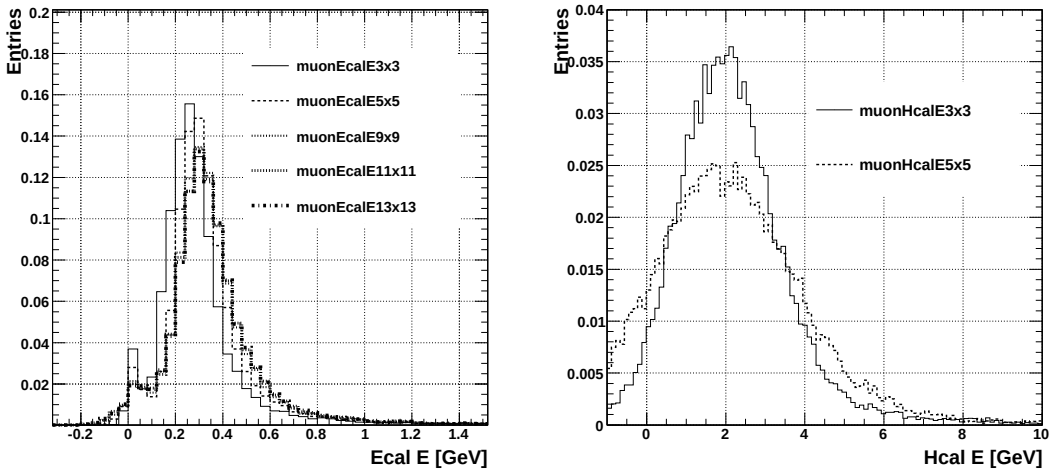

Figure 4.10: Left: Sum of NxN ECAL crystal energy around the most energetic crystal in the vicinity of the propagated track position to the ECAL surface. Right: Sum of HCAL tower energy around the most energetic tower in the vicinity of the propagated track position to the HCAL surface. The mean values of a gaussian fit between -0.1 GeV to 5 GeV are $\sigma_{3\times3}$ = 1.89 GeV and $\sigma_{5\times5}$=1.91 GeV.

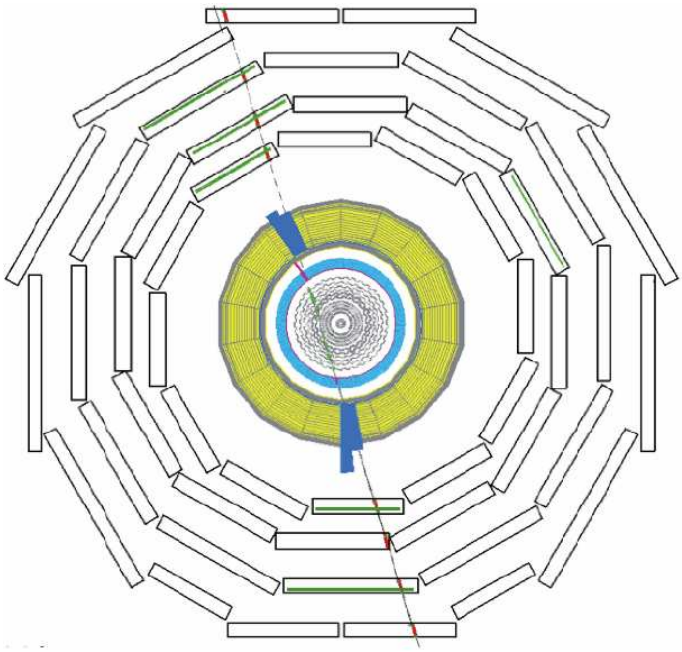

Figure 4.11: Typical event display of a cosmic muon crossing through the entire detector and depositing energy at the calorimeter. The HCAL energy is denoted in blue and the ECAL in pink. The hits in the muon chambers and the tracker are also visible.

L1 calorimetric regions and jets

Figure 4.12 shows the E_T distribution of the closest in ΔR L1 calorimetric region within a cone ΔR<0.5 around the propagated track position to the HCAL surface (open squares). Overlayed is the E_T distribution of L1 calorimetric regions in randomly triggered events (open circles) for comparison. Each distribution is normalized to unity. A larger high energy tail is seen in the muon triggered sample. The effect of the muon energy deposition is clearly visible within the range $0<E_T<50$ GeV. Above that value however due to lack of statistics the effect of noise and muon energy cannot be disentangled. Figure 4.12 also shows the ΔR distribution between the propagated track position to the HCAL surface and the closest in ΔR L1 jet. (equivalent to the L1 calorimetric region position as noted in Section 3.3.2). A match is defined by requiring ΔR <0.5 between the muon position and the closest in ΔR L1 jet (or L1 region). The peak near ΔR=3 is due to a L1 jet formed by the incoming/outgoing muon partner. The width of that peak is mainly due to the L1 jet position resolution with respect to the propagated muon track

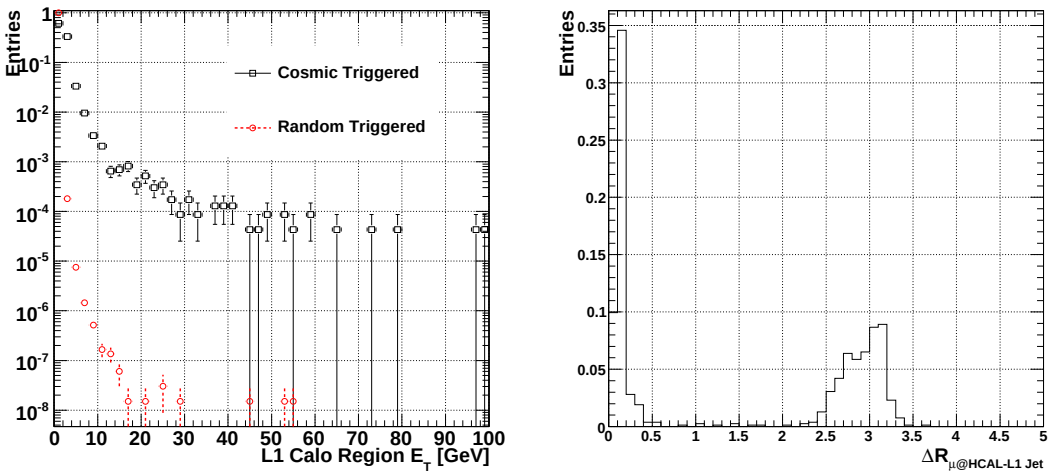

Figure 4.12: Left: E_T distributions of the closest in ΔR L1 calorimetric region within a cone $\Delta R<0.5$ around the propagated track position to the HCAL surface (open squares) and of all L1 calorimetric regions in random triggered events (open circles). Both distributions are normalized to unity. Right: ΔR distribution between the propagated track position to the HCAL surface and the closest in ΔR L1 jet.

position to the calorimeter layer.

L1 τ-jet pattern veto efficiency

By looking at L1 jets formed by a localised calorimetric energy deposition of cosmic muons passing the pre-selections described in Section 4.1.4, the efficiency of the L1 τ-jet pattern veto could be measured. The requirement that the propagated muon track crosses at most two HCAL towers which satisfy one of the L1 τ-jet veto patterns, factorises out the effect of the calorimetric noise on the veto patterns, from a non localised energy deposition of the muon on the calorimeter. However as a muon might shower early in the HCAL, the above pre-selections cannot completely separate this effect from noise. Therefore the results presented in this section represent an estimate of the effect of calorimetric noise on the L1 τ-jet pattern veto efficiency. The fraction of L1 jets both central and τ that pass the τ veto pattern criteria as a function of the L1 jet E_T and η for three different sets of the calorimeter activity cuts - $(E_T^{ECAL}, E_T^{HCAL}) = (1,1)\,GeV$, $(3,3)\,GeV$, $(5,5)\,GeV$ are shown in Figure 4.13. For

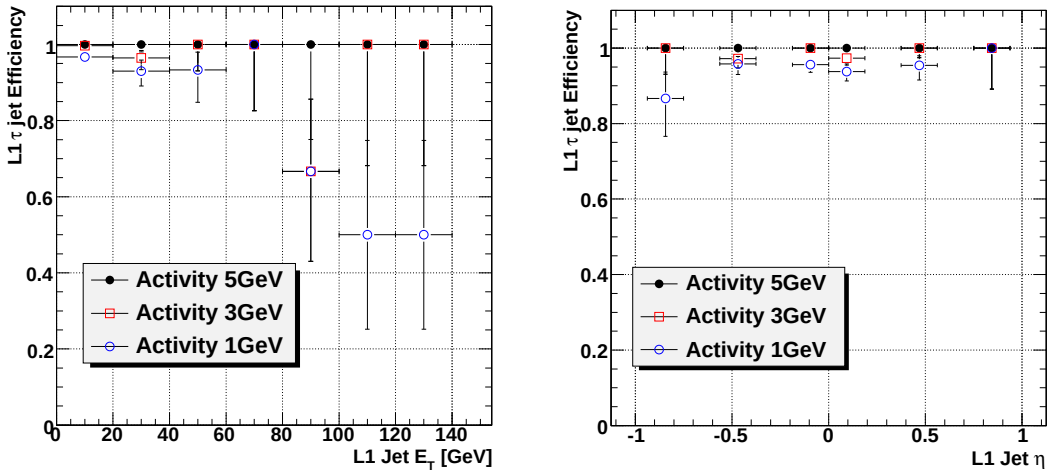

Figure 4.13: Efficiency of the L1 τ-jet pattern veto cut on L1 jets formed by a localised calorimetric energy deposition of cosmic muons. Three different activity cuts are considered, (E_T^{ECAL},E_T^{HCAL}) = (1,1) GeV, (3,3) GeV, (5,5) GeV.

the (1,1) scenario, the veto is sensitive to noise fluctuations leading to degradation in the efficiency as towers other than the ones that are crossed by the muon are considered as active and hence spoil the τ pattern. However for the (3,3) and (5,5) cases, within statistical fluctuations, the efficiency is restored to ∼100%.

L1 τ-jet isolation efficiency

The next step was to measure the effect that calorimetric noise has on the new L1 τ-jet isolation. Once again L1 jets both τ and central were matched to localised calorimetric energy deposition of cosmic muons in events passing the pre-selections of Section 4.1.4. Figures 4.14, 4.15 and 4.16 show the L1 τ-jet efficiency both due to the pattern veto and the new isolation efficiency for a different isolation region cut at E_T^{iso}=3 GeV, 2 GeV and 1 GeV respectively. For each of these cases three different calorimeter activity cuts - (E_T^{ECAL}, E_T^{HCAL}) = (1,1), (3,3), (5,5) were considered. As Figure 4.13 shows that the veto pattern efficiency for the (5,5) case is 100%, the effect that calorimeter noise has on the L1 isolation requirement can be extracted by looking at the (5,5) case of Figures 4.14, 4.15 and 4.16.

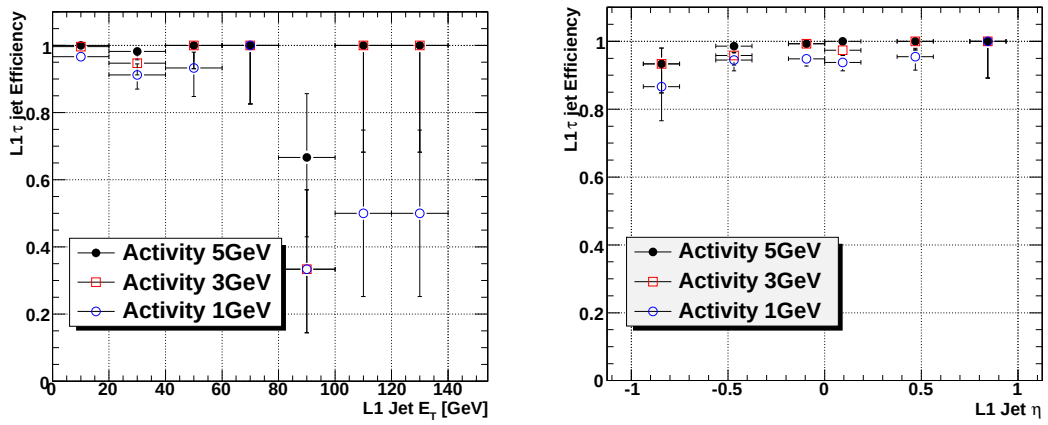

Figure 4.14: Efficiency of the L1 τ-jet isolation and pattern veto cut on L1 jets formed by a localised calorimetric energy deposition of cosmic muons. The isolation cut requires no more than two regions, including the central one, can have E_T >3 GeV. Three different activity cuts are considered, (E_T^{ECAL}, E_T^{HCAL}) = (1,1) GeV, (3,3) GeV, (5,5) GeV.

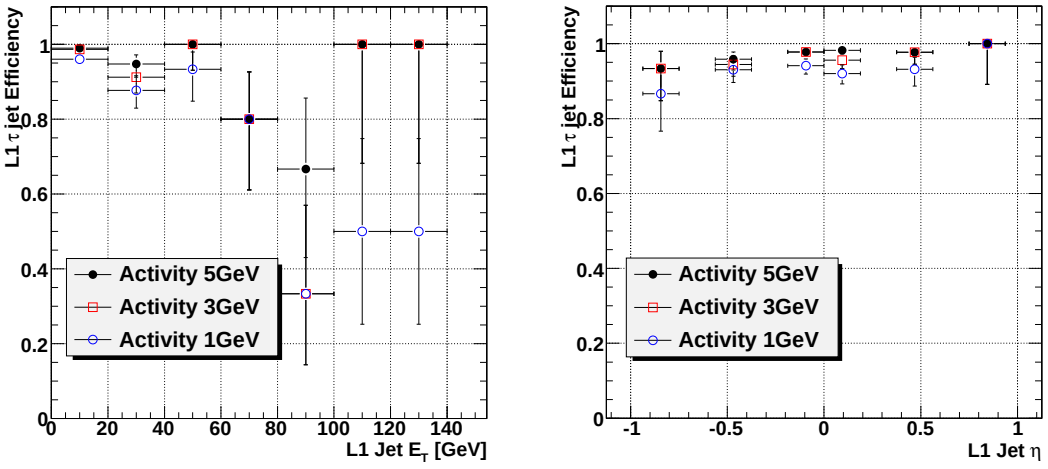

Figure 4.15: Efficiency of the L1 τ-jet isolation and pattern veto cut on L1 jets formed by a localised calorimetric energy deposition of cosmic muons. The isolation cut requires no more than two regions, including the central one, can have E_T >2 GeV. Three different activity cuts are considered, (E_T^{ECAL}, E_T^{HCAL}) = (1,1) GeV, (3,3) GeV, (5,5) GeV.

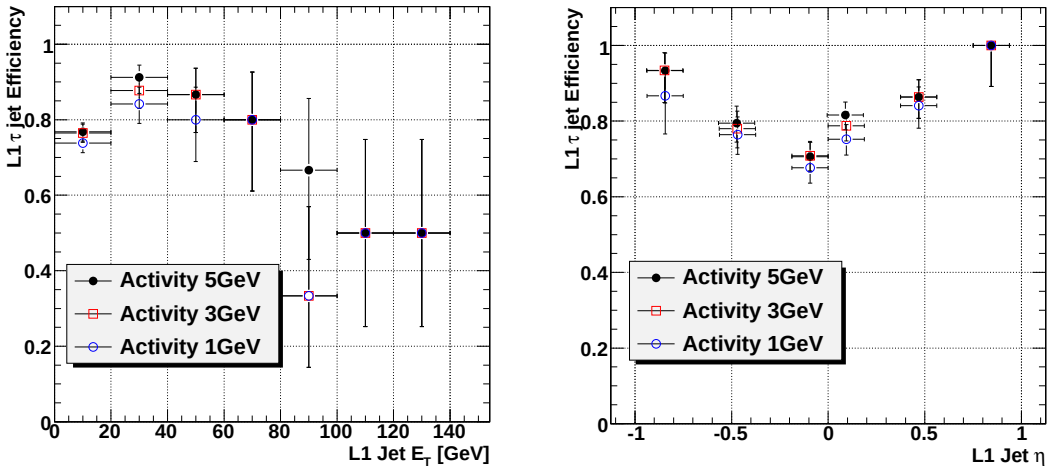

Figure 4.16: Efficiency of the L1 τ-jet isolation and pattern veto cut on L1 jets formed by a localised calorimetric energy deposition of cosmic muons. The isolation cut requires no more than two regions, including the central one, can have E_T >1 GeV. Three different activity cuts are considered, (E_T^{ECAL}, E_T^{HCAL}) = (1,1) GeV, (3,3) GeV, (5,5) GeV. Efficiency drops for such an isolation cut.

For E_T^{iso}=3 GeV and E_T^{iso}=2 GeV the isolation efficiency drops by < 5% due to calorimetric noise. However for E_T^{iso}=1 GeV a visible degradation is observed as the algorithm becomes sensitive to noise in the calorimeter which results in more than one region, apart from the central one, to have an E_T >1 GeV.

4.1.7 Conlcusions

By analysing randomly and cosmic muon triggered events from the first and third periods of the CRUZET exercise, the effect of calorimetric noise on the L1 jet rate and L1 τ-jet algorithmic efficiency were estimated. Considering a L1 jet trigger threshold of 40 GeV the rate of this trigger due to noise accounts only for ∼2% of the total available L1 start-up rate. Furthermore by placing calorimetric activity cuts for the L1 τ veto patterns at (E_T^{ECAL}, E_T^{HCAL}) = (3,3) GeV and the L1 τ-jet isolation threhold of E_T^{iso}=2 GeV results in an acceptable efficiency loss due to calorimetric noise of <5%. With these L1 τ-jet parameters the dominant loss of efficiency in collision data is due to the QCD backgrounds produced along side the Z either from the recoil jet(s) or multiple parton scattering and is ∼20%.

Testing the new Isolation Veto in the L1 hardware as soon as it is made available is of vital importance for the commissioning of the L1 τ-jet trigger . The next step would then be to commission the τ L1 and HLT on electrons from Z$\rightarrow$ *ee* events, during the LHC collisions, which provide a large source of isolated calorimetric depositions and track, allowing for a swift understanding of any algorithmic features and of the isolation parameters which will need to be readjusted to account for the LHC underlying event conditions.

Chapter 5

Reconstruction and selection of Z$\rightarrow \tau\tau \rightarrow \tau$-jet+e+X events

5.1 Introduction

Before Higgs searches involving hadronic and leptonic τ decays can be performed, the detection of existing "standard candles" involving τs should be performed. Furthermore the τ-jet identification efficiency has to be measured using τ-jets originating from these standard candles as it plays an important role in determining the (MSSM) Higgs production cross section and subsequently the MSSM parameter $\tan\beta$. Decays of Z bosons to τ pairs followed by subsequent hadronic and leptonic decays of the τ leptons are a good source of τ-jets. These can be selected above the large hadronic backgrounds by requiring well identified and isolated electrons or muons originating from the leptonic τ decay. By placing stringent criteria on these electrons or muons and selecting events using single lepton (e,μ) triggers, an unbiased and pure sample of τ-jets can be collected in order to measure the efficiency of the τ-jet identification criteria.

This chapter focuses on the selection and reconstruction of Z$\rightarrow \tau\tau \rightarrow \tau$-jet+e+X events as well as methods for estimating the various backgrounds for the purpose of measuring the τ-jet "core" identification efficiency, aimed at $100\,\mathrm{pb}^{-1}$ of integrated luminosity during the early stages of data taking. Therefore tight electron selection

criteria were applied in order to reduce the large backgrounds without requiring harsh τ-jet selections.

5.1.1 Simulated Data Samples and Software Environment

Event generators PYTHIA [56] and MadGraph [57] were used to simulate the hard process, the initial and final state radiation and multiple parton interactions. In contrast to PYTHIA, MadGraph automatically creates the amplitudes for all the relevant hard scattering subprocesses based on leading order Matrix Elements (ME). It then interfaces with PYTHIA to simulate the parton showers and hadronisation.

In light of the LHC schedule $\sqrt{s} = 10\,\text{TeV}$ was used where $\sqrt{s}$ denotes the center of mass energy. PYTHIA was then used for the parton hadronisation and particle decays, and GEANT4 [58] to simulate the interaction of these final state particles with the CMS detector. Finally CMSSW_2_2_1 was used for the detector simulation and reconstruction.

The signal sample for this analysis was a PYTHIA $Z\rightarrow \tau\tau$ sample with $M_Z \in (70, 110)\,\text{GeV/c}^2$ as PYTHIA is more appropriate to describe the low ($< 10\,\text{GeV/c}$) Z p_T region. The main backgrounds of this analysis were QCD di-jet events due to their large production cross-section, W+jets, Z(ee)+jets and $t\bar{t}$+jets events due to the presence of isolated or non-isolated electrons and γ+jets as high p_T photons (γ's) interacting with the detector material and can convert to a pair of isolated electrons. MadGraph was used for the W+jets background, as ≥ 1 final state jets mainly contribute, due to the requirement of both electrons and PFTaus in the event. MadGraph was also used for the Z(ee)+jets and $t\bar{t}$+jets backgrounds as the differences with PYTHIA were small in the context of this analysis.

In order to increase the effective integrated luminosity ($\mathcal{L}$) of the QCD and γ+jets samples, a set of pre-selections at generation stage were applied. The main principle behind such pre-selections was that they should provide a large suppression while guaranteeing that no event failing this pre-selection would pass the single isolated electron trigger with $E_T > 15\,\text{GeV}$. The list of pre-selections on QCD and γ+jets, is summarised below:

- QCD BCtoE ($b/c \rightarrow e$): If a generator level electron has $E_T > 10\,GeV$ and $|\eta| < 2.5$ and originates from a b or c hadron the event is accepted

- QCD EM enriched: Pseudo-cluster generator (PYTHIA) stable particles around a generator (PYTHIA) e or γ seed with $E_T > 5\,GeV$ and $|\eta| < 2.5$ and require $E_T^{calo} < 10\,GeV$ within $\Delta R < 0.2$ at calorimeter surface, charged transverse energy $E_T^{chg} < 5\,GeV$ within $\Delta R < 0.2$ at vertex and has ratio of hadronic to EM energy $E^{\pi,K}/E^{\gamma}$ <0.5. The hadronic and EM energies are evaluated by summing over the energies of stable charged or neutral PYTHIA particles within $\Delta R < 0.2$ at calorimeter surface. If the seed is a γ with $E_T > 20\,GeV$ require isolation within $\Delta R < 0.1$ with $E_T^{calo} < 7\,GeV$ and $E_T^{chg} < 4\,GeV$. Finally if a generator level electron with $E_T > 10\,GeV$ originating from a b or c hadron is found the event is rejected.

- γ+jets: Generator level γ required to have $E_T > 15\,GeV$ and $|\eta| < 2.4$

Table 5.1 summarises the list of samples used together with the effective sample luminosity and filter efficiencies.

In order to reduce their size, the signal, W+jets, Z+jets and $t\bar{t}$+jets samples were filtered by requiring at least one offline generator electron with $E_T > 12\,GeV$ to satisfy $0.8 < E/P < 1.3$. In addition the signal Z$\rightarrow \tau\tau$ sample was required to contain a generator level electron and τ-jet with $|\eta| < 2.5$ originating from the τ leptons.

Finally all samples, apart from the signal, were skimmed by requiring the single isolated electron trigger with $E_T > 15\,GeV$ (HLT_IsoEle15_L1I) to have fired.

Sample	Generator	$\mathcal{L}$	ϵ	$\epsilon \times \sigma$
$Z \rightarrow \tau\tau$ $M_Z \in (70, 110)\,GeV/c^2$	PYTHIA	$1.1\,fb^{-1}$	1.	1086 pb
EM enr. QCD $\hat{p}_T \in (20, 30)\,GeV/c$	PYTHIA	$1.1\,pb^{-1}$	8×10^{-3}	3.2×10^{-3} mb
EM enr. QCD $\hat{p}_T \in (30, 80)\,GeV/c$	PYTHIA	$2.0\,pb^{-1}$	4.7×10^{-2}	4.7×10^{-3} mb
EM enr. QCD $\hat{p}_T \in (80, 170)\,GeV/c$	PYTHIA	$20.8\,pb^{-1}$	1.5×10^{-1}	3×10^{-4} mb
$b/c \rightarrow e$ QCD $\hat{p}_T \in (20, 30)\,GeV/c$	PYTHIA	$2.0\,pb^{-1}$	4.8×10^{-4}	1.9×10^{-4} mb
$b/c \rightarrow e$ QCD $\hat{p}_T \in (30, 80)\,GeV/c$	PYTHIA	$10.7\,pb^{-1}$	2.4×10^{-3}	2.4×10^{-4} mb
$b/c \rightarrow e$ QCD $\hat{p}_T \in (80, 170)\,GeV/c$	PYTHIA	$47.6\,pb^{-1}$	1.2×10^{-2}	2.4×10^{-5} mb
γ+jets $\hat{p}_T \in (20, 25)\,GeV/c$	PYTHIA	$3.1\,pb^{-1}$	5.5×10^{-1}	34.1 nb
γ+jets $\hat{p}_T \in (25, 30)\,GeV/c$	PYTHIA	$7.7\,pb^{-1}$	5.7×10^{-1}	15.4 nb
γ+jets $\hat{p}_T \in (30, 35)\,GeV/c$	PYTHIA	$14.9\,pb^{-1}$	5.9×10^{-1}	7.7 nb
γ+jets $\hat{p}_T \in (35, \infty)\,GeV/c$	PYTHIA	$9.3\,pb^{-1}$	6.4×10^{-1}	12.2 nb
W(l=$(e, \mu, \tau)\nu$) +jets	MADGRAPH	$0.17\,fb^{-1}$	-	40 nb
Z(ee) +jets	MADGRAPH	$0.34\,fb^{-1}$	-	1.6 nb
$t\bar{t}$ +jets	MADGRAPH	$6.3\,fb^{-1}$	-	317 pb

Table 5.1: Table summarising the samples used for this analysis. $\mathcal{L}$ denotes the effective sample luminosity, ϵ the generator level pre-selection efficiency and σ the event cross section.

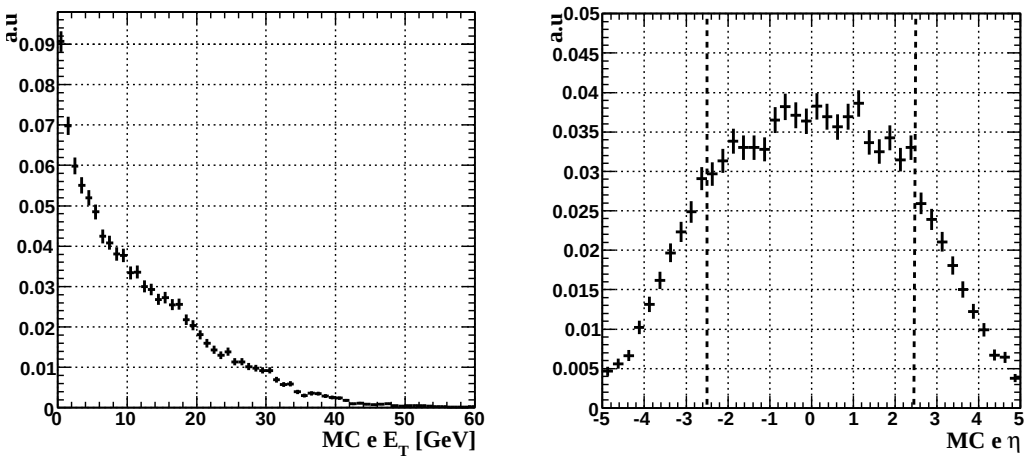

Figure 5.1: Distributions of the generator (MC) electron E_T (left) and η (right), originating from Z→ $\tau\tau$ → τ-jet+e+X events. The bold vertical lines denote a generator level cut placed in this sample which requires that the MC electrons are produced with $|\eta|$ <2.5 which signifies the tracker fiducial region.

5.2 Triggering on Z→ $\tau\tau$ → τ-jet+e+X events

In order to collect an unbiased sample of τ-jets with which to measure the τ-jet identification efficiency, single electron triggers described in Section 3.2.2 . As electrons from τ lepton three body decays are soft as shown in Figure 5.1, this means that the trigger E_T threshold of the electron should be kept low, below 20 GeV. This is possible especially during the initial periods of data taking for luminosity regimes of L= $10^{31}\,cm^{-2}s^{-1}$,$10^{32}\,cm^{-2}s^{-1}$ when the electron trigger bandwidth will be acceptable for E_T <20 GeV.

For all results involving signal events, apart from the generator level pre-selections shown in Figures 5.1 and 5.2, pre-selections using some basic offline criteria for the offline electron and PFTau are placed and are summarised in Table 5.2.

Furthermore for results involving minimum bias events, these had been skimmed using the L1 bit combination of: L1 Single e/γ E_T >8 GeV OR L1 Double e/γ E_T >5 GeV.

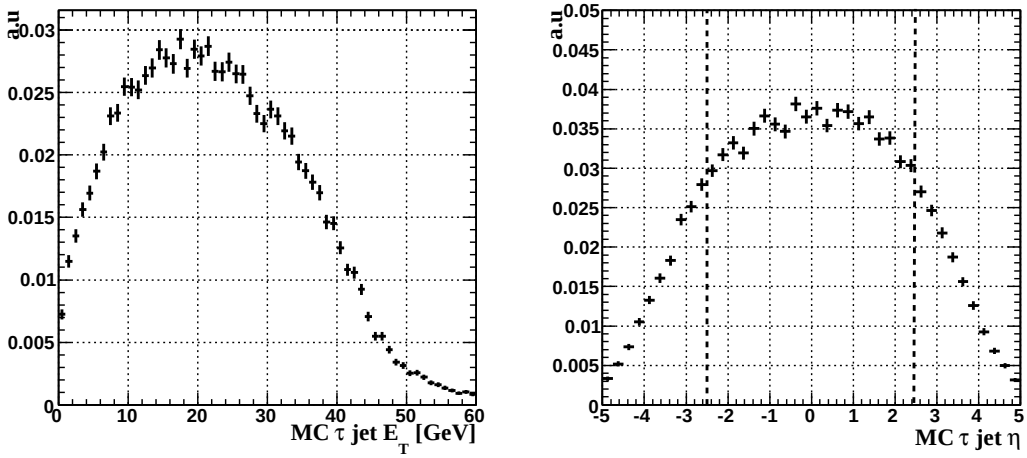

Figure 5.2: Distributions of the generator (MC) τ-jet E_T (left) and η (right), originating from Z→ $\tau\tau$ → τ-jet+e+X events. The bold vertical lines denote a generator level cut placed in this sample which requires that the MC τ-jets are produced with $|\eta|$ <2.5 which signifies the tracker fiducial region.

1. Offline electron isolated in the tracker with no tracks of p_T^{trk} >1.5 GeV/c within an annulus of 0.02< ΔR <0.5.

2. Offline electron satisfies identification criteria of Table 3.3.

3. Offline PFTau with leading track p_T >5 GeV/c.

4. Offline PFTau isolated in the tracker with no tracks of p_T^{trk} >1.0 GeV/c with DR_{iso} <0.5 and DR_{sig} <5.0/E_T and bounded between 0.07<DR_{sig} <0.15.

5. Offline electron and PFTau satisfying the above criteria satisfy $DR_{e\text{PFTau}}$ >0.7 (ensure separate objects).

Table 5.2: Offline object event preselections applied on Z→ $\tau\tau$ → $e + \tau$-jet events.

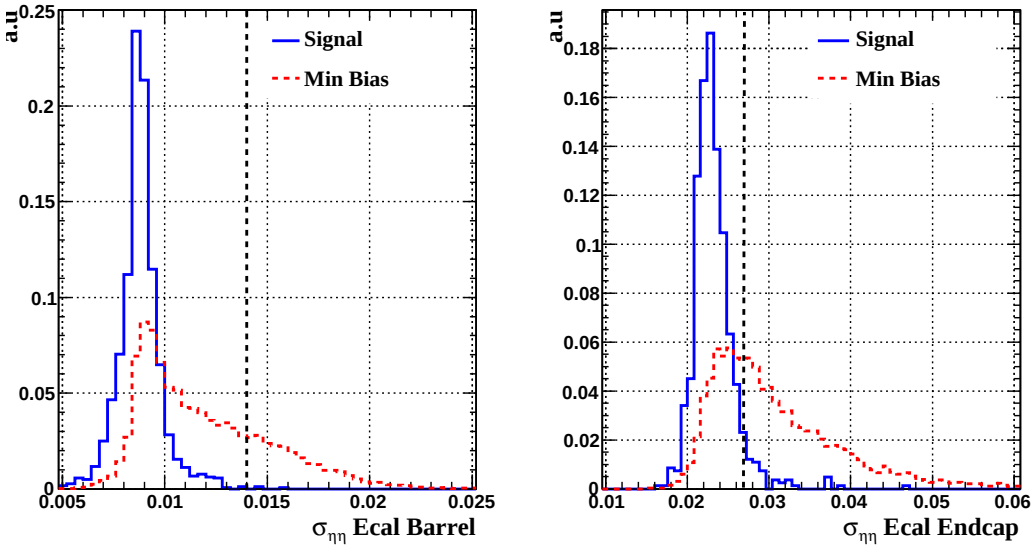

Figure 5.3: Distributions of $\sigma_{\eta\eta}$ at trigger level. The right plot shows the distribution when the super-cluster position lies in the ECAL Barrel and the left plot for the case when the super-cluster position lies in the ECAL Endcap. Solid lines correspond to HLT electrons matching the MC electron in signal events and dashed lines correspond to HLT electrons from L1 EM enriched minimum bias events. The bold vertical line denotes the cut value.

5.2.1 Triggering during L= 10^{31} cm^{-2}s^{-1}

During the L= 10^{31} cm^{-2}s^{-1} regime, a 10 GeV single isolated electron trigger (HLT_IsoEle10_ID_SW_L1I) will be used. In order to keep the rate low, electron identification criteria were used on top of tracker and HCAL isolations. These criteria were a cut on the difference in ϕ and η between the super-cluster position and the track position at the inner most point propagated to the ECAL surface ($\Delta\phi_{\rm in}$,$\Delta\eta_{\rm in}$), and a cluster shape variable measuring the RMS of the electron shower spread in η ($\sigma_{\eta\eta}$). Distributions of these variables for signal and minimum-bias QCD events are show in Figures 5.4 and 5.3. A loose cut was placed on $\sigma_{\eta\eta}$ <1.14 for cases when the super-cluster position is at the ECAL barrel and $\sigma_{\eta\eta}$ <1.27 at the endcaps. Loose cuts were also applied on $\Delta\eta_{\rm in}$ <0.01 and $\Delta\phi_{\rm in}$ <0.06 rad.

In order to collect a large and pure sample of QCD events to estimate their contribution in events passing the selection criteria of the Z→ $\tau\tau$ → τ-jet+e+X analysis, a non isolated version of this 10 GeV electron trigger will also be used

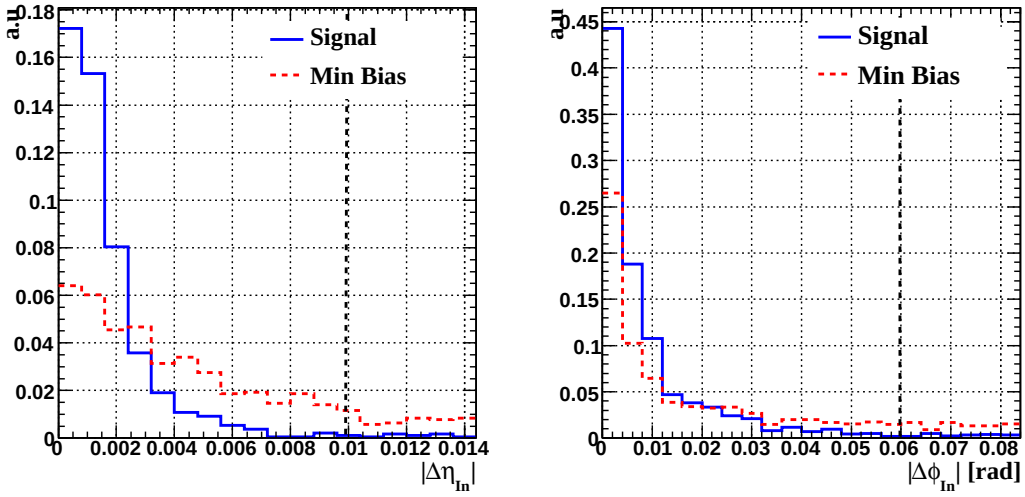

Figure 5.4: Distributions of $\Delta\eta_{\rm in}$ (left) and $\Delta\phi_{\rm in}$ (right) at trigger level. Solid lines correspond to HLT electrons matching the MC electron in signal events and dashed lines correspond to HLT electrons from L1 EM enriched minimum bias events. The bold vertical line denotes the cut value.

(HLT_Ele10_ID_SW_L1R). The same criteria were applied as in HLT_IsoEle10_ID_SW_L1I apart from the Tracker and HCAL isolation. However in order to keep the rate low, a pre-scale will be applied. The choice of the pre-scale was made by balancing trigger bandwidth and collecting sufficient amount of QCD to accurately model its contribution in events passing the selection criteria of the Z→ ττ → τ-jet+e+X analysis. This balance was achieved by pre-scaling the HLT_Ele10_ID_SW_L1R trigger so that it matched the rate of the HLT_IsoEle10_ID_SW_L1I trigger. Tables 5.3 and 5.4 summarise the performance of these single electron triggers on minimum bias QCD events for L= $10^{31}\,{\rm cm}^{-2}{\rm s}^{-1}$. The error in the rate represents the statistical binomial uncertainty on the number of events passing each step, multiplied by the appropriate factors to convert to a rate. The rate of HLT_IsoEle10_ID_SW_L1I is (8.6±0.4) Hz. The rate of HLT_Ele10_ID_SW_L1R including a pre-scale of 4 is (6.7±0.4) Hz. Although a lower pre-scale of 3 could have been chosen so as to match exactly the rate of HLT_IsoEle10_ID_SW_L1I, this higher pre-scale value was considered as a safety margin so that the combined rate of these two 10 GeV Single Electron triggers add less than 10 Hz of rate over the already existing electron triggers of the $10^{31}\,{\rm cm}^{-2}{\rm s}^{-1}$ HLT menu.

HLT_IsoEle10_ID_SW_L1I	Rate (Hz)	Efficiency Rel
Skimmed Total	1120	
L1 Iso $E_T > 8$ GeV	782±4	0.698
L1 Match	695±4	0.889
HLT Electron E_T >10 GeV	381±3	0.548
$\sigma_{\eta\eta}$	231±2	0.607
Hcal Isolation	214±2	0.927
Pixel Match	33.7±0.8	0.158
Loose 1/E-1/P	29.5±0.8	0.873
$\Delta\eta_{in}$, $\Delta\phi_{in}$	19.6±0.6	0.664
Track Isolation	8.6±0.4	0.438

Table 5.3: Minimum Bias Rate of HLT_IsoEle10_ID_SW_L1I trigger for L= $10^{31}\,\mathrm{cm}^{-2}\mathrm{s}^{-1}$. The sample was skimmed using L1 Single EM E_T >8 GeV OR L1 Double EM E_T >5 GeV. Rates are cumulative. The unskimmed Total Rate is 754000 Hz. The error in the rate represents the statistical binomial uncertainty on the number of events passing each step, multiplied by the appropriate factors to convert to a rate. The rate of this trigger is (8.6±0.4) Hz.

HLT_Ele10_ID_SW_L1R	Rate (Hz)	Efficiency Rel
Skimmed Total	1120	
L1 Non Iso E_T >8 GeV	909±4	0.811
Prescale 4 and L1 Match	202±2	0.222
HLT Electron E_T >10 GeV	116±2	0.572
$\sigma_{\eta\eta}$	66.4±1.2	0.575
Pixel Match	12.5±0.5	0.193
Loose 1/E-1/P	10.9±0.5	0.873
$\Delta\eta_{in}$, $\Delta\phi_{in}$	6.7±0.4	0.613

Table 5.4: Minimum Bias Rate of HLT_Ele10_ID_SW_L1R trigger for L= $10^{31}\,\mathrm{cm}^{-2}\mathrm{s}^{-1}$. A prescale of 4 has been applied. The sample was skimmed using L1 Single EM E_T >8 GeV OR L1 Double EM E_T >5 GeV. The Unskimmed Total Rate is 754000 Hz. The error in the rate represents the statistical binomial uncertainty on the number of events passing each step, multiplied by the appropriate factors to convert to a rate. The rate of this trigger including the prescale is (6.7±0.4) Hz.

HLT_Ele10_ID_SW_L1R	Efficiency Cumulative	Efficiency Rel
L1 Non Iso E_T >8 GeV	0.984±0.019	0.984
Prescale 4 and L1 Match	0.252±0.010	0.256
HLT Electron E_T >10 GeV	0.251±0.010	0.997
$\sigma_{\eta\eta}$	0.249±0.010	0.994
Pixel Match	0.229±0.009	0.918
Loose 1/E-1/P	0.222±0.009	0.970
$\Delta\eta_{in}$, $\Delta\phi_{in}$	0.212±0.009	0.955

Table 5.5: Signal efficiency of the HLT_Ele10_ID_SW_L1R trigger for L= $10^{31}\,cm^{-2}s^{-1}$. A prescale of 4 has been applied. The sample was preselected using the criteria described in Table 5.2 including at offline electron E_T >12 GeV cut. The errors represent the statistical binomial uncertainty. The signal efficiency is (0.212±0.009).

HLT_IsoEle10_ID_SW_L1I	Efficiency Cumulative	Efficiency Rel
L1 Iso E_T >8 GeV	0.935± 0.019	0.935
L1 Match	0.935± 0.019	1.000
HLT Electron E_T >10 GeV	0.930± 0.019	0.995
$\sigma_{\eta\eta}$	0.923± 0.019	0.992
Hcal Isolation	0.920± 0.019	0.997
Pixel Match	0.834± 0.018	0.907
Loose 1/E-1/P	0.802± 0.018	0.961
$\Delta\eta_{in}$, $\Delta\phi_{in}$	0.773± 0.018	0.964
Track Isolation	0.765± 0.018	0.990

Table 5.6: Signal efficiency of the HLT_IsoEle10_ID_SW_L1R trigger for L= $10^{31}\,cm^{-2}s^{-1}$. The sample was preselected using the criteria described in Table 5.2 including at offline electron E_T >12 GeV cut. The errors represent the statistical binomial uncertainty. The signal efficiency is (0.765±0.018).

The performance of HLT_Ele10_ID_SW_L1R and HLT_IsoEle10_ID_SW_L1I triggers on signal events satisfying the criteria of Table 5.2 with the offline electron E_T >12 GeV is summarised in Tables 5.6 and 5.5. The errors represent the statistical binomial uncertainty. This offline threshold was chosen to ensure that events are selected on the plateau of the HLT turn on curve. The main drop in signal efficiency occurs due to the tighter HLT electron pixel matching and (1/E-1/P) criteria which were not applied in this generic offline electron definition. Furthermore the large drop in the HLT efficiency of the HLT_Ele10_ID_SW_L1R trigger was due to the prescale of 4 applied after L1.

HLT_IsoEle15_L1I	Rate (Hz)	Efficiency Rel
Total	1.45e+05	
L1 Iso E_T >12 GeV	1700±10	0.012
L1 Match	1580±10	0.930
HLT Electron E_T >15 GeV	770±6	0.490
Hcal Isolation	672±6	0.869
Pixel Match	69.7±1.6	0.104
Loose 1/E-1/P	60.6±1.5	0.870
Track Isolation	20.5±0.8	0.339

Table 5.7: Rate of the HLT_IsoEle15_L1I trigger rate in QCD $\hat{p}_T$ >15 GeV/c for L= $10^{32}\,cm^{-2}s^{-1}$. The error in the rate represents the statistical binomial uncertainty on the number of events passing each step, multiplied by the appropriate factors to convert to a rate.

5.2.2 Triggering during L= $10^{32}\,\mathbf{cm^{-2}s^{-1}}$

For the L= $10^{32}\,cm^{-2}s^{-1}$ regime, currently the only single isolated electron trigger available in the HLT menu has an E_T >15 GeV (HLT_IsoEle15_L1I). Therefore this is the trigger that is used in this study to select Z$\rightarrow \tau\tau \rightarrow \tau$-jet+e+X events. Table 5.7 shows the rate for every selection of this trigger using QCD with $\hat{p}_T$ >15 GeV/c.

The corresponding efficiency table for Signal events satisfying the criteria of Table 5.2 with the offline electron E_T >17 GeV is shown in Table 5.8. The main drop in Signal efficiency occurs due to the tighter HLT electron pixel matching and (1/E-1/P) criteria which were not applied in this generic offline electron definition. Figure 5.5 shows the L1 and L1+HLT efficiencies of this trigger as a function of the offline reconstructed electron E_T and η. The efficiency with respect to η requires E_T >15 GeV. The drop in efficiency of the HLT_IsoEle15_L1I trigger between $1.2 < \eta < 1.8$ is mainly due to the increase of tracking material, shown in Figure 2.4 which causes the electron to radiate energy which fails the calorimetric isolation criteria of the L1 isolated e/γ trigger or the pixel matching criteria of the HLT.

5.3 Electron selections

The main goal of these electron selections is to reduce the large QCD background without the requirement of harsh subsequent τ-jet selections.

HLT_IsoEle15_L1I	Efficiency Cumulative	Efficiency Rel
L1 Iso E_T >12 GeV	0.890± 0.028	0.890
L1 Match	0.890± 0.028	1.000
HLT Electron E_T >15 GeV	0.883± 0.028	0.990
Hcal Isolation	0.877± 0.028	0.993
Pixel Match	0.756± 0.026	0.862
Loose 1/E-1/P	0.703± 0.025	0.930
Track Isolation	0.693± 0.025	0.985

Table 5.8: Signal efficiency of the HLT_IsoEle15_L1I trigger for L= $10^{32}\,cm^{-2}s^{-1}$. The sample was preselected using the criteria described in Table 5.2 including an offline electron E_T >17 GeV cut. The errors represent the statistical binomial uncertainty. The signal efficiency is (0.693±0.025).

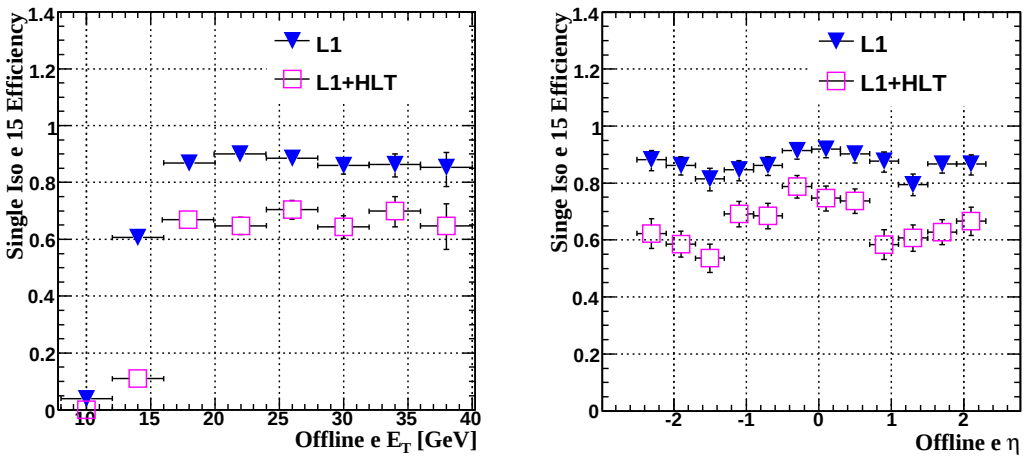

Figure 5.5: L1 and L1+HLT efficiencies of HLT_IsoEle15_L1I as a function of the offline reconstructed electron E_T (left) and η (right). The efficiency w.r.t η requires E_T >16 GeV.

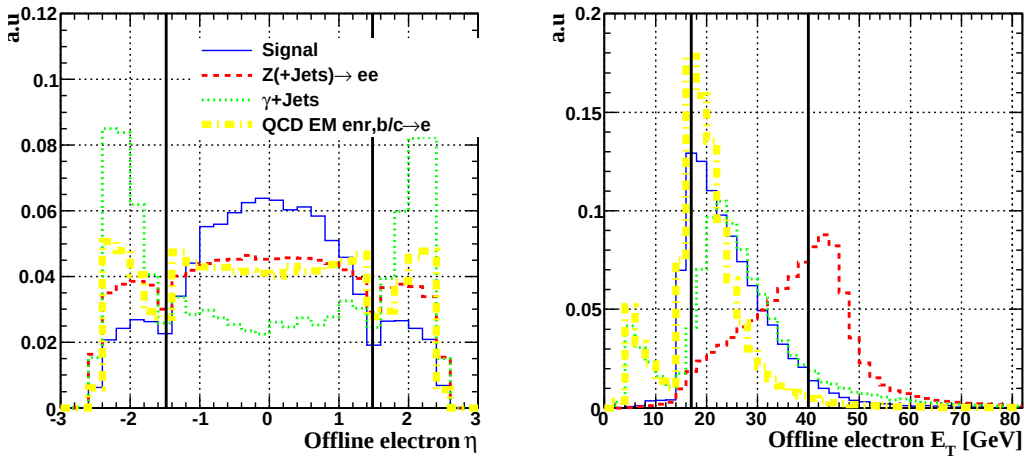

Figure 5.6: Left: η distribution of offline electrons matching within $\Delta R < 0.1$ the HLT electron firing the HLT_IsoEle15_L1I trigger. Right: E_T distribution of offline electrons matching within $\Delta R < 0.1$ the HLT electron firing the HLT_IsoEle15_L1I trigger. The dashed distribution corresponds to Z(+jets)$\rightarrow ee$ events, the dotted distribution corresponds to γ+jets events, the dashed-dotted distribution corresponds to QCD EM enriched and $b/c \rightarrow e$ events. The solid line corresponds to signal events where the offline electron matches the MC electron in the event within $\Delta R < 0.1$. The bold vertical lines indicate the positions the cuts are placed. The electron distribution of W+jets events is similar to the Z+jets case.

5.3.1 Kinematic Selections

For events passing the HLT_IsoEle15_L1I trigger, a further set of kinematic criteria are applied to the offline electron, described in Section 3.2.1, matching in $\Delta R < 0.1$ the HLT electron. Firstly a tighter E_T >17 GeV cut is placed to ensure we are sitting at the plateau of the HLT electron turn on distribution as shown in Figure 5.5. Moreover in order to reduce the contribution of high E_T electrons originating from Z(W) decays an upper cut of $E_T < 40$ GeV is placed as suggested by the right plot of Figure 5.6. The second peak below 15 GeV for the QCD and γ+jets E_T distributions corresponds to events containing a second electron candidate (fake or prompt) with E_T below the trigger threshold. Finally as the main goal of this analysis is to collect a pure sample of Z$\rightarrow \tau\tau \rightarrow \tau$-jet+e events without applying stringent selection criteria on the τ-jets in order to obtain an unbiased collection for further studies, offline electrons are required to have $|\eta| < 1.479$ which suppresses QCD and γ+jets events as shown in the left plot of Figure 5.6.

5.3.2 The γ(+jets)$\rightarrow ee$ background

High E_T (>15 GeV) isolated photons arising mainly from γ+jets events can convert to a pair of electrons in the tracker, giving rise to a well isolated electron passing all the electron identification criteria. In order to reduce the contribution from such events and generally cases where the electron originated from a photon conversion, algorithms have been implemented which search and veto such electrons. The standard conversion finding algorithm described in [59] begins by looking for an ECAL super-cluster which is assumed to contain the bulk of the converted photon energy. Tracks are then reconstructed using the Kalman or GSF based fitting by propagating first inwards from the first tracker layer and then outwards, from the inner most compatible hit of the inwards reconstructed track. All pairs of oppositely charged tracks satisfying the χ^2 and N_{hits} criteria are retained, and the track pair satisfying further selections such as the invariant mass are assumed to originate from a converted photon [59].

In events which satisfy isolated electron triggers, the conversion tends to be highly asymmetric as the conversion electron which fired the trigger is not allowed to have any track with p_T >1 GeV/c within an annulus $0.02 < \Delta R < 0.2$. The left plot of Figure 5.7 shows the p_T of the simulation level electron tracks originating from a photon conversion, when one of these tracks matches (in ΔR) the electron which fired the HLT and has p_T >18 GeV and $|\eta| < 1.479$. A clear asymmetry is seen in the p_T of such electrons with the soft electron having a p_T ≤1 GeV/c. Furthermore the fact that reconstructed electrons are required to have hits in at least two pixel layers, means that the conversion must have occurred at or before the second pixel layer as shown in the right plot of Figure 5.7 where the two first pixel layers at ≈4 and ≈7 cm are clearly visible. The conversions at ≈3 cm are most likely due to the exterior shell of the pixel barrel. Therefore electrons with p_T ≤1 GeV/c originating at the pixel layers will loose a large fraction of their energy while crossing the tracker and therefore will not leave hits in the outer most tracker layers compatible with the super cluster seed. Thus the standard conversion finding algorithm will not identify a conversion vertex.

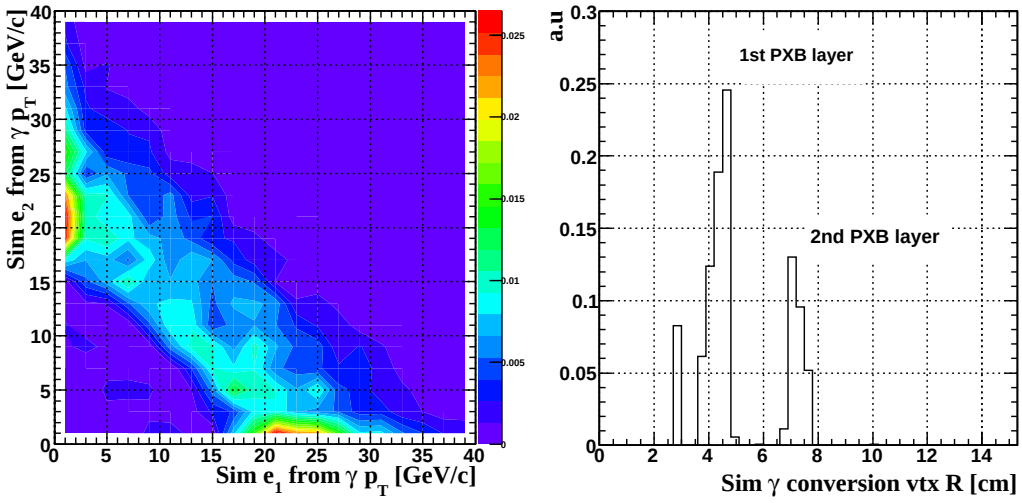

Figure 5.7: Left: Distribution of the p_T's of the electron tracks at simulation level which originated from a photon conversion plotted against each-other in events firing the single isolated electron HLT and contain an offline reconstructed electron with E_T >18 GeV and $|\eta|$ <1.479, for γ+Jet events. Right: The photon conversion position radius at simulation level for events firing the single isolated electron HLT and contain an offline reconstructed electron with E_T >18 GeV and $|\eta|$ <1.479, for γ+Jet events. For both plots the simulation level electron has been matched to the offline reconstructed electron.

Therefore in order to identify and remove electrons originating from a photon conversion in events which fire the isolated electron HLT, a dedicated basic algorithm was developed. It relied on comparing the inner most hit position and momentum between the well reconstructed offline electron and all tracks with p_T >0.3 GeV/c. As photons are massless, the opening angle between the two electrons should be small. Due to the bending of the tracks in the (r-ϕ) plane from to the magnetic field, a cut was placed on the difference of the slope in the (r-z) plane parametrised as $\cot\theta$ where θ is the polar angle as measured from the z-axis. The left plot of Figure 5.8 shows the distribution of $\Delta\cot\theta_{\rm in}$ between the inner most track momentum of the reconstructed electron track and all reconstructed tracks whose inner most track hit positions are separated by $0.01 < \Delta R_{\rm in} < 0.3$. A clear excess of tracks with $\Delta\cot\theta_{\rm in} = 0$ is seen in γ+jets events. The small excess at 0 in signal events is due to the inefficiency of removing the signature of the GSF electron track from the general track collection using the $\Delta R_{\rm in} > 0.01$ requirement. A cut was thus placed on the number of reconstructed tracks with $p_T > 0.3$ GeV/c which have $|\Delta\cot\theta_{\rm in}| < 0.045$

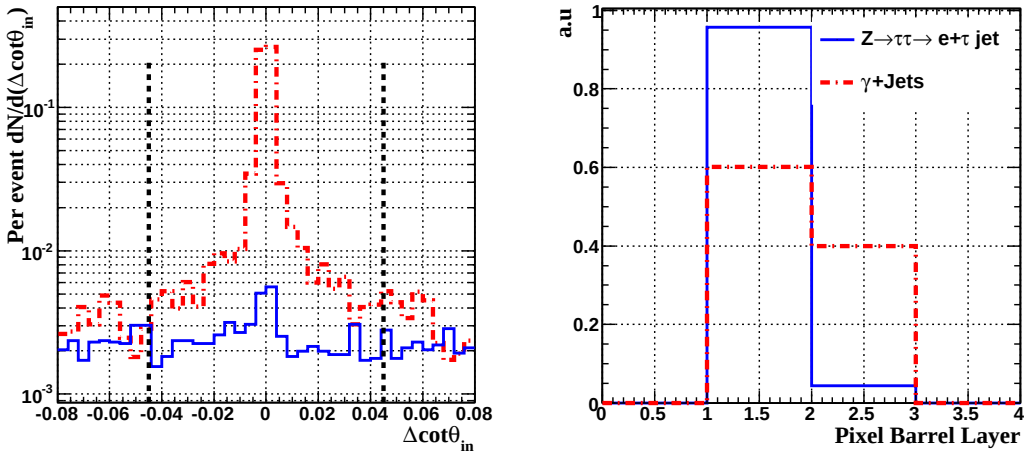

Figure 5.8: Left: Distribution of $\Delta\cot\theta_{\rm in}$ in events firing the single isolated electron HLT and contain an offline electron with E_T >18 GeV and $|\eta|$ <1.479, for γ+Jet events (dashed) and signal events (solid). Right: Innermost pixel barrel layer hit of the reconstructed electron in events firing the single isolated electron HLT and contain an offline electron with E_T >18 GeV and $|\eta|$ <1.479 and satisfies the $\Delta\cot\theta_{\rm in}$ selection, for γ+Jet events (dashed) and signal events (solid).

and the inner most track hits were separated by $\Delta R_{\rm in}$ <0.3 ($N_{\rm conv}$). $N_{\rm conv}$ was required to be either 0 or 1 in order to account for the GSF reconstructed electron track appearing in the general track collection of CMS.

In order to further reduce the contribution of electrons originating from converted photons, reconstructed electron tracks were required to leave a hit in the first pixel layer. This suppresses electrons within $|\eta|$ <1.479 from photon conversions by 60% while keeping a high efficiency of 96% on electrons originating from the τ decay as shown in the right plot of Figure 5.8.

The per event performance of both selections is summarised in Table 5.9 for signal and γ+jets events giving an efficiency of 91% in signal events and 19% in γ+jets events for events firing the single isolated electron HLT and containing an offline electron with E_T >18 GeV and $|\eta|$ <1.479

5.3.3 Isolations

Three types of isolation were applied to the electron. Isolation in the Tracker, in the ECAL and in the HCAL as described in Section 3.2.1. In order to reduce

Cut	Signal	γ+jets
N_{conv}=0 or 1	95%	35%
1st PXB Layer	91%	19%

Table 5.9: Table summarising the performance of the photon conversion rejection criteria described in the text for events firing the single isolated electron HLT and containing an offline electron with E_T >18 GeV and $|\eta|$ <1.479. Efficiencies are cumulative.

significantly the QCD background without having to place stringent selection criteria on the τ-jets, tight electron isolation criteria were required. Furthermore in order to be able to obtain the efficiency of the electron selections on real electrons from Z$\rightarrow$ *ee* studies, only absolute isolation variables were considered since no corrections would be needed due to the different electron kinematic distribution of electrons from τ-lepton decays. In particular Σp_T^{Trk}, ΣE_T^{ECAL}, ΣE^{HCAL} where p_T^{trk}, E_T^{ECAL}, E^{HCAL} denote the p_T, E_T and E of the tracks, ECAL crystals and HCAL towers respectively within their corresponding isolation annuli were used.

Figure 5.9 shows the performance of the Track isolation variable Σp_T^{Trk} starting at 0.3 GeV/c in steps of 0.3 GeV/c for various isolation annuli between $0.015 < \Delta R < [0.3, 0.9]$ and with $p_T^{Trk} > 0.3$ GeV/c. The left plot shows the performance of Σp_T^{Trk} as a function of the efficiency for signal electrons originating from Z$\rightarrow \tau\tau \rightarrow \tau$-jet+e decays (x-axis) and of the efficiency on QCD jets in both the EM and electron enriched QCD samples (y-axis). The right plot shows the performance of Σp_T^{Trk} as a function of the number of signal events for 100 pb^{-1} of integrated luminosity (x-axis) and of the number of signal over Background QCD, EM and electron enriched events (S/B). Events are required to satisfy the HLT_IsoEle15_L1I trigger and the kinematic criteria of Section 5.3.1. A cut at $\Sigma p_T^{Trk} < 0.9$ GeV/c with $0.015 < \Delta R < 0.7$ and $p_T^{Trk} > 0.3$ GeV/c was chosen giving a signal efficiency of 52.0% and a QCD efficiency of 11.5%. Figure 5.10 shows the distribution of this variable with the chosen parameters for signal (Solid) and both EM enriched QCD (Left-Dashed) and QCD $b/c \rightarrow e$ (Right-Dashed) events. The vertical line denotes the position of the cut.

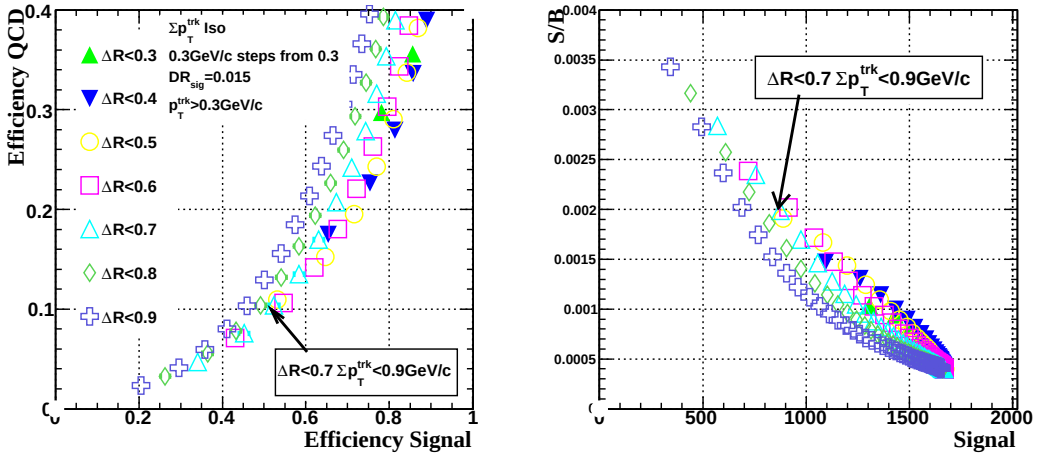

Figure 5.9: Track Isolation variable Σp_T^{Trk} performance on signal and QCD electrons for various isolation cone sizes. The isolation variable varies in steps of 0.3 GeV/c starting from 0.3 GeV/c. The rest of the isolation parameters are described in the text. Electrons from signal events have been matched to the MC electron with $\Delta R < 0.1$. For both QCD and signal, only events where the HLT_IsoEle15_L1I trigger has fired, contain an offline electron with E_T >18 GeV and $|\eta| < 1.5$ were considered.

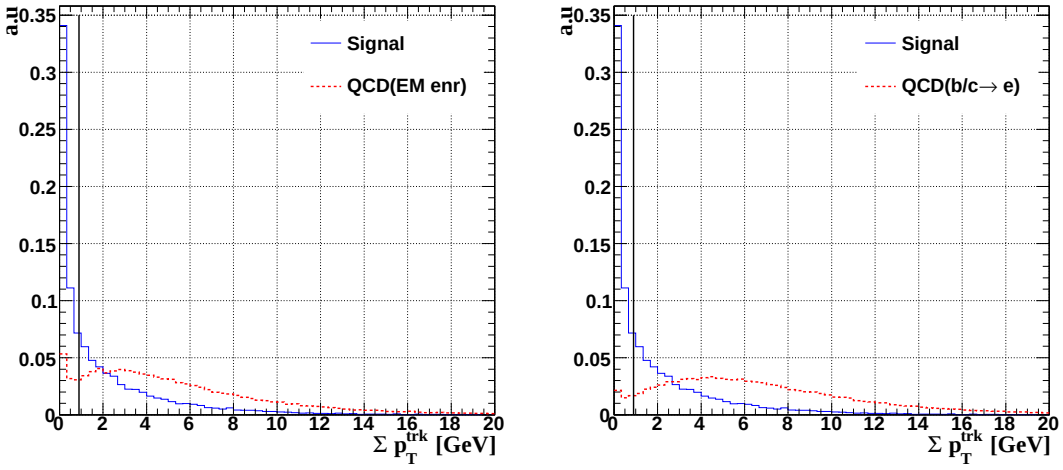

Figure 5.10: Distribution of the electron Track isolation variable $\Sigma p_T^{Trk\,iso}$ for signal (blue) and EM enriched QCD (left) or BCtoE QCD (right). Electrons from signal events have been matched to the MC electron with $\Delta R < 0.1$. For both QCD and signal, only events where the single isolated electron trigger has fired , contain an offline electron with E_T >17 GeV and $|\eta| < 1.5$ were considered.

Figure 5.11 shows the performance of the ECAL isolation variable ΣE_T^{ECAL} starting at 0.25 GeV in steps of 0.25 GeV for various isolation annuli between $0.045 < \Delta R < [0.3, 0.9]$ and with $E_T^{ECAL} > 0.12$ GeV and a strip width $\Delta\eta = 0.02$. The left plot shows the performance of ΣE_T^{ECAL} as a function of the efficiency for signal electrons originating from $Z \rightarrow \tau\tau \rightarrow \tau$-jet+e decays (x-axis) and of the efficiency on QCD jets in both the EM and electron enriched QCD samples (y-axis). The right plot shows the performance of ΣE_T^{ECAL} as a function of the number of signal events for 100 pb^{-1} of integrated luminosity (x-axis) and of the number of Signal over Background QCD, EM and electron enriched events (S/B). Events are required to satisfy the HLT_IsoEle15_L1I trigger, the kinematic criteria of Section 5.3.1 and the Track isolation of Figure 5.9. A cut at $\Sigma E_T^{ECAL} < 1.0$ GeV/c with $0.045 < \Delta R < 0.7$, $E_T^{ECAL} > 0.25$ GeV/c and strip width$\Delta\eta = 0.02$ was chosen giving a signal efficiency of 68.4% and a QCD efficiency of 17.1%. Figure 5.12 shows the distribution of this variable with the chosen parameters for signal (Solid) and both EM enriched QCD (Left-Dashed) and QCD $b/c \rightarrow e$ (Right-Dashed) events. The vertical line denotes the position of the cut.

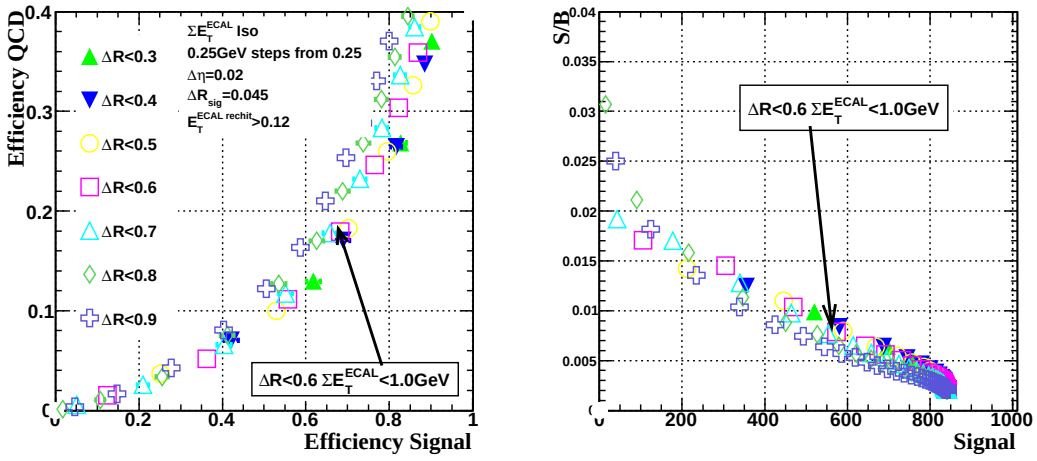

Figure 5.11: ECAL Isolation variable $\Sigma E_T^{ECAL\,iso}$ performance on signal and QCD electrons for various isolation cone sizes. The isolation variable varies in steps of 0.25GeV/c starting from 0.25GeV/c. The rest of the isolation parameters are described in the text. Electrons from signal events have been matched to the MC electron with $\Delta R < 0.1$. For both QCD and signal, only events where the single isolated electron trigger has fired, contain an offline electron with E_T >17 GeV and $|\eta| < 1.5$ which satisfy the offline Track isolation criteria were considered.

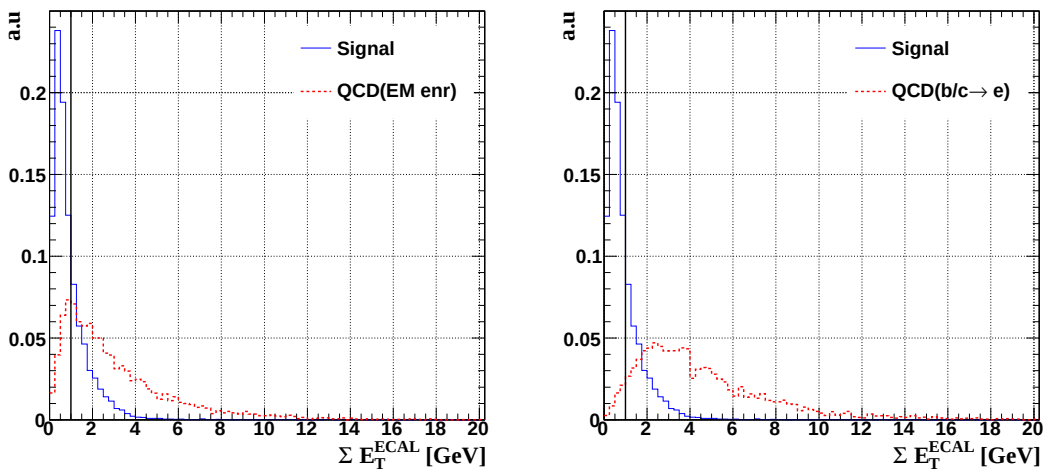

Figure 5.12: Distribution of the electron ECAL isolation variable $\Sigma E_T^{ECAL\,iso}$ for signal (blue) and EM enriched QCD (left) or $b/c \rightarrow e$ QCD (right). Electrons from signal events have been matched to the MC electron with $\Delta R < 0.1$. For both QCD and signal, only events where the single isolated electron trigger has fired , contain an offline electron with $E_T > 17\,GeV$ and $|\eta| < 1.5$ which satisfy the offline Track isolation criteria were considered.

Figure 5.13 shows the performance of the HCAL isolation variable ΣE^{HCAL} starting at 0.5 GeV in steps of 0.5 GeV for various isolation cones between $0 < \Delta R < [0.3, 0.9]$. Because of the HCAL performance during the Cosmic Run at Zero Tesla analysis discussed in Chapter 4, a loose HCAL isolation was considered in order to reduce the dependance of this analysis on the effects of HCAL noise. The left plot shows the performance of ΣE^{HCAL} as a function of the efficiency for signal electrons originating from $Z \rightarrow \tau\tau \rightarrow \tau$-jet+e decays (x-axis) and of the efficiency on QCD jets in both the EM and electron enriched QCD samples (y-axis). The right plot shows the performance of ΣE^{HCAL} as a function of the number of signal events for $100\,pb^{-1}$ of integrated luminosity (x-axis) and of the number of signal over Background QCD, EM and electron enriched events (S/B). Events are required to satisfy the HLT_IsoEle15_L1I trigger, the kinematic criteria of Section 5.3.1 and the Track and ECAL isolation of Figures 5.9 and 5.11. A cut at $\Sigma E^{HCAL} < 1.5\,GeV/c$ with $0 < \Delta R < 0.3$ was chosen giving a signal efficiency of 99.3% and a QCD efficiency of 79.2%. Figure 5.14 shows the distribution of this variable with the chosen parameters for signal (Solid) and both EM enriched QCD (Left-Dashed) and QCD $b/c \rightarrow e$ (Right-Dashed) events. The vertical line denotes the position of the cut.

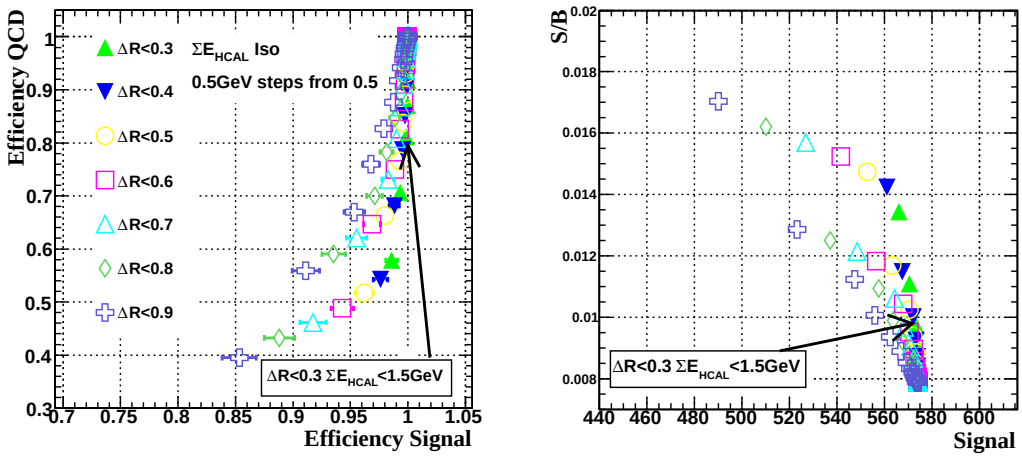

Figure 5.13: HCAL Isolation variable $\Sigma E^{\mathrm{HCAL\,iso}}$ performance on signal and QCD electrons for various isolation cone sizes. The isolation variable varies in steps of 0.5GeV/c starting from 0.5GeV/c. The rest of the isolation parameters are described in the text. Electrons from signal events have been matched to the MC electron with $\Delta R < 0.1$. For both QCD and signal, only events where the single isolated electron trigger has fired, contain an offline electron with E_T >17 GeV and $|\eta| < 1.5$ which satisfy the offline Track and ECAL isolation criteria were considered.

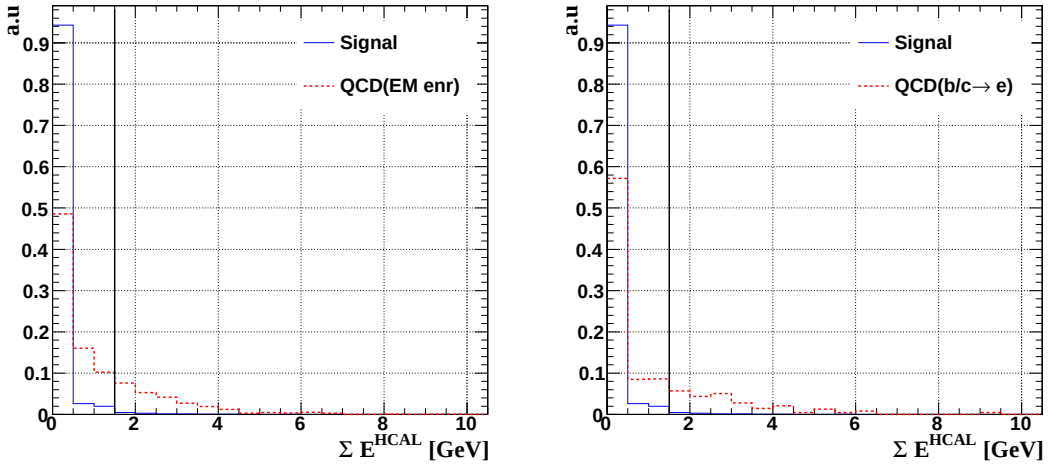

Figure 5.14: Distribution of the electron HCAL isolation variable $\Sigma E^{\mathrm{HCAL\,iso}}$ for signal (blue) and EM enriched QCD (left) or $b/c \rightarrow e$ QCD (right). Electrons from signal events have been matched to the MC electron with $\Delta R < 0.1$. For both QCD and signal, only events where the single isolated electron trigger has fired , contain an offline electron with E_T >17 GeV and $|\eta| < 1.5$ which satisfy the offline ECAL and Track isolation criteria were considered.

5.3.4 Identification

In order to further reduce the contribution of QCD jets faking electrons a set of electron identification criteria as described in Section 3.2.1 were applied. Figures 5.15, 5.16, 5.17, 5.18, 5.19 show the distributions of E/P, $\Delta\phi_{\rm in}$, $\Delta\eta_{\rm in}$, H/E and $\mathrm{E2}\times5/\mathrm{E5}\times5$ Vs $\mathrm{E1}\times5/\mathrm{E5}\times5$ respectively in signal (Solid/Blue) and both EM enriched QCD (Left-Dashed/Red) and $b/c \rightarrow e$ QCD (Right-Dashed/Red) for events which satisfy HLT_IsoEle15_L1I trigger, the kinematic criteria of Section 5.3.1 and the isolation criteria of Section 5.3.3. As expected the identification variable distributions for reconstructed electrons in $b/c \rightarrow e$ QCD events are more like events containing a signal electron, compared to the EM enriched QCD case since the jets from $b/c \rightarrow e$ always contain a prompt electron originating from decays of b/c quarks. The vertical bold lines denote the position of the cut. Table 5.10 summarises the values of the selections and the efficiencies in signal, EM enriched and $b/c \rightarrow e$ QCD events. An efficiency of 79.8% is obtained on signal events and 6.0% in combined EM enriched and $b/c \rightarrow e$ QCD events w.r.t. events which satisfy the electron trigger, kinematic, γ conversion rejection and isolation criteria.

The S/B, with B representing the total number of QCD events (EM enriched and $b/c \rightarrow e$) improves from 5.5×10^{-4} before electron isolation and identification is applied, to 1.3×10^{-1} after electron isolation and identification criteria are applied, with a signal efficiency of 28.2% w.r.t. events which satisfy the electron trigger, kinematic, γ conversion rejection criteria.

Selection	Signal	EM enr QCD	$b/c \to e$ QCD	Combined QCD
$\Sigma p_T^{Trk} < 0.9$	52.0%	12.8%	5.7%	11.5%
$\Sigma E_T^{ECAL} < 1.0$	68.4%	18.3%	5.1%	17.1%
$\Sigma E^{HCAL} < 1.5$	99.3%	79.2%	79.8%	79.2%
H/E<0.015, 0.9<E/P<1.2				
$\Delta\eta_{in} < 0.0092$, $\Delta\phi_{in} < 0.02$				
$\frac{E2\times5}{E5\times5} > 0.95 \frac{E1\times5}{E5\times5} < 0.85$ OR	79.8%	4.7%	52.3%	6.0%
$\frac{E2\times5}{E5\times5} > 0.92 \frac{E1\times5}{E5\times5} > 0.85$				
$\frac{E2\times5}{E5\times5} < 0.99$				
Total	28.2%	0.09%	0.1%	0.09%

Table 5.10: Table summarising the selection and performance of the Electron Isolation and Identification on signal, EM enriched and $b/c \to e$ QCD events. Efficiencies are relative to the previous selection criterion.

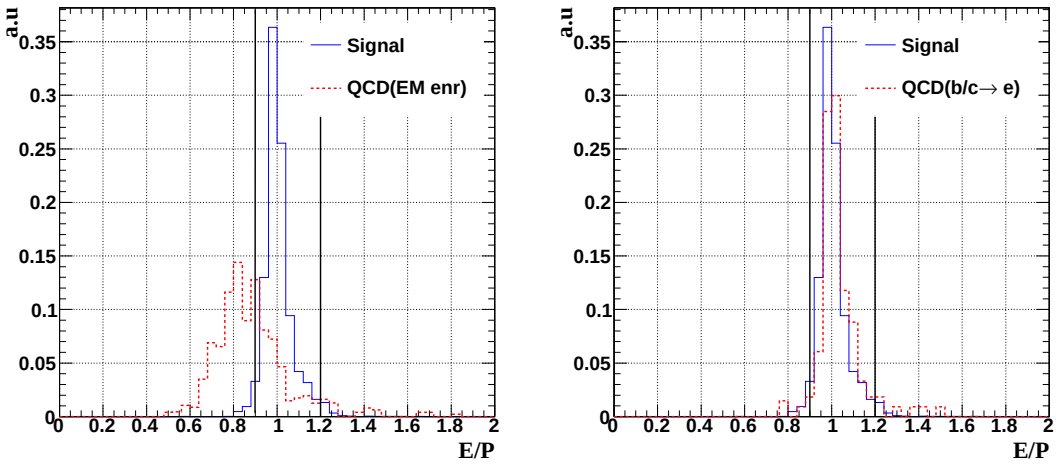

Figure 5.15: Distribution of the electron E/P id variable for signal (blue) and EM enriched QCD (left) or $b/c \to e$ QCD (right). Electrons from signal events have been matched to the MC electron with $\Delta R < 0.1$. For both QCD and signal, only events where the single isolated electron trigger has fired , contain an offline electron with E_T >17 GeV and $|\eta| < 1.5$ which satisfies all the offline isolation criteria were considered.

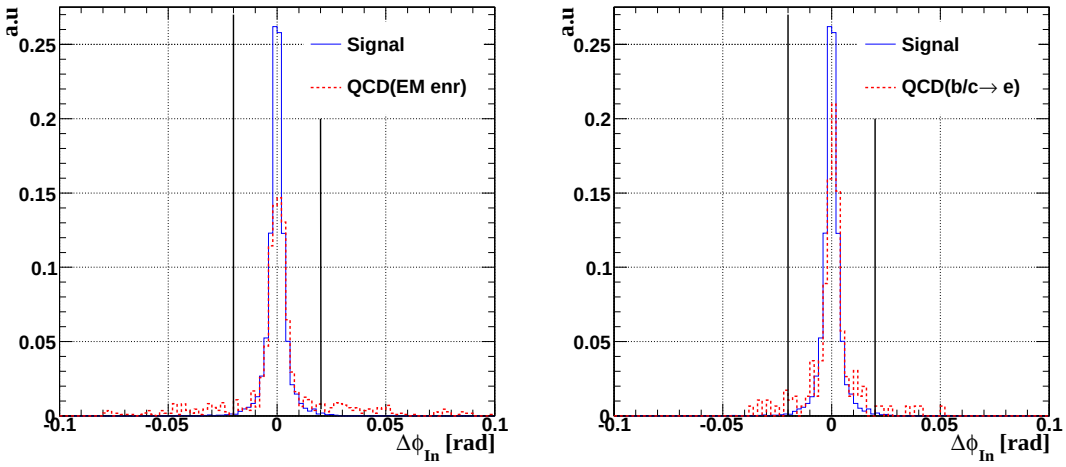

Figure 5.16: Distribution of the electron $\Delta\phi$ id variable for signal (blue) and EM enriched QCD (left) or $b/c \rightarrow e$ QCD (right). Electrons from signal events have been matched to the MC electron with $\Delta R < 0.1$. For both QCD and signal, only events where the single isolated electron trigger has fired , contain an offline electron with E_T >17 GeV and $|\eta| < 1.5$ which satisfies all the offline isolation criteria were considered.

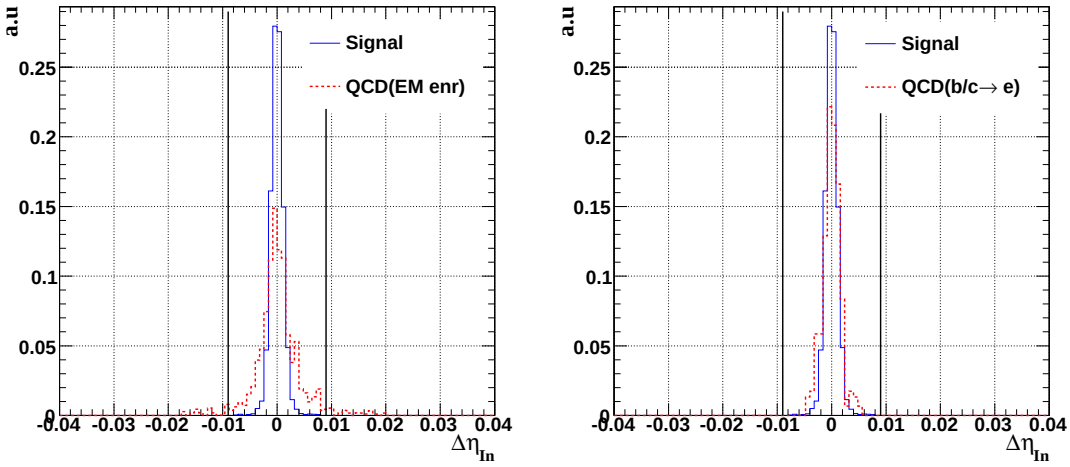

Figure 5.17: Distribution of the electron $\Delta\eta$ id variable for signal (blue) and EM enriched QCD (left) or $b/c \rightarrow e$ QCD (right). Electrons from signal events have been matched to the MC electron with $\Delta R < 0.1$. For both QCD and signal, only events where the single isolated electron trigger has fired , contain an offline electron with E_T >17 GeV and $|\eta| < 1.5$ which satisfies all the offline isolation criteria were considered.

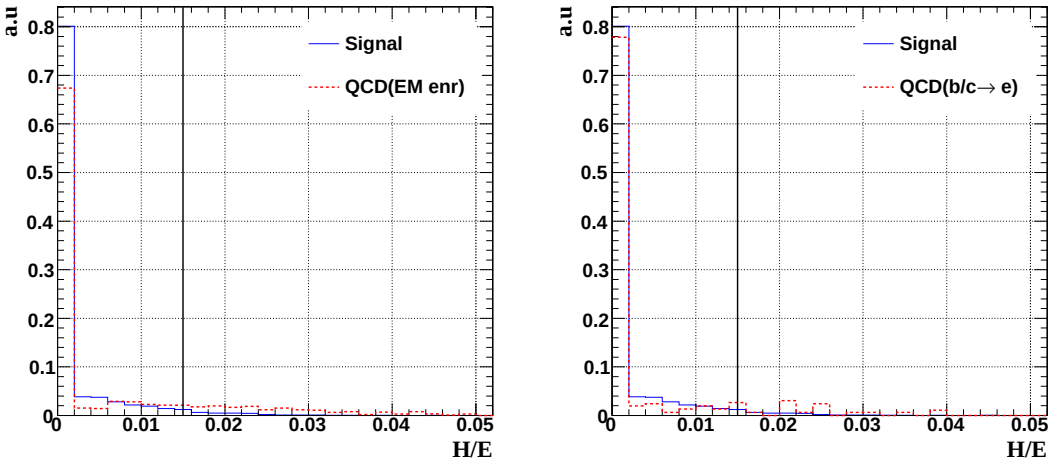

Figure 5.18: Distribution of the electron H/E id variable for signal (blue) and EM enriched QCD (left) or $b/c \rightarrow e$ QCD (right). Electrons from signal events have been matched to the MC electron with $\Delta R < 0.1$. For both QCD and signal, only events where the single isolated electron trigger has fired , contain an offline electron with E_T >17 GeV and $|\eta| < 1.5$ which satisfies all the offline isolation criteria were considered.

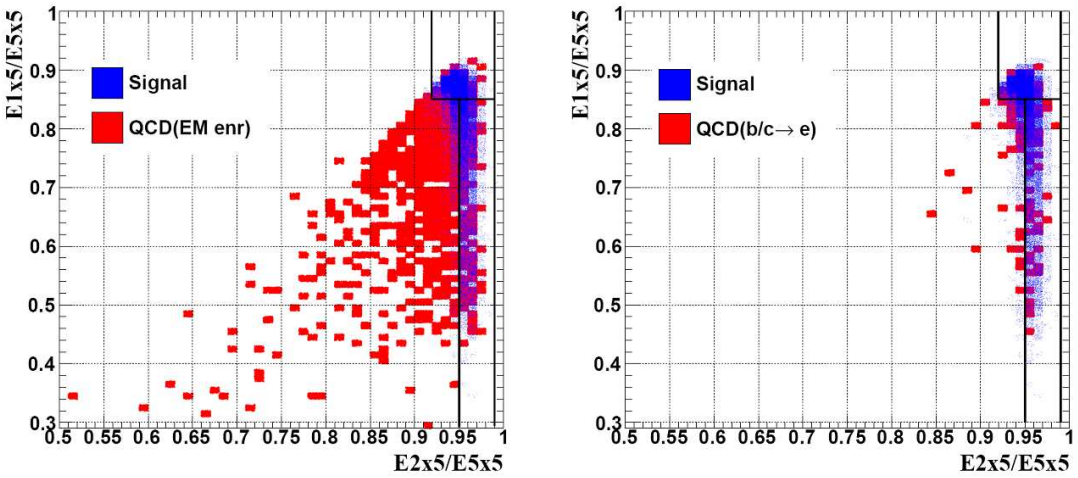

Figure 5.19: Distribution of the electron (E2x5/E5x5 vs E1x5/E5x5) id variable for signal (blue) and EM enriched QCD (left) or $b/c \rightarrow e$ QCD (right). Electrons from signal events have been matched to the MC electron with $\Delta R < 0.1$. For both QCD and signal, only events where the single isolated electron trigger has fired , contain an offline electron with E_T >17 GeV and $|\eta| < 1.5$ which satisfies all the offline isolation criteria were considered. The area enclosed between the bold lines denotes the selection.

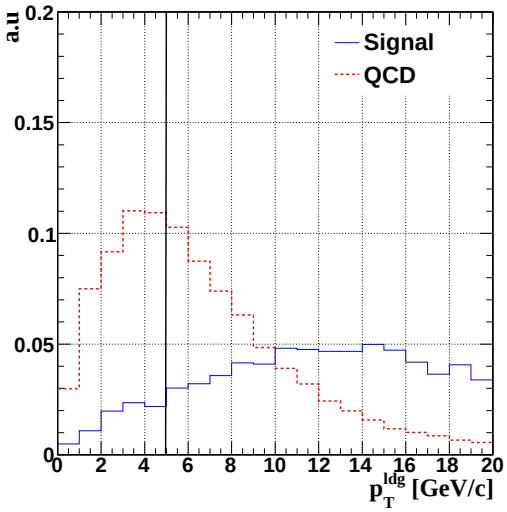

Figure 5.20: Distribution of the PF leading charged hadron p_T within $\Delta R_m = 0.1$ for PFTaus with E_T >15 GeV matching the MC τ-jet in signal events with $\Delta R < 0.2$ (solid-blue), and in QCD events where no matching is applied (dashed-red).

5.4 PFTau selections

5.4.1 Introduction

Once the electron selections of Section 5.3 are satisfied, the PFTau reconstruction and selections follow as outlined in Section 3.3.1. These selections are tuned to minimise any biases on the "core" structure (dynamics of hadronic τ decay stable products).

All PFTaus, which at this point are simply iterative cone jets of size $\Delta R = 0.5$ made up of PF particles, are required to have an $E_T > 15$ GeV lying within the tracker acceptance $|\eta| < 2.5$. As electrons can form PFjets, PFTaus are required to be separated by $\Delta R > 0.3$ to electrons passing the kinematic and γ conversion criteria of Section 5.3. The biases introduced by these kinematic selections are acceptable as they are the minimal criteria applied in any analysis which uses PFTaus. Figure 5.20 shows the p_T distribution of the leading charged hadron of the PFTau as defined in Section 3.3.1 within $\Delta R_m = 0.1$ for both signal and QCD events with $\hat{p}_T \in [20\,\text{GeV/c}, 170\,\text{GeV/c}]$. A cut at $p_T^{ldg} > 5\,\text{GeV/c}$ was placed. The efficiency

of this track reconstruction cut, will be measured by the Tracking group using a sample of isolated charged pions and reconstructing tracks using pixel hits only.

5.4.2 PFTau Isolations

Isolation in the ECAL and Tracker follow in the form of PF γ (photon) and PF charged hadron isolation as described in Section 3.3.1. In order to collect a sample of events containing τ-jets whose structure (pions, photons) is unbiased by these selections, a large fixed size signal cone of $\Delta R_s = 0.15$ was chosen. For PF γ isolation, the isolation cone size ΔR^{γ}_{iso} and minimum PF γ p^{γ}_T were chosen to reduce the QCD background for minimal signal loss. Figure 5.21 shows the Signal over Background (S/B) and the Signal (S) as a function of ΔR^{γ}_{iso} and p^{γ}_T, for $\Delta R^{\gamma}_{iso} = (0.3, 0.5, 0.7, 0.9)$ and $p^{\gamma}_T > (0.5, 1.0, 1.5, 2.0)\,\mathrm{GeV/c}$. An isolation cone $\Delta R^{\gamma}_{iso} = 0.7$ was chosen with a conservative threshold of $p^{\gamma}_T > 1.5\,\mathrm{GeV/c}$ giving $S/B \sim 0.54$ for ~ 250 signal events at $100\,\mathrm{pb}^{-1}$ of integrated luminosity. Figure 5.22 shows the S/B and S as a function of ΔR^{had}_{iso} and p^{had}_T for $\Delta R^{had}_{iso} = (0.3, 0.5, 0.7, 0.9)$ and $p^{had}_T > (0.3, 0.6, 0.9, 1.2)\,\mathrm{GeV/c}$, in events which satisfy the PF γ isolation. A tight cut using $\Delta R^{had}_{iso} = 0.7$ and $p^{had}_T > 0.3$ was placed giving $S/B \sim 5.3$ for ~ 135 signal events at $100\,\mathrm{pb}^{-1}$ of integrated luminosity.

It is important to note that due to the limited statistics of QCD and γ+jets events and the tight electron selections, a factorisation of the electron and PFTau selections had to be applied in order to obtain such events passing all the selections of this analysis. In particular the number of QCD and γ+jets events passing the electron and PFTau selections were evaluated as

$$N_{e+\tau} = \frac{N_e}{N_e^{loose}} N_{e+\tau}^{loose} \tag{5.1}$$

where N_e^{loose} are the number of events passing the electron selections without applying the isolation and identification criteria of Sections 5.3.3 and 5.3.4 and $N_{e+\tau}^{loose}$ are the number of events passing the loose electron selections and PFTau selections. Equation was shown to be true within one σ when considering statistical fluctuations. The number of background events (B) in Figures 5.22 and 5.21 were evaluated using Equation (5.4.2). Table 5.11 summarises the efficiencies of these selections for τ-jets in signal events and EM enriched QCD events.

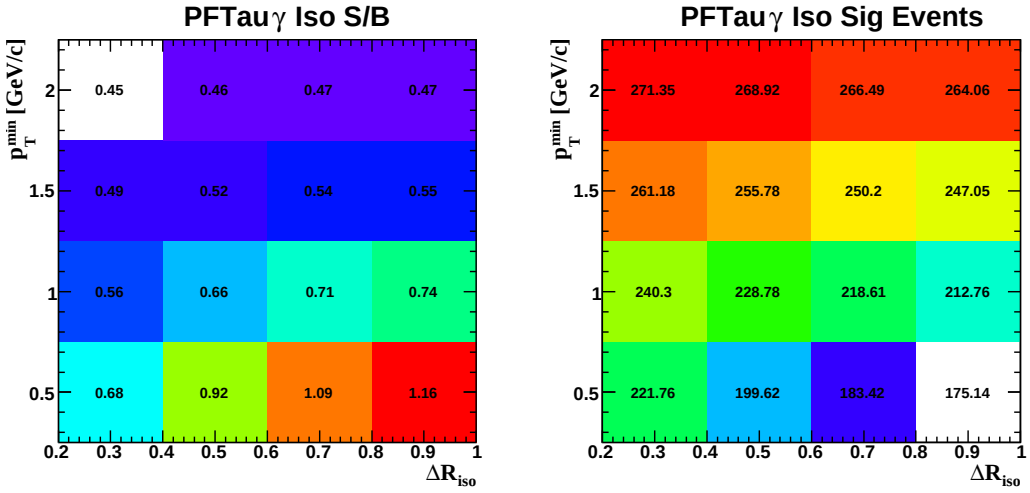

Figure 5.21: Signal over Background (S/B) (left) and the Signal (S) (right) as a function of ΔR^{γ}_{iso} and p^{γ}_{T}, for $\Delta R^{\gamma}_{iso} = (0.3, 0.5, 0.7, 0.9)$ and $p^{\gamma}_{T} > (0.5, 1.0, 1.5, 2.0)\,\mathrm{GeV/c}$ at $100\,\mathrm{pb}^{-1}$ of integrated luminosity for B being EM enriched QCD events with $\hat{p}_T \in [20\,\mathrm{GeV/c}, 170\,\mathrm{GeV/c}]$.

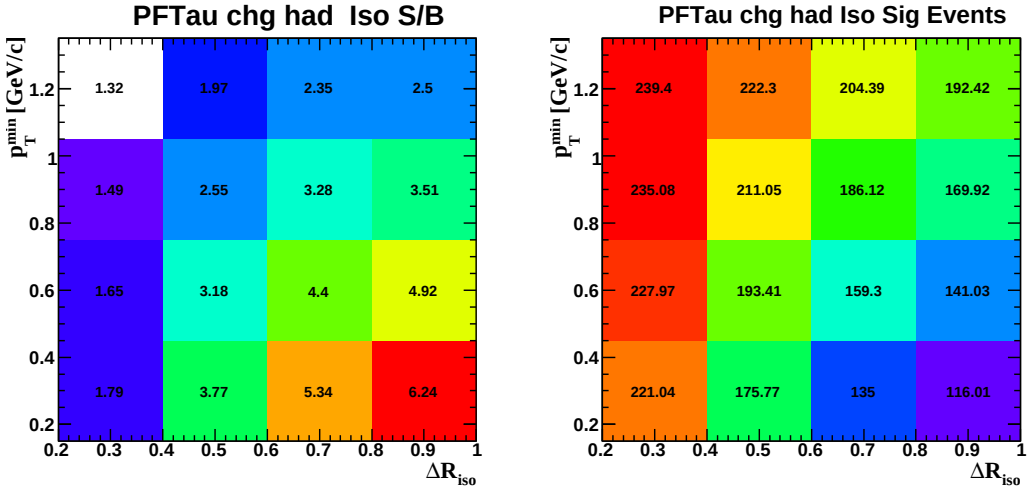

Figure 5.22: Signal over Background (S/B) (left) and the Signal (S) (right) as a function of ΔR^{had}_{iso} and p^{had}_{T} for $\Delta R^{had}_{iso} = (0.3, 0.5, 0.7, 0.9)$ and $p^{had}_{T} > (0.3, 0.6, 0.9, 1.2)\,\mathrm{GeV/c}$, in events which satisfy the PF γ isolation at $100\,\mathrm{pb}^{-1}$ of integrated luminosity B being EM enriched QCD events with $\hat{p}_T \in [20\,\mathrm{GeV/c}, 170\,\mathrm{GeV/c}]$.

Cut	Signal	QCD
e-τ ΔR>0.3	98.9%	69.2%
$p_T^{ldg} > 5\,GeV/c$	86.0%	36.5%
PF γ iso	75.6%	23.0%
PF had iso	40.3%	1.3%

Table 5.11: Table summarising the performance of the τ identification criteria on PF τ-jets formed out of real τ-jets QCD jets from EM enriched QCD events with $\hat{p}_T \in [20\,GeV/c, 170\,GeV/c]$. Efficiencies are cumulative with respect to PF τ-jets with $E_T > 15\,GeV/c$ in events where there is only one electron satisfying all the isolation and identification criteria of section 5.3 and the PF τ-jet is not collinear (ΔR>0.3) to the offline gsf electron which matches the HLT electron.

5.4.3 The Z($\rightarrow ee$)+jets background

Electrons from Z decays are well isolated objects both in the tracker and ECAL making them prime candidates for passing the τ-jet identification criteria. In order to deal with this source of fakes sophisticated algorithms were developed. These rely on identifying electrons which do not appear in the default electron collections mainly because they have radiated a very large fraction of their energy in tracker and failed the electron tracking criteria. Although these selections add a bias to the "core" structure of the τ-jet, their effect can be measured using Z$\rightarrow \tau\tau \rightarrow \tau$-jet+$\mu$+X events in which case the requirement of a well reconstructed muon means that Z$\rightarrow ee$ events do not contribute.

The τ-jet algorithm of electron rejection

A particle flow electron pre-identification algorithm [17], which employs a fast multivariate analysis of Tracker and ECAL information to reconstruct electron seeds (for the full electron reconstruction which identifies individual bremsstrahlung photons) with an efficiency of 90-95% across the whole tracker coverage for electrons and 5% for charged pions. The PFTaus whose leading charged hadron satisfies the above electron pre-id are flagged as electrons (but not vetoed). To further reduce contamination from electrons a set of cuts based on track p_T and ECAL/HCAL E_T were investigated. These were:

- The sum of all HCAL clusters associated to the PF τ-jet over the p_T of the leading PF charged hadron (H/P)

- The highest in E_T HCAL cluster associated to the PF τ-jet over the p_T of the leading PF charged hadron (H_{max}/P)

- The sum of HCAL clusters associated to the PF τ-jet within a cone $\Delta R < 0.183$ which corresponds to 3x3 HCAL towers, around the extrapolated impact point of the leading track on the ECAL surface over the the p_T of the leading PF charged hadron (H_{3x3}/P)

- The electromagnetic energy fraction of the PF τ-jet (EM_{frac}) and the summed energy of all ECAL clusters in a narrow strip $|\Delta\eta| < 0.04$ with respect to the extrapolated impact point of the leading track on the ECAL surface, divided by the p_T of the leading charged hadron (E/P) with the strip extending in $\Delta\phi$ up to 0.5 in the direction of the expected bremsstrahlung photon deposition

The performance of all of the variables for PF τ-jets matching electrons from Z decays and PF τ-jets matching τ-jets in $Z \rightarrow \tau\tau \rightarrow \tau$-jet+e+X events is shown in Figure 5.23. The left plot is for PF τ jets satisfying the leading track and isolation criteria of Section 5.4 in events where the single electron HLT has fired. The right plot shows the performance for PF τ jets satisfying the leading track and isolation criteria of Section 5.4 and do not match the reconstructed electron which fired the electron trigger in events where there is only one good electron satisfying the criteria of Section 5.3. Finally the variable used to reject electrons, whose performance is denoted by a cross in Figure 5.23, was:

1. E/P <0.80 or $H_{3x3}/P > 0.15$ for candidates not pre-identified (using PFlow) as electrons

2. E/P <0.95 or H_{3x3}/P>0.05 for candidates pre-identified (using PFlow) as electrons

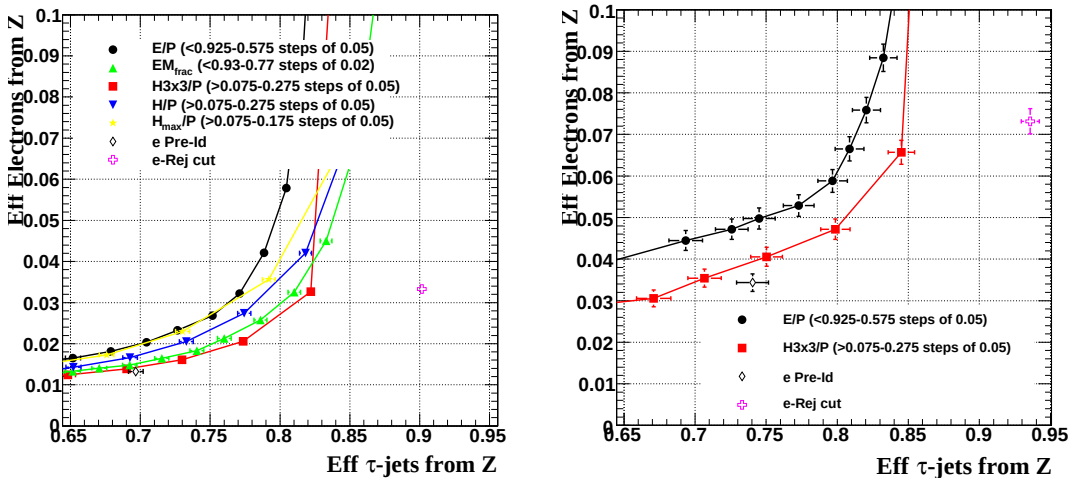

Figure 5.23: Performance of various electron rejection parameters as described in the text on τ-jets from Z$\rightarrow \tau\tau \rightarrow \tau$-jet+e+X and electrons from Z$\rightarrow ee$ in events where the HLT_IsoEle15_L1I has fired. The left plot is for PF τ-jets that pass tracking and isolation criteria described in 5.4. The right plot is for PF τ-jets that pass tracking and isolation criteria described in 5.4 and do not match (ΔR>0.3) the offline electron firing the HLT in events were there is only one electron satisfying all the isolation and identification criteria of section 5.3.

The choice of H_{3x3}/P is motivated by its good electron rejection performance as well as being less sensitive to the underlying event and pile-up compared to a sum of all the HCAL clusters within the PF τ-jet. Used in conjunction with the bremsstrahlung energy fraction E/P one can recover the signal efficiency to $(90.16 \pm 0.34)\%$ while keeping the electron rejection power at an acceptable level $(3.53 \pm 0.04)\%$.

However in this analysis events where required to contain only one electron satisfying all the isolation and identification criteria of Section 5.3 in addition to the PF τ-jet not to be collinear (ΔR>0.3) to the offline GSF electron which matches the HLT electron. This gives, a lower rejection power (right plot of Figure 5.23) due to the fact that badly reconstructed electrons not appearing in the GSF list are more likely to pass the electron rejection criteria due to their badly reconstructed track or large HCAL activity. For this case the efficiency on τ-jets is (93.56$\pm$0.63) and on electrons is (7.31 ± 0.30).

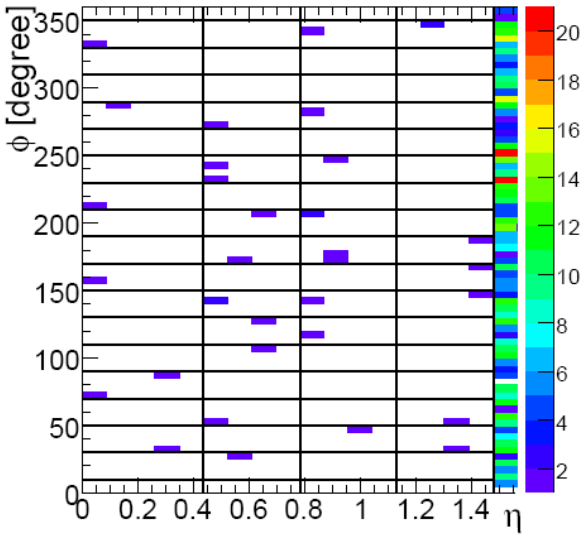

Figure 5.24: Extrapolated impact point of the electron track on the ECAL surface in η,ϕ for electrons passing the τ-jet isolation criteria with p_T^{MC} >20 GeV/c which have a 3x3 HCAL tower E_T sum around the impact point H_{3x3} >5 GeV. The vertical lines and horizontal lines denote position of ECAL cracks. A concentration of electrons in the η cracks is clearly visible, mostly at the ECAL barrel-endcap transition region ($|\eta| = 1.479$) [3].

Electrons going through ECAL cracks deposit their energy in the HCAL and therefore can pass the electron rejection criteria. Figure 5.24 shows the extrapolated impact point of the electron track on the ECAL surface in η,ϕ for electrons with MC $p_T > 20$ GeV matching reconstructed τ-jets which have a 3x3 HCAL tower E_T sum around the impact point H_{3x3} >5 GeV in a sub-sample of Z(ee)+jets events [3]. The vertical and horizontal lines denote position of ECAL cracks. A concentration of electrons in the η cracks is clearly visible, mostly at the ECAL barrel-endcap transition region ($|\eta| = 1.479$). Therefore a cut is placed to remove τ-jets whose extrapolated leading track position at the ECAL surface matches one of these cracks in η. The performance of this cut is summarised in Table 5.12.

A final method to identify and reject Z→ *ee* events where only one well identified electron satisfying the criteria of sections 5.3 is found and the PF τ-jet criteria (including electron rejection) are satisfied, is to form an invariant mass out of the well identified electron and any Super-Cluster in the event with E_T >8GeV. Events were at least one such pair lies within a Z mass window of 70 GeV/c^2 <M_{eSC} < 110 GeV/c^2 are rejected. The logic behind this method is that electrons from Z decays which

Cut	τ-jets	electrons
e-τ ΔR>0.3	$(98.85 \pm 0.17)\%$	$(35.67 \pm 0.23)\%$
$p_T^{ldg} > 5\,GeV/c$	$(86.03 \pm 0.56)\%$	$(30.95 \pm 0.22)\%$
PF had/γ iso	$(40.27 \pm 0.80)\%$	$(16.81 \pm 0.17)\%$
e-Rej Cut	$(37.68 \pm 0.79)\%$	$(1.22 \pm 0.05)\%$
ECAL Crack Cut	$(33.95 \pm 0.80)\%$	$(0.62 \pm 0.04)\%$

Table 5.12: Table summarising the performance of the τ identification criteria on PF τ-jets formed out of real τ-jets or electrons from Z decays. Efficiencies are cumulative with respect to PF τ-jets with $E_T > 15\,GeV/c$ in events were there is only one electron satisfying all the isolation and identification criteria of section 5.3 and the PF τ-jet is not collinear (ΔR>0.3) to the offline gsf electron which matches the HLT electron.

either are not pre-identified as electrons or their track momentum is badly measured, will still form Super-Clusters whose energy and position information can be used to identify Z$\rightarrow ee$ by forming an invariant mass with the well identified electron of the event. By requiring no Super-Cluster with $E_T > 8\,GeV$ forms an invariant mass with the well identified electron in the event within $70\,GeV/c^2 < M_{eSC} < 110\,GeV/c^2$ a per event efficiency of $\sim 98\%$ in Z$\rightarrow \tau\tau \rightarrow \tau$-jet+e+X and $\sim 16\%$ in Z$\rightarrow ee$ with respect to events which satisfy all the electron and τ-jet identification criteria including the electron rejection cut. The above efficiency was measured for events which also satisfied the topological selection criteria described in Section 5.5.

5.5 Topological and Opposite Sign Selections

A final set of topological criteria mainly to reject W+jets and $t\bar{t}$+jets events follow the electron and PFTau selections of Sections 5.3 and 5.4. Electrons in W+jets and $t\bar{t}$+jets events originate mainly from leptonic decays of W bosons. This means that the invariant mass ($M_{e\mathrm{MET}}$) between the electron and the missing transverse energy (E_T^{miss} or MET) four-vector will have larger values for such events compared to signal events where the electron and neutrino originate from τ-lepton decays. The left plot of Figure 5.25 shows this distribution in W+jets, $t\bar{t}$+jets and signal events which satisfy all the electron and PFTau selections of this analysis. A cut at $M_{e\mathrm{MET}} < 48\,GeV/c^2$ was placed where the MET vector is defined as

$$\overrightarrow{E}_T^{miss} = -\sum_i (\overrightarrow{E}_{Ti}^{calo}) - \sum_i \overrightarrow{p}_{Ti}^{\mu} \tag{5.2}$$

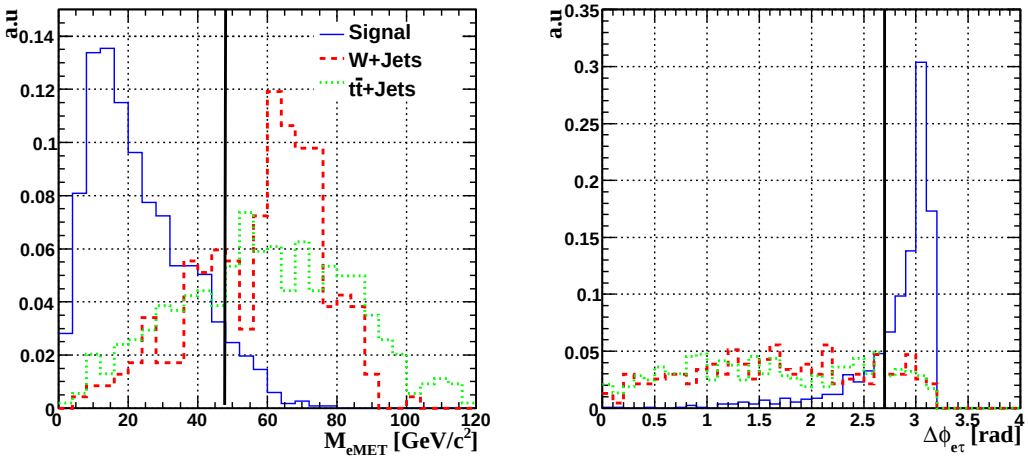

Figure 5.25: Left: The invariant mass ($M_{e\mathrm{MET}}$) between the selected electron and the missing transverse energy for signal (solid) W+jets (dashed) $t\bar{t}$+jets (dotted). Right: The opening angle in the transverse plain ($\Delta\Phi_{e\tau}$) between the PFTau and electron passing the selections of this analysis for signal (solid) W+jets (dashed) $t\bar{t}$+jets (dotted). The solid vertical line denotes the position of the cut.

with $\overrightarrow{\mathrm{E}}^{\mathrm{calo}}_{\mathrm{Ti}} = \mathrm{E}^{\mathrm{calo}}_{\mathrm{i}} \sin\theta_{\mathrm{i}} \cos\phi_{\mathrm{i}} \hat{\mathrm{x}} + \mathrm{E}^{\mathrm{calo}}_{\mathrm{i}} \sin\theta_{\mathrm{i}} \sin\phi_{\mathrm{i}} \hat{\mathrm{y}}$, which do not account for the expected muon energy deposition in the calorimeter to avoid double counting, and $\overrightarrow{\mathrm{p}}^{\mu}_{\mathrm{Ti}}$ is the transverse momentum vector of the i^{th} reconstructed muon. Although further topological cuts involving the missing transverse energy could be placed, the choice to minimise its use during the early data taking period was made as it requires good understanding of the whole detector system including electronic noise, underlying event and calibration and would add to the systematic error of the analysis.

Furthermore, the opening angle in the transverse plain ($\Delta\phi_{e\tau}$) between τ-jets and electrons from signal events is predominantly at π since the τ-leptons from the Z decay are back to back in the transverse plain and the products of the τ lepton decays are predominantly collinear with the τ leptons due to the large Lorentz boost as shown in the right plot of Figure 5.25. Therefore a cut was placed on $|\Delta\phi_{e\tau}| > 2.7\,\mathrm{rad}$ between the electron and PFTau satisfying all the selections of the analysis. Table 5.13 summarises the efficiencies of these selections.

Finally in order to further reduce backgrounds a cut on the charge between the electron and the PFTau was applied $\mathrm{OS}_{e\tau}$. As τ leptons from Z decays are oppositely

Selection	Signal	W+jets	$t\bar{t}$+jets
$\lvert\Delta\phi_{e\tau}\rvert > 2.7\,\text{rad}$	78.1%	15.4%	14.0%
$M_{e\text{MET}} < 48\,\text{GeV/c}^2$	93.8%	72.2%	48.6%
Total	73.3%	11.1%	6.8%

Table 5.13: Table summarising the efficiencies of the topological selections in signal, W+jets and $t\bar{t}$+jets events. Efficiencies are relative to the previous selection.

charged then so should be their products. The PFTau charge was defined as the charge of the leading charged hadron. This was done in order to minimise the bias on structure of the τ-jet.[1]

5.6 Results

Applying the selections defined in Sections 5.3, 5.4 and 5.5 to Signal and Background events one obtains the visible mass (invariant mass between electron and PFTau four-vectors) distribution $M_{e\tau}$ of Figure 5.26. The visible mass was used instead of the full mass which requires missing energy information, in order to reduce the dependance on the performance of E_T^{miss} during the early stages of data taking, which will take time to be understood. Table 5.14 summarises the number of Signal and Background events passing each selection for $100\,\text{pb}^{-1}$ of integrated luminosity. A final cut was placed on $M_{e\tau} \in (40, 88)\,\text{GeV}/c^2$ which gives 74.5 $Z\rightarrow \tau\tau \rightarrow \tau$-jet+e events with S/(S+B)=0.73. Figure 5.27 shows the PFTau E_T and η distribution for these events. It is clear that the background contribution to these distributions has to be extracted using either data driven techniques or well understood MC simulations in order to obtain the pure τ-jet kinematic distributions. It is worth noting that the distributions and number of events for QCD and γ+jets events were obtained by applying no electron isolation or identification and scaling these events by Equation (5.4.2). However even with this factorisation procedure a limited

[1] If the PFTau charge was defined as the sum of charges of PF charged hadrons within ΔR_{sig}, then the opposite sign criterion to the electron charge would fail for an even number of charged hadrons within ΔR_{sig} with opposite charged pairs resulting in a zero charged PFTau. An even number of charged hadrons within ΔR_{sig} for τ-jets can occur due to track reconstruction inefficiency or due to the presence of fake or photon conversion tracks. These τ-jets should not be omitted as it is vital to understand the behaviour of the PFTau selection algorithms for such cases.

Cut	Signal	EM enr QCD	$b/c \to e$ QCD	γ+ jets	W+ jets	Z(ee)+ jets	$t\bar{t}$+ jets
HLT	2821	7.8×10^6	1.9×10^6	254131	628851	74048	4687
e Kin	1719	3.4×10^6	815972	67168	297513	33684	1564
γ Conv	1568	2.3×10^6	525396	12746	271854	30947	1368
e Iso+Id	432	1996	645	795	62979	7323	169
τ Kin	340	728	229	308	5381	3853	129
τ Iso	146	25.2	8.4	21.2	293	2087	21.1
τ e-Rej	122	22.2	7.8	18.2	252	76.0	15.1
$OS_{e\tau}$	108	12.2	3.9	11.9	150	62.9	11.4
M_{eSC}	106	10.8	3.6	11.9	141	13.9	8.7
1τ + 1e	105	10.6	3.6	11.9	140	13.9	8.4
Topol.	76.9	6.2	2.1	8.4	15.6	6.7	0.6
$M_{e\tau}$	74.5	4.6	1.6	7.9	9.6	3.2	0.3
$\in (40, 88)$	±2.6	±0.5	±0.1	±3.1	±2.4	±0.9	±0.1

Table 5.14: Table summarising the selection and performance of all the selections in Signal and all the Background events considered. Events have been scaled to $100\,\mathrm{pb}^{-1}$ of integrated luminosity. The errors reflect the statistical uncertainty of the full samples used for this analysis.

number of γ+jets events survive all selections which leads to discrete distributions in Figures 5.26 and 5.27.

5.7 Background extraction

5.7.1 Introduction

In order to obtain kinematic distributions of pure Z$\to \tau\tau \to \tau$-jet+e+X events, the contribution from backgrounds has to be subtracted from the total number of events. Data driven techniques were developed to estimate the over-all normalisation and shape of the invariant mass between reconstructed and identified electrons and τ-jets as well as the E_T and η distributions of these τ-jets, in QCD and W+jets events. These methods involved selecting events using the Single Isolated electron trigger and then reversing offline isolation, identification or topological criteria. It is worth noting that the methods developed in this chapter to extract the background contributions will also be directly applied to analogous H$\to \tau\tau \to \tau$-jet+e+X searches as they share the same backgrounds as this analysis.

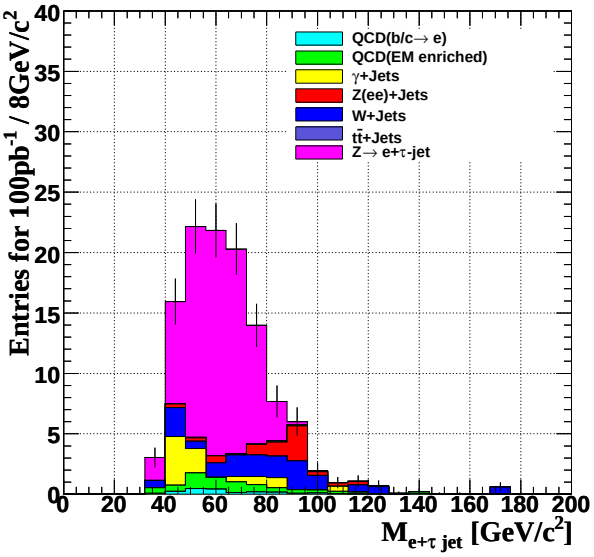

Figure 5.26: Invariant mass between PFTau and electron satisfying all selection criteria. Signal and Backgrounds are shown as stacked histograms. Events have been scaled to 100pb^{-1} however error bars denote the statistical uncertainty of the full samples used for this analysis. S/(S+B) 74% within $M_{e\tau} \in (40, 88)$.

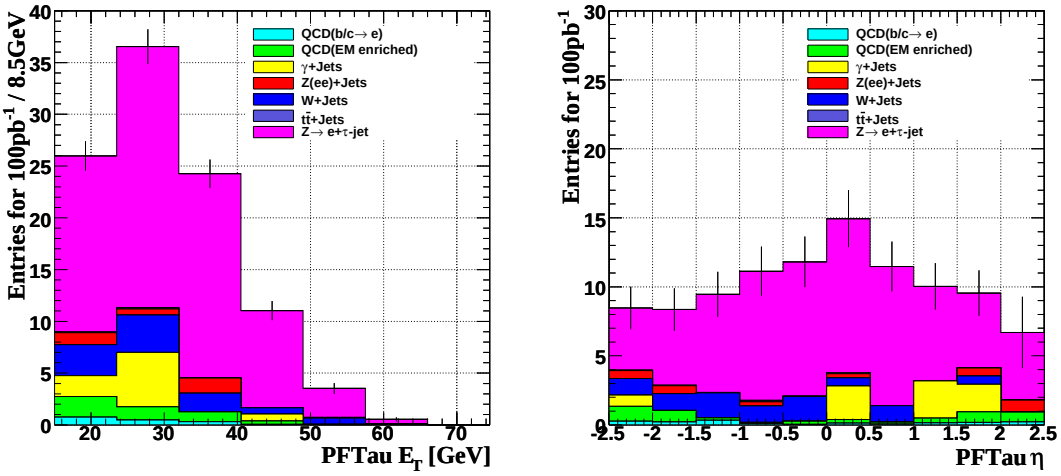

Figure 5.27: PFTau E_T (left) and η (right) distributions for PFTaus satisfying all selections including $M_{e\tau} \in (40, 88)$. Events have been scaled to 100pb^{-1} however error bars denote the statistical uncertainty of the full samples used for this analysis.

5.7.2 QCD extraction

QCD di-jet events are characterised by non isolated electron and τ-jet candidates. Therefore in order to estimate the QCD contribution passing all the selections described in the previous sections, one could estimate the contribution passing the reverse electron and τ-jet isolations (anti-iso) and extrapolate to the isolated region. The "ABCD" method used in [43] is based on considering two variables such as electron identification (including isolation) and τ-jet isolation and counting the number of events for four cases as shown below and in Figure 5.28.

- Case A: iso & id electron - iso τ-jet
- Case B: !(iso & id electron) - iso τ-jet
- Case C: iso & id electron - !(iso τ-jet)
- Case D: !(iso & id electron) - !(iso τ-jet)

Where "!" denotes the reverse (anti) selection.

The electron isolation was performed in the Tracker, ECAL and HCAL and the τ-jet isolation was performed in the Tracker and ECAL with parameters as described in previous sections. For all four regions, all the other selection criteria such as rejection of photon conversions for electrons and electron rejection for τ-jets were applied. Furthermore events were required to satisfy the $\Delta\phi_{e\tau}$, $\mathrm{M}_{e\mathrm{MET}}$ and $\mathrm{OS}_{e\tau}$ criteria discussed in previous sections.
If the electron and τ-jet selections are uncorrelated then

$$\frac{N_A^{QCD}}{N_B^{QCD}} = \frac{N_C^{QCD}}{N_D^{QCD}} \Rightarrow N_A^{QCD} = N_B^{QCD} \times \frac{N_C^{QCD}}{N_D^{QCD}} \tag{5.3}$$

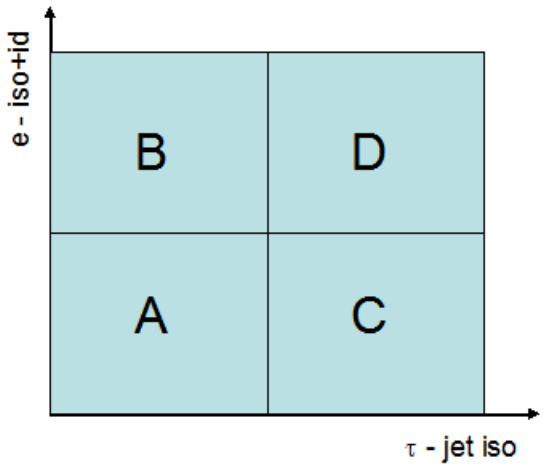

Figure 5.28: Figure demonstrating the four regions of the ABCD method described in the text.

In order to test the validity of this method, a statistically significant number of QCD events was required in every region. However due to the limited QCD samples available, a slightly looser set of electron identification criteria were applied. Specifically the ECAL isolation cut was loosened to $\Sigma E_T^{ECAL} < 2.0\,GeV$ instead of $\Sigma E_T^{ECAL} < 1.0\,GeV$ and no E/P or E2x5(E1x5)/E5x5 cuts were placed. Furthermore the dependence of the τ-jet isolation on the electron isolation and identification was studied separately for τ-jet Tracker and ECAL isolations as the combination of both would yield no events for Case A. Table 5.15 shows that equation is indeed valid for QCD events as the efficiencies of the τ-jet isolation (Tracker or ECAL) followed by all the other topological criteria, are independent of the electron isolation and identification. The main problem with this method is other events such as γ+jets, EWK and signal entering regions B,C or D. Table 5.16 summarises the number of events contributing to each of these regions both from QCD and other sources. In this case the electron and τ-jet selection criteria were restored to their original values in order to obtain contributions which faithfully reflect all the selections applied in this analysis.

As expected in Case C, out of a total 1200 events 26% originate from EWK processes (excluding signal) 10% from γ+jets events and 8% from signal events all of which contain real electrons. The EWK, signal and γ+jets contributions to region C can be evaluated using the cross section obtained by dedicated W/Z+jets and γ+jets

QCD	
Relation	Value
τ-jet Track Iso	
N_A/N_B	0.023 ± 0.009
N_C/N_D	0.022 ± 0.002
τ-jet ECAL Iso	
N_A/N_B	0.0220 ± 0.0025
N_C/N_D	0.0221 ± 0.0029

Table 5.15: Table testing the validity of Equation 5.7.2 in QCD events for extraction of the QCD background.

Cases	QCD	γ+ jets	EWK (excl Signal)	Signal	Total (QCD %)
B	9731 ± 537	122 ± 44	63 ± 5	132 ± 3	10048 (97%)
C	673 ± 144	116 ± 42	313 ± 12	97 ± 3	1199 (56%)
D	269460 ± 2842	1088 ± 130	1090 ± 22	296 ± 5	279340 (99%)

Table 5.16: Table showing the number of events passing the selections for each of the cases B,C,D us discussed in the text for QCD, γ+jets, EWK (W,Z,$t\bar{t}$+jets,and signal processes). Events have been scaled to $100\,\mathrm{pb}^{-1}$ of integrated luminosity. The total number of events collected for each region along with the fraction of QCD events contributing to the region, in brackets, are shown in the left most column.

analyses and scaling these by the electron efficiencies measured using Tag and Probe studies using electrons from Z$\rightarrow$ *ee* events [43]. τ-jet and mis-tag rates can be measured using jets from QCD di-jet or recoil jets from Z(ee)+jets events. Therefore this adds a systematic uncertainty on the estimated number of QCD events. However for Cases B and D QCD accounts for 97% and 99% of the total number of events for these regions and therefore the contribution from other sources was considered negligible.

The shape of the invariant mass between the final electron and PF τ-jet as well as the PF τ-jet E_T and η were extracted by looking at events satisfying reverse offline electron track isolation and no further isolation or identification requirements on the electron (a-iso electron, not to be confused with anti-iso electron) and extrapolating to the full isolation and identification case. In order to check the validity of this method a substantial amount of QCD was required to pass all the criteria for the isolated electron case. Therefore the PF τ-jets were required to have an E_T >15 GeV,

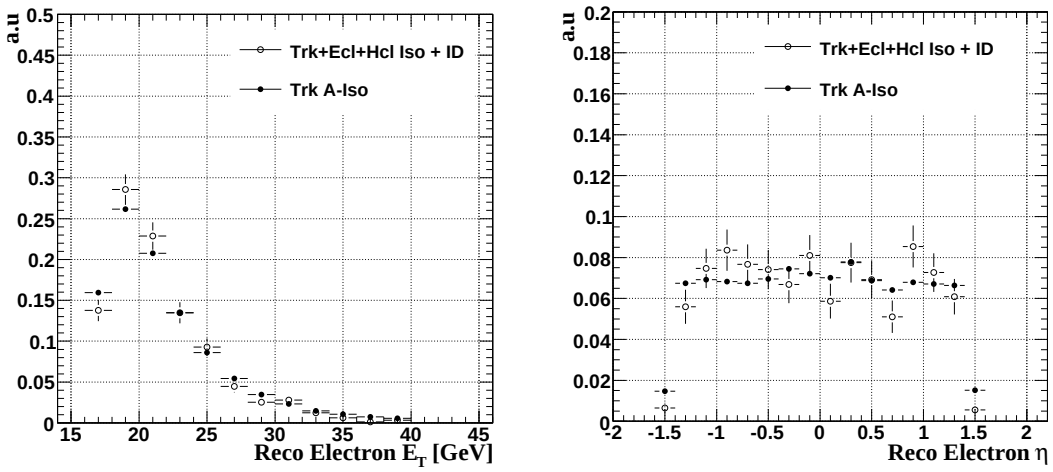

Figure 5.29: Distribution of E_T (left) and η (right) of the offline electron for electrons satisfying all isolations and identification criteria (open circles) and for electrons satisfying reversed track isolation with no other isolation or identification applied (full circles).

a ΔR >0.3 with the offline electron and a p_T^{Ldg} >5 GeV/c but no τ-jet isolation requirements for both the isolated and a-iso electron cases. The lack of τ-jet isolation criteria does not affect the validity of this method as we are interested only in the relative agreement in the kinematic distributions of events satisfying the isolated or a-iso electron cases.

Figure 5.29 shows the E_T and η distributions for electrons passing the offline isolation and identification criteria and for electrons satisfying reverse offline track isolation requirement with no other offline isolation or identification criteria applied (a-iso electron). A reasonable agreement was obtained within statistical uncertainties. The left plot of Figure 5.30 shows the invariant mass distribution between the isolated or a-iso electron and the PF τ-jet for QCD $\hat{p}_T \in [20\,\text{GeV/c}, 170\,\text{GeV/c}]$. A clear discrepancy was observed between isolated and a-iso electron cases (Kolmogorov Prob=1×10^{-4}). As no isolation was applied to the PF τ-jet, in order to emulate the effect the PF τ-jet isolation would have on the PF τ-jet kinematics, the right plot of Figure 5.30 shows the invariant mass between the isolated or a-iso electron and the vector sum of the PF candidates (photons, charged and neutral hadrons) within the signal cone of the PF τ-jet. A better agreement was obtained between the isolated and a-iso electron cases (Kolmogorov Prob=7.5×10^{-2}). The discrepancy in the

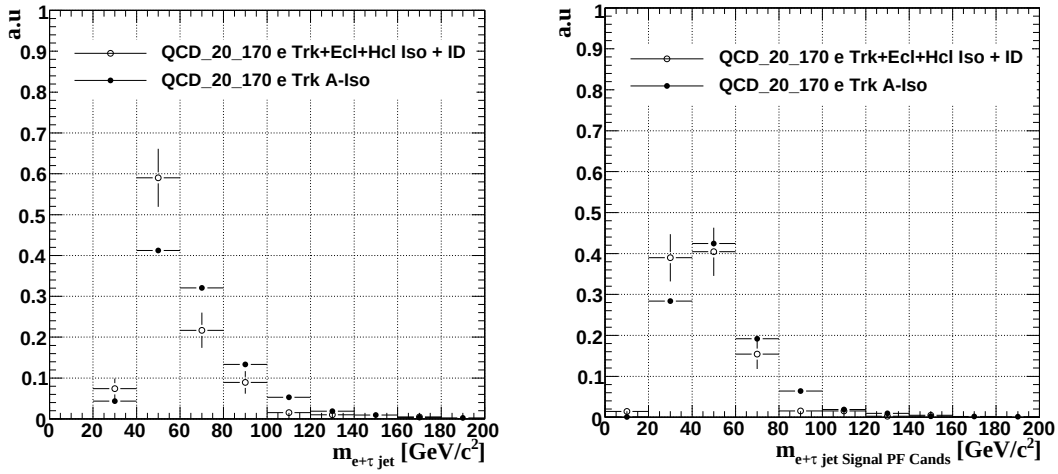

Figure 5.30: Left: Distribution of the visible invariant mass between the electron and PF τ-jet for isolated and anti-isolated electrons (Kolmogorov Prob=1×10^{-4}) . Right: Distribution of the visible invariant mass between the electron and the vector sum of the PF τ-jet constituents within the signal cone (Kolmogorov Prob=7.5×10^{-2}). No isolation was applied on the PF τ-jet to increase statistics.

mass shapes is mainly due to the dependance of the τ-jet kinematics on whether there is an isolated or a-iso electron in the event. Figures 5.31 and 5.32 show the E_T and η distributions of the PF τ-jet and the vector sum of PF candidates within the isolation cone respectively. As expected a better agreement was obtained for the latter case as the signal constituents are less sensitive to the rest of the event.

A closer inspection revealed that by omitting the QCD $\hat{p}_T \in [20\,\mathrm{GeV/c}, 30\,\mathrm{GeV/c}]$ a better matching of the invariant mass, PF τ-jet (vector sum of PF candidates in signal cone) E_T and η between cases containing an isolated or a-iso electron as shown in Figures 5.33, 5.34, 5.35 where a Kolmogorov Test yielded a probability of 0.98 for the E_T distribution of the vector sum of PF candidates in the signal cone.

In order to fully understand these discrepancies a deeper analysis using a larger QCD sample is required. However due limited available statistics, a Monte Carlo based correction factor was placed in order to obtain the correct invariant mass and PF τ-jet E_T and η distributions. This MC correction introduced a systematic uncertainty in this analysis.

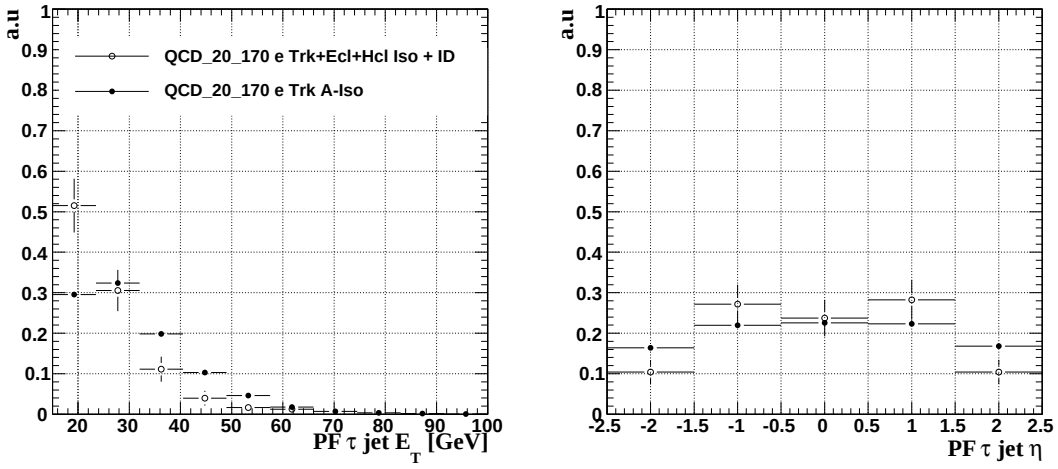

Figure 5.31: E_T (left) and η (right) distributions of the PF τ-jet in events containing isolated (open circles) or anti-isolated (full circles) electron for QCD $\hat{p}_T \in [20\,\mathrm{GeV/c}, 170\,\mathrm{GeV/c}]$ events. No isolation was applied on the PF τ-jet to increase statistics. A Kolmogorov Test yielded a probability of 3×10^{-5} for E_T and 0.73 for η.

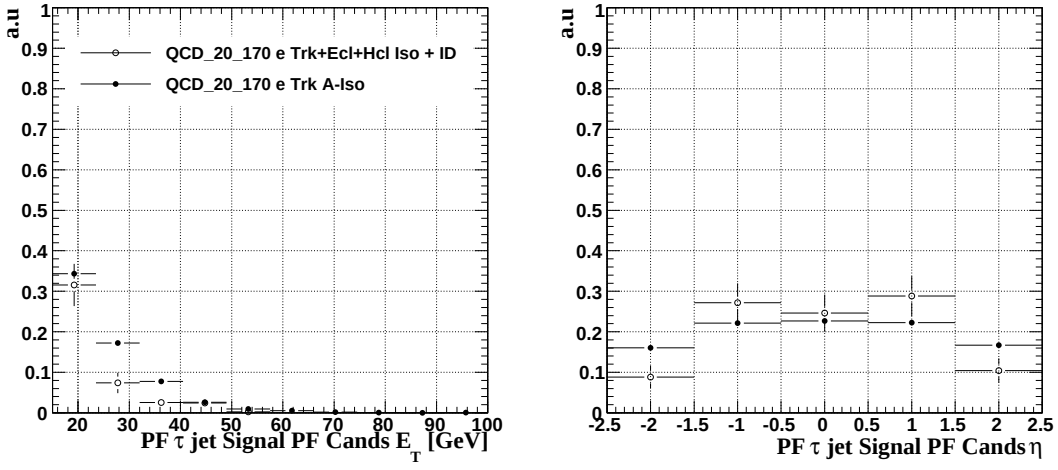

Figure 5.32: E_T (left) and η (right) distributions of the vector sum of the PF candidates within the isolation cone of the PF τ-jet in events containing isolated (open circles) or anti-isolated (full circles) electron for QCD $\hat{p}_T \in [20\,\mathrm{GeV/c}, 170\,\mathrm{GeV/c}]$ events. No isolation was applied on the PF τ-jet to increase statistics. A Kolmogorov Test yielded a probability of 0.09 for E_T and 0.58 for η.

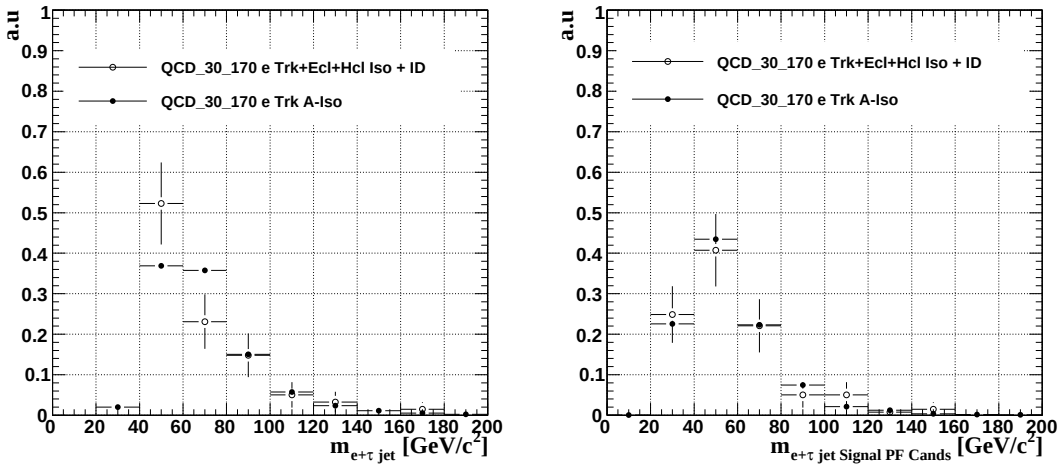

Figure 5.33: Left: Distribution of the visible invariant mass between the electron and PF τ-jet for isolated and anti-isolated electrons (Kolmogorov Prob=0.33) . Right: Distribution of the visible invariant mass between the electron and the vector sum of the PF τ-jet constituents within the signal cone for isolated and anti-isolated electrons (Kolmogorov Prob=0.98). No isolation was applied on the PF τ-jet to increase statistics.

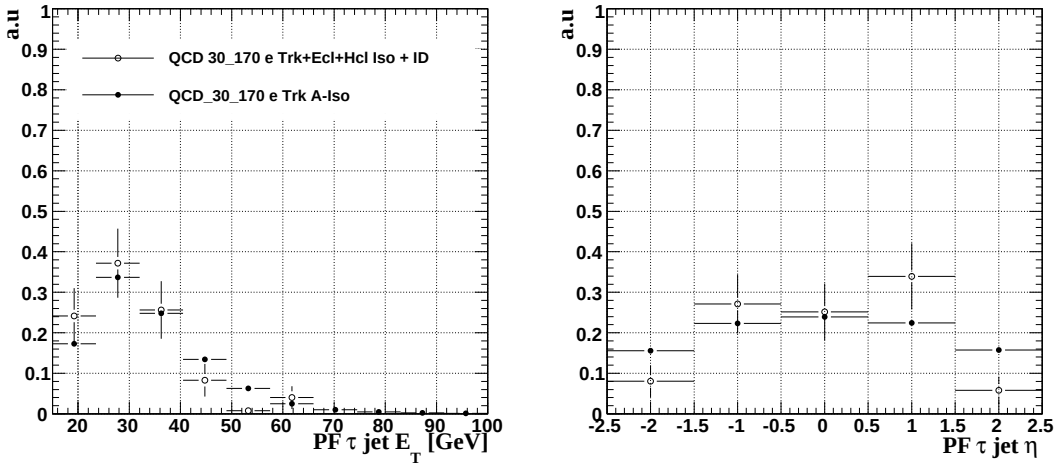

Figure 5.34: E_T (left) and η (right) distributions of the PF τ-jet in events containing isolated (open circles) or anti-isolated (full circles) electron for QCD $\hat{p}_T \in [30\,\mathrm{GeV/c}, 170\,\mathrm{GeV/c}]$ events. No isolation was applied on the PF τ-jet to increase statistics. A Kolmogorov Test yielded a probability of 0.58 for E_T and 0.69 for η.

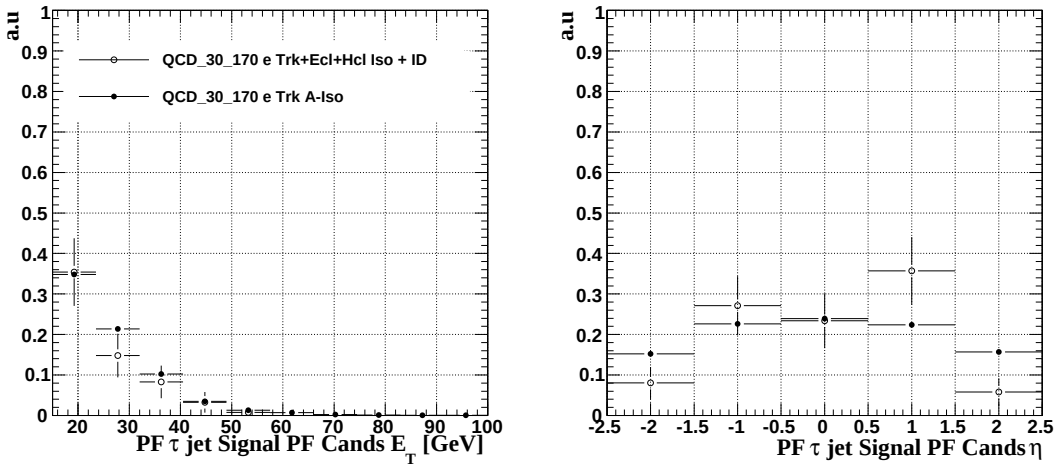

Figure 5.35: E_T (left) and η (right) distributions of the vector sum of the PF candidates within the isolation cone of the PF τ-jet in events containing isolated (open circles) or anti-isolated (full circles) electron for QCD $\hat{p}_T \in [30\,GeV/c, 170\,GeV/c]$ events. No isolation was applied on the PF τ-jet to increase statistics. A Kolmogorov Test yielded a probability of 0.97 for E_T and 0.70 for η.

Selections	QCD	γ+jets, EWK	Total (QCD %)
$OS_{e\tau}$ a-iso e,iso τ-jet,(M_{eMET},$\Delta\phi_{e\tau}$)	7740 ± 488	174 ± 10	7914 (98%)

Table 5.17: Table summarising the number of events passing the selections used to estimate the QCD mass and τ-jet kinematic distributions. Events have been scaled to $100\,pb^{-1}$ of integrated luminosity.

Finally a check was performed to ensure that the number of events passing the a-iso electron criteria followed by the full PF τ-jet isolation and topological criteria including the OS requirement between the electron and the PF τ-jet leading track, were dominated by QCD events. Table 5.17 summarises these results with QCD contributing 98% of the total number of events passing these selections.

5.7.3 W+jets extraction

Extraction of the total number of W+jets events passing all the selections was performed using the "ABCD" method described in Section 5.7.2. The independent variables used this time were the combination of the $\Delta\phi_{e\tau}$, M_{eMET} cuts and the τ-jet isolation. In order to reduce the contribution of QCD events, electron isolation and

identification was applied to all regions. This time the four regions were defined as follows:

- Case A: $\Delta\phi_{e\tau} > 2.7\,\text{rad}$ & $\text{M}_{e\text{MET}} < 48\,\text{GeV/c}^2$ - iso τ-jet
- Case B: $\Delta\phi_{e\tau} < 2.7\,\text{rad}$ & $\text{M}_{e\text{MET}} > 48\text{GeV/c}^2$ - iso τ-jet
- Case C: $\Delta\phi_{e\tau} > 2.7\,\text{rad}$ & $\text{M}_{e\text{MET}} < 48\,\text{GeV/c}^2$ - !(iso τ-jet)
- Case D: $\Delta\phi_{e\tau} < 2.7\,\text{rad}$ & $\text{M}_{e\text{MET}} > 48\,\text{GeV/c}^2$) - !(iso τ-jet)

Table 5.18 shows the validity of this method in W+jets events.

W+jets	
Relation	Value
τ-jet Track and ECAL Iso	
N_A/N_B	0.11 ± 0.02
N_C/N_D	0.10 ± 0.01

Table 5.18: Table testing the validity of Equation 5.7.2 in W+jets events for extraction of the W+jets background.

Cases	QCD	γ+ jets	Z(ee)+ jets ,	$t\bar{t}$+ jets ,	W+ jets	Signal	Total (W+jets %)
B	0	0	10 ± 1		117 ± 8	3 ± 0.5	130 (90%)
C	673 ± 144	116 ± 42	35 ± 2		279 ± 13	97 ± 3	1200 (23%)
D	50 ± 39	0	73 ± 3		1957 ± 32	4 ± 0.5	2084 (94%)

Table 5.19: Table showing the number of events passing the selections for each of the cases B,C,D as discussed in the text for QCD, γ+jets, Z(ee),$t\bar{t}$+jets,and signal processes. Events have been scaled to $100\,\text{pb}^{-1}$ of integrated luminosity. The total number of events collected for each region along with the fraction of W+jets events contributing to the region, in brackets, are shown in the left most column.

As shown in Table 5.19 the main problem with this method is that Case C is dominated by QCD and γ+jets events which must be subtracted before the W+jets

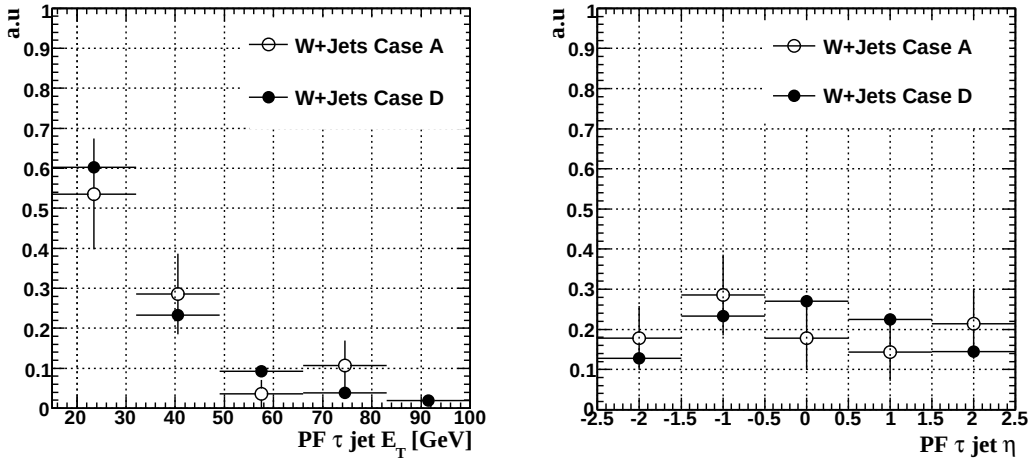

Figure 5.36: Left: Distribution of the final PF τ-jet E_T (left) and η (right) for Cases A and D.

contribution can be evaluated. This can be done by in various ways, such as using the cross section of these processes from dedicated analysis and scaling these by the efficiencies of our selections obtained from data as discussed in Section 5.7.2 or MC. Therefore this introduced a systematic uncertainty on the estimated number of W+jets events.

In order to subtract correctly the W+jets contribution, the shapes of the distributions of the visible invariant mass between the final electron and PF τ-jet candidates ($M_{e\tau}$), and the E_T and η of the final τ-jet should also be obtained. Figure 5.36 shows the τ-jet E_T and η distributions for Cases A and D. A good agreement is obtained within statistical uncertainties demonstrating that the τ-jet E_T distribution could be obtained by applying the selections of Case D. The visible mass depends on the topology of the final electron and τ-jets. This means that as Cases A and D apply opposite $\Delta\phi_{e\tau}$ selections, the visible mass distributions differ as shown on the left plot of Figure 5.37. However Cases A and C apply the same $\Delta\phi_{e\tau}$ and hence a good agreement is obtained as shown in the right plot of Figure 5.37. Therefore the W+jets visible mass shape can be obtained by applying the selections of Case C and subtracting the QCD, γ+jets and signal contributions which can be obtained either from data or MC.

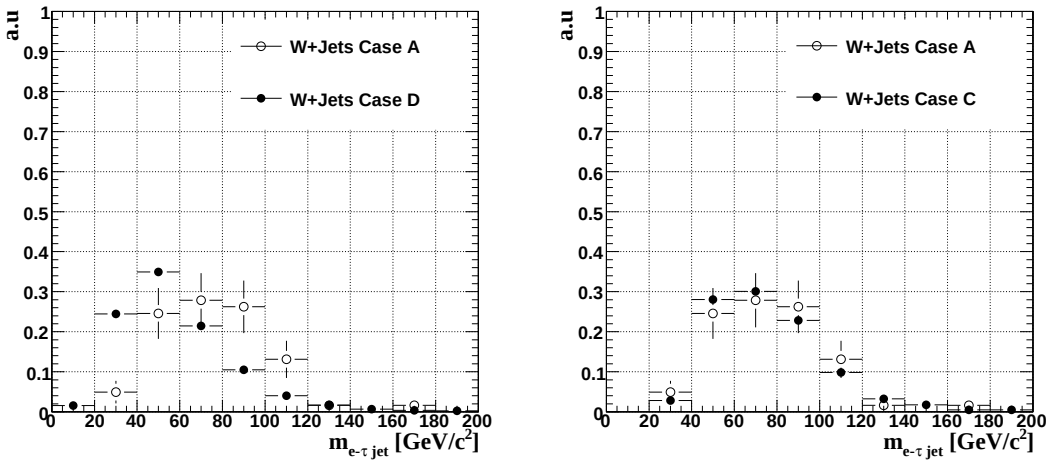

Figure 5.37: Distribution of the visible invariant mass between the electron and τ-jet for Cases A and D (left) and Cases A and C (left) in W+jets events.

5.7.4 Z(ee)+jets extraction

A preliminary investigation of a method for extracting the Z(ee)+jets background using data driven techniques was performed and documented in [3][60]. It was based on firstly applying all selections of this analysis apart from the electron rejection cuts described in Section 5.4.3 and counting the number of events within the $M_{e\tau} \in (70, 110)\,\mathrm{GeV}/c^2$ window which is dominated by Z(ee)+jets events (N_{ee}). Then the electron rejection selections were reversed (τ-veto) and the number of events within $M_{e\tau} \in (70, 110)\,\mathrm{GeV}/c^2$ were counted $N_{ee}^{\tau\mathrm{v}}$. Therefore the number of Z(ee)+jets passing the selections of this analysis including the electron rejection cut (N_{ee}^{er}) could be obtained by

$$N_{ee}^{\mathrm{er}} = N_{ee}^{\tau\mathrm{v}} \times (1 - \frac{N_{ee}}{N_{ee}^{\tau\mathrm{v}}}) \tag{5.4}$$

However a better understanding in the extraction of the kinematic distributions of such events was required and therefore in the context of this analysis, this background was extracted using only MC simulation information and therefore introduced a systematic uncertainty.

5.7.5 γ+jets extraction

The γ+jets background accounts for a significant amount ($\sim$ 30%) of the total backgrounds of this analysis as shown in Table 5.14 and needs to be extracted using data driven techniques. However for the purpose of this analysis, this background was extracted using only MC simulation information and therefore introduced a systematic uncertainty to this analysis.

5.8 Measuring the τ-jet core selection efficiencies

The τ-jet is a composite object made up of a collection of $\pi^{+/-}$ and π^0's which decay predominantly to photons. This means that τ-jet identification algorithms which rely on requiring isolated τ-jets in the tracker and calorimeter, are sensitive both to underlying event and pile-up as well as the kinematics of the core (constituent) τ-jet objects which can leak energy into the isolation regions. The loss of efficiency due to the underlying event can be measured in Z$\rightarrow ee/\mu\mu$ events as the particle content and kinematics of the underlying event should be independent of the Z decay products. Figure 5.38 shows the average number of Particle Flow charged hadrons and photons as a function of their distance ΔR in η,ϕ space from the reconstructed jet axis in Z($\rightarrow ee$)+jets and Z($\rightarrow \tau\tau \rightarrow \tau$-jet+e+X)+jets events. A good agreement in the particle multiplicities is observed for ΔR $\gtrsim$0.15. Therefore the loss of efficiency due to the underlying event can be measured using Z$\rightarrow ee$ decays due to the large and clear signature [61]. The loss of efficiency due to the topological structure of the constituents of the τ-jets can be measured using Z$\rightarrow \tau\tau \rightarrow \tau$-jet+e/$\mu$+X events. The efficiency of the electron rejection algorithms on τ-jets however cannot be measured easily in Z$\rightarrow \tau\tau \rightarrow \tau$-jet+e+X events due to the contribution of Z$\rightarrow ee$ events. However this efficiency can be measured in Z$\rightarrow \tau\tau \rightarrow \tau$-jet+$\mu$+X events in which case the requirement of a well reconstructed muon means that Z$\rightarrow ee$ events do not contribute.

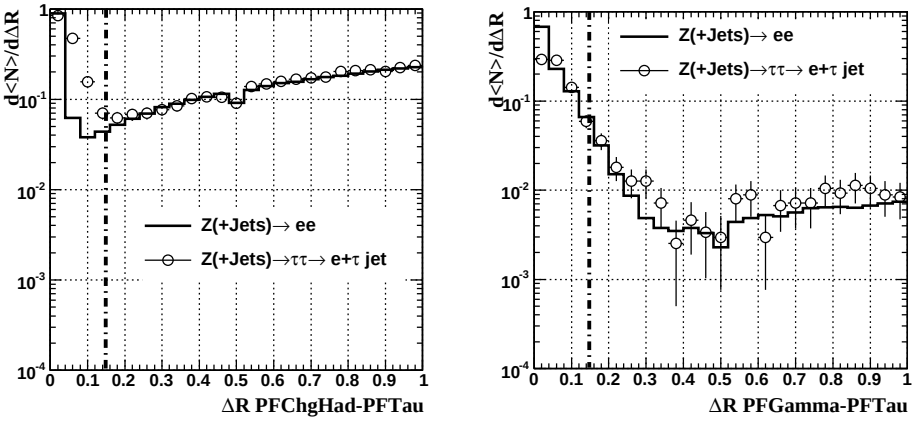

Figure 5.38: Distribution of the average number of particle flow charged hadrons (left) and photons (right) as a function of their distance ΔR in η,ϕ space from the reconstructed jet axis in Z(+jets)$\rightarrow ee$ and Z(+jets)$\rightarrow \tau\tau \rightarrow \tau$-jet+e+X events.

5.8.1 Efficiency Definitions

The PFTau selections applied in this analysis were chosen to minimise any biases on the core objects of the τ-jet. Isolations were applied between $0.15 < \Delta\mathrm{R} < 0.7$ and the opposite sign requirement (OS) was placed between the electron charge and the charge of the leading PF charged hadron of the PFTau. Therefore the efficiencies of the τ-jet core charged hadron isolation and 1 or 3 prong [2] requirements ($\epsilon_{\mathrm{ch}}^{\mathrm{Iso}}$, $\epsilon_{\mathrm{ch}}^{1||3}$) with $\Delta\mathrm{R} = 0.07$, $\Delta\mathrm{R}_{\mathrm{iso}} = 0.15$ and $\mathrm{p_T^{trk}} > 1\,\mathrm{GeV/c}$ were measured with respect to PFTaus with $\mathrm{E_T} > 15\,\mathrm{GeV}$ satisfying the selection criteria of Sections 5.4 and 5.4.3. Furthermore these events were required to satisfy all the electron selections of Section 5.3, all the topological selections of Section 5.5 including the $\mathrm{OS}_{e\tau}$ requirement and $\mathrm{M_{e\tau jet}} \in (40, 88)\,\mathrm{GeV/c^2}$. Finally the τ-jet core efficiency due to selection i as a function of the kinematic variable p can be written as

$$\epsilon_{\mathrm{ch}}^{i}(p) = \frac{N_{\mathrm{tot}}^{i}(p) - N_{\mathrm{bkg}}^{i}(p)}{N_{\mathrm{tot}}^{m}(p) - N_{\mathrm{bkg}}^{m}(p)} \tag{5.5}$$

where N_{tot}^{m} and N_{bkg}^{m} denote the total and background events respectively within $\mathrm{M_{e\tau}} \in (40, 88)\,\mathrm{GeV/c^2}$.

[2] Prong here refers to PF charged hadrons within a signal cone $\Delta\mathrm{R_s}$ with $\mathrm{p_T} > \mathrm{p_T^{trk}}$

5.8.2 Systematic Uncertainties

The systematic uncertainty on the τ-jet efficiency measurement arises mainly from the uncertainties involved in estimating the number of background events satisfying all the selection criteria of this analysis. These uncertainties can be divided into three categories. Firstly errors due to the estimation of W+jets(QCD), γ+jets, Z+jets, $t\bar{t}$+jets contributing in region C of the ABCD method for estimating QCD(W+jets) events as well as errors in the estimation of γ+Jet events satisfying all the selection criteria, which for now relies solely on Monte Carlo. Secondly errors arising from the estimation of the PFTau E_T and η distributions in QCD events. Thirdly errors due to the $\frac{N_A}{N_B} = \frac{N_C}{N_D}$ assumption of the ABCD method.

For the first case, the contributions of W+jets, γ+jets, Z(ee)+jets, $t\bar{t}$+jets and Z$\rightarrow e+\tau$-jet in region C of the ABCD method as well as the contribution of γ+jets and $t\bar{t}$+jets in the signal region could be evaluated using the number of events obtained by dedicated W/Z+jets and γ+jets analyses and using our event selection efficiencies obtained from the simulation to scale these number of events. In this way the background normalisation uncertainty does not include the jet energy scale uncertainties related with the PFJet kinematics [21]. The remaining uncertainties involve the systematic errors in the electron and PFTau identification efficiencies as well as in the E_T^{miss} which contributes to the M_{eMET} selection all of which have been obtained from simulation. Table 5.20 summarises the approximate expected uncertainties for O(100 pb^{-1}) of integrated luminosity. A 5% uncertainty was associated to the τ-jet$-$PFTau selection efficiency. at O(1 fb^{-1}) of statistics [21]. For O(100 pb^{-1}) this value was doubled instead of tripled as the scaling down of luminosity would suggest, since even at O(100 pb^{-1}), a significant amount of $Z \rightarrow ee$ [43] and isolated pions from QCD [62] will be collected to measure the loss of efficiency due to the underlying event and track reconstruction efficiency respectively.

For the second case, a simulation based correction factor was required in order to obtain the correct PFTau E_T and η distributions for QCD events passing all the selections using the techniques described in Section 5.7.2 and Figures 5.35, 5.32. This factor was evaluated by dividing the two distributions (isolated/a-iso) in each

Background process	W+ jets	γ+ jets	Z(ee)+ jets	$t\bar{t}$+ jets	Z$\rightarrow e+\tau$-jet
Events for $100\,\mathrm{pb}^{-1}$	9.6	7.9	3.2	0.3	74.5
Source of uncertainty	value %				
MET scale	25	23	20	10	20
Jet or e−PFTau eff	20	20	20	20	–
τ-jet−PFTau eff	–	–	–	–	10
e eff	1	1	1	1	1
Normalisation uncertainty	2	15	1	1	1
Total uncertainty	32	34	28	22	22

Table 5.20: Table summarising the approximate expected uncertainties of the selections for $\mathrm{O}(100\,\mathrm{pb}^{-1})$ of integrated luminosity [21][22]. The large normalisation uncertainty of the γ+jets events is due to the lack of such an analysis.

of Figures 5.35, 5.32 which were based on simulated data studies resulting in a systematic error in this correction arising from differences in the kinematics of jets between PYTHIA simulated data and real LHC data. At the Tevatron experiments it was found that the PYTHIA parameters [56] had to be tuned in order to correctly describe the kinematics and multiplicities of the underlying event. The first tuning of the PYTHIA parameters gave a maximum discrepancy of 30% for CDF [63][64]. At CMS a dedicated group aims to tune the PYTHIA parameters from the very start of data taking using 1,10 and $100\,\mathrm{pb}^{-1}$ of data [65]. Therefore a conservative systematic error of 30% was placed on the correction factor for the PFTau $\mathrm{E_T}$ and η even though the kinematics of the hard scatter will be more accurately modeled by PYTHIA from the very beginning [56]. Moreover as no data driven technique to obtain the PFTau kinematic distributions in γ+jets was investigated, these distributions had to be obtained purely from simulations and therefore the same source of systematic error was added to account for the discrepancies in the kinematic distributions of jets between PYTHIA simulations and LHC data.

For the third case, Table 5.15 shows the validity of the ABCD method in QCD events, however it suffers from large statistical errors. Therefore a correction factor f was used such that $\frac{N_A}{N_B} = f\frac{N_C}{N_D}$. The value of f was taken to be a gaussian of $\mu = 1$ and $\sigma = 0.45$ which corresponds to a fluctuation of $(\frac{N_A}{N_B})_{QCD}$ by 1σ. In contrast the validity of the ABCD method in W+jets events was established with significant certainty, as show in Table 5.18, to ignore such a correction factor.

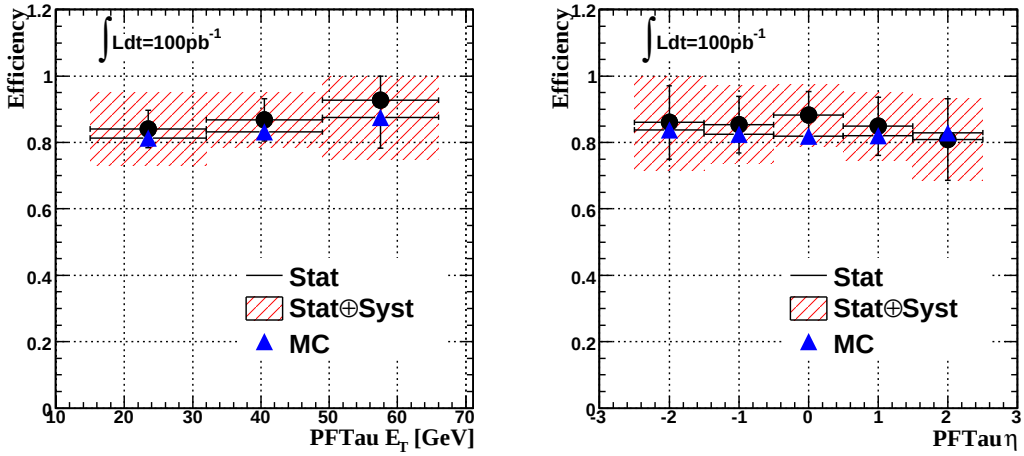

Figure 5.39: PF charged hadron isolation efficiency ($\epsilon_{\mathrm{ch}}^{\mathrm{Iso}}$) as defined in Section 5.8.1 as a function of $\mathrm{E_T}$ (left) and η (right).

Finally the systematic error in the efficiency was estimated by considering the effect of these three sources of uncertainties in Equation (5.5) and running 10,000 toy Monte-Carlo experiments for each PFTau $\mathrm{E_T}$ and η bin.

5.8.3 Results

Figure 5.39 shows the PF charged hadron isolation efficiency ($\epsilon_{\mathrm{ch}}^{\mathrm{Iso}}$) as defined in Section 5.8.1. The black circles correspond to events satisfying all the PFTau, electron and topological selections of this analysis and are therefore "Data-like". In contrast the blue triangles require the PFTau to match within $\Delta\mathrm{R} < 0.2$ the MC τ-jet in events which has fired the single isolated electron HLT with no other electron or topological selections applied. Two independent $\mathrm{Z}\rightarrow \tau\tau \rightarrow \tau$-jet+e+X samples were used for the "Data-like" and "MC" cases to ensure any agreement between the two cases is uncorrelated. The black error bars correspond to statistical errors for $100\,\mathrm{pb}^{-1}$ of integrated luminosity. The shaded area denotes the statistical and systematic errors added in quadrature. A good agreement is obtained between the "Data-like" and "MC" cases proving that the electron and topological selections of $\mathrm{Z}\rightarrow \tau\tau \rightarrow \tau$-jet+e+X events do not bias $\epsilon_{\mathrm{ch}}^{\mathrm{Iso}}$. The PFTau "core" track isolation was evaluated as $85.5\%\pm4.0\%\,(\mathrm{stat.})\pm5.7\%\,(\mathrm{syst.})$

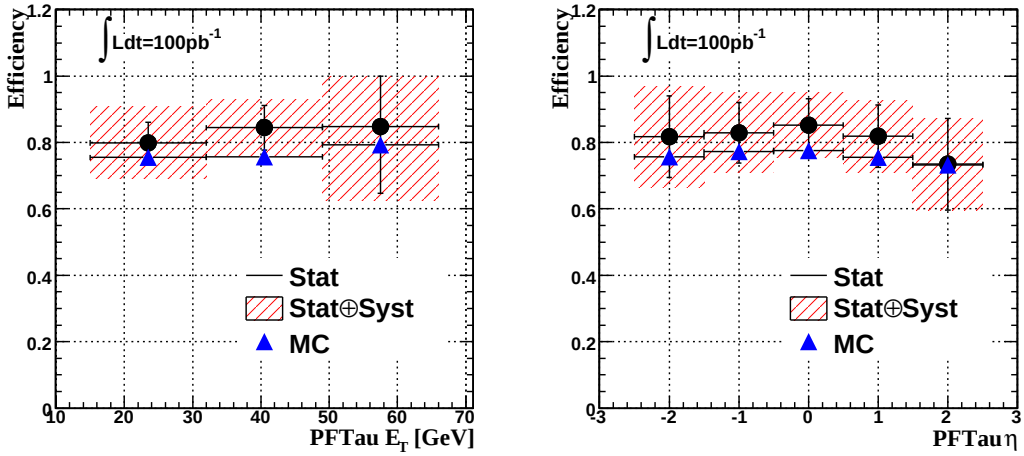

Figure 5.40: Efficiency of the 1 or 3 prong selection ($\epsilon_{\mathrm{ch}}^{1||3}$) as defined in Section 5.8.1 as a function of $\mathrm{E_T}$ (left) and η (right).

Similarly Figure 5.40 shows the $\epsilon_{\mathrm{ch}}^{\mathrm{Iso}} \times \epsilon_{\mathrm{ch}}^{1||3}$ efficiency as defined in Section 5.8.1. For this case a bias is observed between the "Data-like" and "MC" cases. This is mainly due to the OS requirement between the electron and the leading PF charged hadron of the PFTau which naturally favors 1 prong τ-jets as shown in the left plot of Figure 5.41. As this bias still lies within the statistical uncertainties for $100\,\mathrm{pb}^{-1}$ of integrated luminosity, it will become dominant in later stages of data taking when systematic uncertainties will be better understood, and therefore the OS requirement should be modified (require OS between leading or second leading PF charged hadron and electron) in order to reduce this bias.

5.9 Conclusions

This chapter described the reconstruction and selection of Z$\rightarrow \tau\tau \rightarrow$ τ-jet+e+X events from trigger level to offline, and methods for estimating the various backgrounds for the purpose of measuring the τ-jet "core" identification efficiency. These were aimed for $100\,\mathrm{pb}^{-1}$ of integrated luminosity during the early stages of data taking. In order to obtain a pure and unbiased sample of τ-jets, tight electron selections were placed resulting in 74.5±2.6 Signal events with S/(S+B)=0.73 where the errors represent the statistical uncertainty of the full signal sample used in this

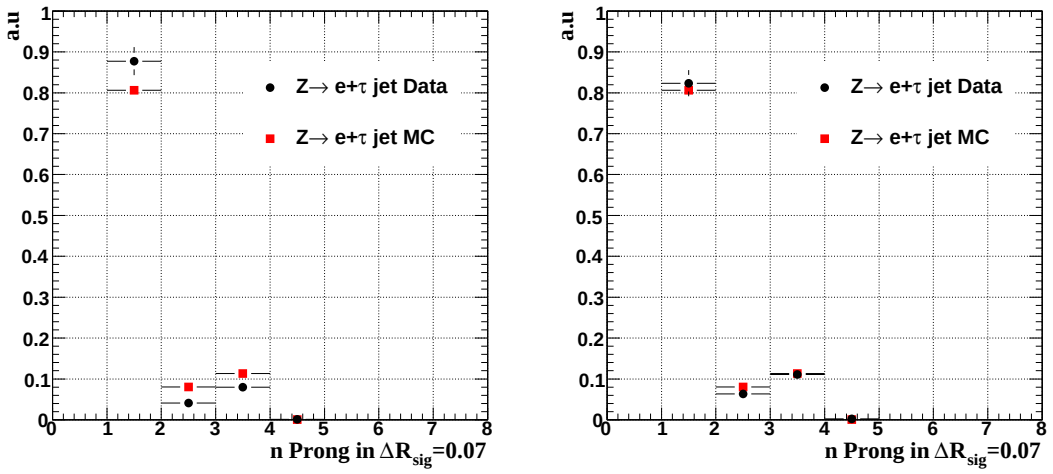

Figure 5.41: Number of PF charged hadrons (Prongs) within $\Delta R_{sig} = 0.07$, $\Delta R_{iso} = 0.15$ with $p_T^{trk} > 1\,GeV/c$ for PFTaus as defined in Section 5.8.1 for both "Data-like" and "MC" cases. Left: The OS requirement is applied. Right: No OS requirement is applied.

analysis. With these events the PFTau "core" track isolation was evaluated as 85.5%±4.0% (stat.)±5.7% (syst.) where the statistical uncertainty reflects $100\,pb^{-1}$ of integrated luminosity and the systematic uncertainty is estimated using projected uncertainties at $100\,pb^{-1}$ of integrated luminosity.

The availability of larger QCD and γ+jets MC samples was limited. Therefore running over larger such samples would help in order to further investigate the background extraction techniques and to evaluate more accurately their contribution to the total number of events passing all the selections of this analysis. During the first LHC collisions and with $>100\,pb^{-1}$ of integrated luminosity, selections will be re-tuned in order to account for a looser $OS_{e\tau}$ cut which adds a bias to the 1 or 3 prong efficiency measurement. Running over LHC collision data would also help understand discrepancies with simulation as well as systematic uncertainties. Ultimately a combination of the Z$\rightarrow \tau\tau \rightarrow \tau$-jet+e+X PFTau "core" efficiency measurements with the corresponding from Z$\rightarrow \tau\tau \rightarrow \tau$-jet+$\mu$+X analyses, which will achieve a better S/(S+B) and signal yield, will be made. The first efficiency measurement of the PFTau algorithms on real τ-jets will play an important role in placing limits for the first (MSSM) H$\rightarrow \tau\tau \rightarrow \tau$-jet+l+X searches. Finally all the techniques used in the reconstruction, selection and background estimation of this

Z$\rightarrow \tau\tau \rightarrow \tau$-jet+$e$+X analysis will be directly applied to analogous (MSSM) Higgs searches.

Chapter 6

Conclusions

Tau leptons are important in Higgs searches, particularly within an MSSM scenario where they play a central role due to a potential enhancement of the coupling by $\tan\beta$. Hence decays of electrically neutral (MSSM) Higgs bosons to two τ leptons have a significant branching ratio. Requiring one of the τs to decay leptonically and the other hadronically gives us a good balance between signal yield and background suppression. The CMS detector is ideally placed to detect such signals due both to its good tracking performance and the fine granularity of the electromagnetic calorimeter.

However before such searches take place, it is important to ensure that Standard Model results are reproduced. Therefore during the initial stages of data taking there will be a major effort from the CMS collaboration to measure standard candles involving W and Z bosons. In this context Z$\rightarrow \tau\tau$ decays are important, as they provide a test bench for analogous H$\rightarrow \tau\tau$ and can allow for the measurement of τ-jet selection efficiencies which is vital in extracting the Higgs production cross section and branching ratio and therefore essential in determining potential MSSM parameters.

This thesis describes the first CMS analysis from trigger to offline including data driven background estimation techniques, aimed for selecting and reconstructing Z$\rightarrow \tau\tau \rightarrow e + \tau$-jet events and measuring the "core" τ-jet track isolation efficiency.

The e+τ High Level Trigger

A combined electron and τ-jet trigger using a logical AND was developed and tuned for the $10^{32}\,\mathrm{cm}^{-2}\mathrm{s}^{-1}$ instantaneous luminosity regime. The motivation behind a combined e+τ-jet trigger (e+τ), is mainly in order to lower the $\mathrm{E_T}$ threshold of the electron trigger while keeping the rate due to QCD low by requiring the existence of a τ-jet object as well. As τ decays to leptons (electrons, muons) are three body decays, the $\mathrm{E_T}$ spectrum of the out-coming lepton tends to be soft (majority have $\mathrm{E_T}$ <30 GeV) for τs originating from Z and light Higgs decays. Therefore by having a lower electron $\mathrm{E_T}$ threshold compared to the single electron trigger, one can gain in the number of signal events (H(Z)$\rightarrow\ \tau\tau\ \rightarrow\ e + \tau$-jet) stored on tape. The performance of the e+τ trigger (HLT_IsoEle12_IsoTau_Trk3) for the $10^{32}\,\mathrm{cm}^{-2}\mathrm{s}^{-1}$ regime on Z$\rightarrow\ \tau\tau\ \rightarrow\ e + \tau$-jet and QCD di-jet events was presented. Given the parameters of Table 3.5, which were tuned to optimise the Z$\rightarrow\ \tau\tau\ \rightarrow\ e + \tau$-jet efficiency while keeping the QCD rate below 1 Hz, and the offline pre-selections of Table 3.2, a signal efficiency of (44.6±1.6)% with a QCD rate of (0.7±0.2) Hz for an instantaneous luminosity of $10^{32}\,\mathrm{cm}^{-2}\mathrm{s}^{-1}$ was obtained. Finally the efficiency of the logical OR between HLT_IsoEle15_L1I, HLT_IsoEle12_IsoTau_Trk3 was compared to the HLT_IsoEle15_L1I yielding efficiencies of (65.4 ± 2.5)% and (61.4 ± 2.5)% respectively. The marginal gain in efficiency was due to the small difference between the HLT electron $\mathrm{E_T}$ thresholds of the two triggers. Therefore the e+τ trigger will play a more important role during higher instantaneous luminosity regimes where higher rates will mean that the electron $\mathrm{E_T}$ threshold of the single isolated electron trigger will have to be increased to > 20 GeV.

During the LHC start-up, the HLT_IsoEle12_IsoTau_Trk3 selections will be re-tuned in order to increase the efficiency on τ-jets by loosening the pixel triplet requirement. This could be achieved for example by building tracks using pixel doublet hits together with a hit in the silicon strip layers for the cases when a third pixel hit is not found. Moreover by integrating PFlow objects in the trigger, a better QCD rejection could be achieved. In particular the use of more sophisticated PFlow based calorimetric shower shape variables at L2 has been a major improvement of the τ-jet triggers at CMS over the last few months. These improvements need to be further

studied and propagated to the later stages of the τ trigger and finally integrated with the e+τ trigger. Finally commissioning the τ-jet triggers using the first LHC collision data would ensure that CMS is ready for a wide range of τ related physics.

L1 τ jet trigger commissioning

By analysing randomly and cosmic muon triggered events from the first and third periods of the CRUZET exercise, the effect of calorimetric noise on the L1 jet rate and L1 τ-jet algorithmic efficiency were estimated. Considering a L1 jet trigger threshold of 40 GeV the rate of this trigger due to noise accounts only for $\sim$2% of the total available L1 start-up rate. Furthermore by placing calorimetric activity cuts for the L1 τ veto patterns at (E_T^{ECAL}, E_T^{HCAL}) = (3,3) GeV and the L1 τ-jet isolation threhold of E_T^{iso}=2 GeV results in an acceptable efficiency loss due to calorimetric noise of <5%. With these L1 τ-jet parameters the dominant loss of efficiency is due to QCD backgrounds produced along side the Z either from the recoil jet(s) or multiple parton scattering and is $\sim$20%.

Testing the new Isolation Veto in the L1 hardware as soon as it is made available is of vital importance for the commissioning of the L1 τ-jet trigger . The next step would then be to commission the τ L1 and HLT on electrons from Z$\rightarrow$ ee events, during the LHC collisions, which provide a large source of isolated calorimetric depositions and track, allowing for a swift understanding of any algorithmic features and of the isolation parameters which will need to be readjusted to account for the LHC underlying event conditions.

Reconstruction and selection of Z$\rightarrow \tau\tau \rightarrow$ τ-jet+e+X events

Chapter 5 described the reconstruction and selection of Z$\rightarrow \tau\tau \rightarrow$ τ-jet+e+X events from trigger level to offline and methods for estimating the various backgrounds for the purpose of measuring the τ-jet "core" identification efficiency were presented. These were aimed for 100 pb^{-1} of integrated luminosity during the early stages of data taking. In order to obtain a pure and unbiased sample of τ-jets, tight electron selections were placed resulting in 74.5$\pm$2.6 Signal events with S/(S+B)=0.73 where the errors represent the statistical uncertainty of the full Signal sample used in this analysis. With these events the PFTau "core" track isolation efficiency was evaluated as 85.5%$\pm$4.0% (stat.)$\pm$5.7% (syst.) where the statistical uncertainty reflects

$100\,\mathrm{pb}^{-1}$ of integrated luminosity and the systematic uncertainty is estimated using projected uncertainties at $100\,\mathrm{pb}^{-1}$ of integrated luminosity.

The availability of larger QCD and γ+jets simulated samples was limited. Table 5.1 shows that only O($1\,\mathrm{pb}^{-1}$) of QCD and γ+jets were available for this O($100\,\mathrm{pb}^{-1}$) analysis. Therefore running over larger such samples would help in order to further investigate the background extraction techniques and to evaluate more accurately their contribution to the total number of events passing all the selections of this analysis. During the first LHC collisions and with $>100\,\mathrm{pb}^{-1}$ of integrated luminosity, selections will be re-tuned in order to account for a looser opposite sign charge cut between the electron and the leading PF charged hadron of the PFTau ($\mathrm{OS}_{e\tau}$) which adds a bias to the 1 or 3 prong efficiency measurement. Running over LHC collision data would also help understand discrepancies with simulation as well as systematic uncertainties. Ultimately a combination of the Z$\rightarrow \tau\tau \rightarrow \tau$-jet+e+X PFTau "core" efficiency measurements with the corresponding from Z$\rightarrow \tau\tau \rightarrow \tau$-jet+$\mu$+X analyses, which will achieve a better S/(S+B) and signal yield, will be made. The first efficiency measurement of the PFTau algorithms on real τ-jets will play an important role in placing limits for the first (MSSM) H$\rightarrow \tau\tau \rightarrow \tau$-jet+l+X searches. Finally all the techniques used in the reconstruction, selection and background estimation of this Z$\rightarrow \tau\tau \rightarrow \tau$-jet+$e$+X analysis will be directly applied to analogous (MSSM) Higgs searches.

References

[1] The CMS collaboration, "CMS High Level Trigger," CERN/LHCC 2007-021.

[2] S. Gennai *et al.*, "Tau reconstruction and identification with particle-flow techniques using the CMS detector at LHC," CMS AN-2008/043.

[3] A. Nikitenko *et al.*, "Search for the Standard Model Higgs boson produced in Vector Boson Fusion and decaying into $\tau\tau$ pair in CMS with $1\,\mathrm{fb}^{-1}$," CMS AN-2007/035.

[4] ALEPH CDF D0 DELPHI L3 OPAL SLD Collaborations, "Precision Electroweak Measurements and Constraints on the Standard Model," CERN-PH-EP/2008-020.

[5] A. Djouadi, "The Anatomy of Electro-Weak Symmetry Breaking, Tome 2," hep-ph/0503173v2.

[6] The DØ collaboration, "Search for MSSM Higgs Boson Production in Di-tau Final States with $\mathcal{L} = 2.2\,\mathrm{fb}^{-1}$ at the DØ Detector," DØ Note 5740-CONF.

[7] A. Tricoli, A. Copper-Sarkar, and C. Gwenlan, "Uncertainty on W and Z production at the LHC HERA-LHC Workshop Proceedings," hep-ex/0509002v1.

[8] A. D. Martin, R. G. Roberts, W. J. Stirling, and T. R. S, "Parton Distributions and the LHC: W and Z Production," hep-ph/9907231v1.

[9] The CMS collaboration, "CMS Physics Technical Design Report Volume 1: Detector Performance and Software," CERN/LHCC 2006-001.

[10] V. Ciulli, "The CMS Silicon Strip Tracker: from integration to start-up," CMS CR-2008/001.

[11] The CMS Collaboration, "The CMS experiment at the CERN LHC," *Journal of Instrumentation* **3** (2008), no. 08, S08004.

[12] G. Baiatian and A. Sirunyan, "Energy Response and Longitudinal Shower Profiles Measured in CMS HCAL and Comparison with GEANT4," CMS AN-2006/143.

[13] The CMS Computing Model RTAG, "The CMS Computing Model," CERN-LHCC-2004-035/G-083.

[14] S. Baffioni *et al.*, "Electron Reconstruction in CMS," CMS NOTE 2006/40.

[15] E. Meschi *et al.*, "Electron Reconstruction in the CMS Electromagnetic Calorimeter," CMS Note 2001/034.

[16] A. Askew *et al.*, "A Review of Clustering in the Electromagnetic Calorimeter," CMS NOTE IN PREPARATION.

[17] The Particle Flow Physics Object Group, "Particle Flow Reconstruction of Jets, MET, and Taus," CMS AN-2009/039.

[18] Nguyen, Chi-Nhan, "Personal Communication.".

[19] C. Amsler et al. (Particle Data Group) *Phys. Rev. Lett.* **B** (2008), no. 667, 1.

[20] M. Takahashi, "Optimization of CMS detector performance and detection of the standard model Higgs boson via the qqH, $H \to \tau\tau$ channel with a lepton + a jet in the final state,". CERN-THESIS-2007-021.

[21] CMS collaboration, "Search for the Standard Model Higgs boson produced in Vector Boson Fusion and decaying into τ pair in CMS with $1\,\mathrm{fb}^{-1}$," CMS PAS HIG-08-008.

[22] CMS collaboration, "Towards the measurement of the $t\bar{t}$ cross section in the $e\tau$ and $\mu\tau$ dilepton channel in pp collisions at $\sqrt{s} = 14\,\text{TeV}$," `CMS PAS TOP_08_004`.

[23] T. P. Cheng and L. F. Li, *Gauge Theory of elementary particle physics*. Oxford university press, 2000.

[24] E. Leader and E. Predazzi, *Introduction to gauge theories and modern particle physics*. Cambridge university press, 1996.

[25] E. Noether, "Invariant Variation Problems, Translation of original 1918 paper," *Transport Theory and Statistical Mechanics* **1** (1971), no. 3, 183–207.

[26] A. Salam, "In Elementary Particle Theory Relativistic Groups and Analyticity," *Nobel Symposium No.8* (1968).

[27] S. Weinberg *Phys. Rev. Lett* **19** (1967) 1264.

[28] S. Glashow *Nucl. Phys.* **22** (1961) 579.

[29] M. Gell-Man, "A Schematic Model of Baryons and Mesons," *Phys. Lett* **8** (1964) 214–215.

[30] G. S. Guralnik, C. R. Hagen, and T. Kibble, "Global Conservetion Laws and Massless Particles," *Phys. Rev. Lett.* **13** (1964) 585.

[31] P. Higgs *Phys. Rev. Lett.* **13** (1964) 508.

[32] A. Djouadi, "The Anatomy of Electro-Weak Symmetry Breaking, Tome 1," `hep-ph/0503172v2`.

[33] J. Goldstone, A. Salam, and S. Weinberg, "Broken Symmetries," *Phys. Rev.* **127** (1962) 965–970.

[34] D. Balin and A. Love, *Supersymmetric gauge field theory and string theory*. Taylor & Francis, 1996.

[35] I. Aitchison, "Supersymmetry and the MSSM: An Elementary Introduction," `hep-ph/0505105v1`.

[36] J. Wess and J. Bagger, *Supersymmetry and Supergravity*. Princeton University Press, 1992.

[37] S. Coleman and J. Mandula, "All Possible Symmetries of the S Matrix," *Phys. Rev.* **159** (1967) 1251.

[38] R. Haag, J. Lopuszanski, and M. Sohnius *Nucl. Phys.* **B88** (1975) 257.

[39] D. Candlin *Nuovo Cimento* **4** (1956) 224.

[40] J. Wess and B. Zumino, "All Possible Symmetries of the S Matrix," *Phys. Rev.* **49B** (1974) 52.

[41] S. Martin, "A Supersymmetry Primer," `hep-ph/9709356v5`.

[42] D. Griffiths, *Introduction to Elementary Particles*. John Wiley and Sons, 1987.

[43] N. Adam *et al.*, "Towards a Measurement of the Inclusive W$\rightarrow e\nu$ and Z$\rightarrow ee$ Cross section in pp Collisions at $\sqrt{s} = 14\,\text{TeV}$," `CMS AN-2007/026`.

[44] M. L. Perl, G. S. Abrams, A. M. Boyarski, M. Breidenbach, D. D. Briggs, F. Bulos, W. Chinowsky, J. T. Dakin, G. J. Feldman, C. E. Friedberg, D. Fryberger, G. Goldhaber, G. Hanson, F. B. Heile, B. Jean-Marie, J. A. Kadyk, R. R. Larsen, A. M. Litke, D. Lüke, B. A. Lulu, V. Lüth, D. Lyon, C. C. Morehouse, J. M. Paterson, F. M. Pierre, T. P. Pun, and P. A. Rapidis, "Evidence for anomalous lepton production in $e+-e-$ annihilation," *Phys. Rev. Lett.* **35** (1975), no. 22, 1489–1492.

[45] LHC Project `http://lhc.web.cern.ch/lhc/`.

[46] ATLAS Collaboration `http://atlas.web.cern.ch/Atlas/index.html`.

[47] ALICE Collaboration `http://aliceinfo.cern.ch/`.

[48] LHCb Collaboration `http://http://lhcb.web.cern.ch/lhcb/`.

[49] Worldwide LHC Computing Grid `http://lcg.web.cern.ch/lcg/`.

[50] The MONARC Project `http://monarc.web.cern.ch/MONARC/`.

[51] M. LeBourgeois and V. Sharma, "A Update on Electron Isolation." http://indico.cern.ch/conferenceDisplay.py?confId=29233.

[52] The CMS collaboration, "The TriDAS Project Technical Design Report, Volume 1: The Trigger Systems," CERN/LHCC 2000-038.

[53] S. Gennai, "Tau Trigger Review." http://indico.cern.ch/conferenceDisplay.py?confId=49079.

[54] The CMS collaboration, "The TriDAS Project Technical Design Report, Volume 2: Data Acquisition and High-Level Trigger," CERN/LHCC 02-26.

[55] J. Damgov *et al.*, "Analysis of Cosmic Muons in the CMS HCAL Barrel from CRUZET I,II and III," CMS IN-2008/035.

[56] T. Sjostrand, S. Mrenna, and P. Skands, "PYTHIA 6.4 Physics Manual," hep-ph/0603175.

[57] J. Alwall *et al.*, "New Developments in MadGraph/MadEvent," *AIP Conf. Proc.* **1078** (2009) 84–89, 0809.2410.

[58] "G4–a simulation toolkit," *Nuclear Instruments and Methods in Physics Research Section A: Accelerators, Spectrometers, Detectors and Associated Equipment* **506** (2003), no. 3, 250 – 303.

[59] N. Marinelli, "Identification of converted photons," CMS AN-2006/005.

[60] CMS collaboration, "Towards the Search for the Standard Model Higgs boson produced in Vector Boson Fusion and decaying into a τ pair in CMS with $1\,\mathrm{fb}^{-1}$: τ identification studies," CMS PAS HIG-08-008.

[61] A. Abulancia *et al.*, "Measurement of $\sigma(p\bar{p} \to Z) \cdot \mathcal{B}(Z \to \tau\tau)$ in $p\bar{p}$ collisions at $\sqrt{s} = 1.96\,\mathrm{TeV}$," *Phys. Rev. D* **75** (2007).

[62] A. Nikitenko *et al.*, "Jet Plus Tracks Algorithm for Calorimeter Jet Energy Corrections in CMS," CMS AN-2009/031.

[63] Rick Field and R. Craig Group, "Pythia Tune A, Herwig and Jimmy in Run 2 at CDF," hep-ph/0510198v1.

[64] D. Kar, "Measurement of the Underlying Event at Tevatron," hep-ex/0905.2323v1.

[65] The CMS Collaboration, "Measurement of the Underlying Event in Jet Topologies using Charged Particle and Momentum Densities," CMS PAS QCD_07_003.